CONTENTS

ABSTRACTS

Adel Tellili, Nouceyba Abdelkrim, Bahaa Jaouadi, Mohamed Naceur Abdelkrim
Diagnosis of Discrete-Time Singularly Perturbed Systems Based on Slow Reduced Subsystem

This paper deals with the diagnosis of discrete-time singularly perturbed systems presenting two time scales property. Parity space method is considered to generate the fault detection residual. The focus is in two directions. First, we discuss the residual ill-conditioning caused by the singular perturbation parameter. Then, the use of the slow subsystem is considered to make the fault diagnosis easier. It is shown that the designed diagnostic algorithm based on reduced order model is close to the one synthesized using the full order system. The developed approach aims at reducing the computational load and the ill-conditioning for stiff residual generation problem. Two examples of application are used to demonstrate the efficiency of the proposed method.

Jacek Kłosiński, Jarosław Janusz, Rafał Nycz
The Impact of the FLC Controller's Settings on the Precision of the Positioning of a Payload Transferred by a Mobile Crane

The paper presents a model of a control system of the slewing motion of a mobile crane in which the FLC controller was used, and then selected results of the numerical simulations of this model were presented. The influence of this controller's settings on the precision with which the payload is positioned after it has been transferred to a target point for different angles of rotation of the jib, different lengths of the rope and different input signals of the controller was investigated.

Piotr Grześ
Numerical Analysis of Temperature Field in a Disc Brake at Different Cover Angle of the Pad

In the paper an influence of the cover angle of the pad on temperature fields of the components of the disc brake is studied. A three-dimensional finite element (FE) model of the pad-disc system was developed at the condition of equal temperatures on the contacting surfaces. Calculations were carried out for a single braking process at constant deceleration assuming that the contact pressure corresponds with the cover angle of the pad so that the moment of friction is equal in each case analysed. Evolutions and distributions of temperature both for the contact surface of the pad and the disc were computed and shown.

Arkadiusz Trąbka
The Impact of the Support System's Kinematic Structure on Selected Kinematic and Dynamic Quantities of an Experimental Crane

This paper presents a comparative analysis of two kinematic structures of the support system (with supports with bilateral and unilateral constraints), which were used in an experimental model of a crane. The computational model was developed by using the ADAMS software. The impact of the kinematic structure of the support system on selected kinematic and dynamic values that were recorded during the slewing motion was analysed. It was found, among other things, that an increased number of degrees of freedom of the support system leads to multiple distortions of time characteristics of kinematic and dynamic quantities.

Marcin Derlatka
Examination of the Effect of Psychophysical Factors on the Quality of Human Gait Recognition

The paper presents an analysis concerning the influence of selected psychophysical parameters on the quality of human gait recognition. The following factors have been taken into account: body height (BH), body weight (BW), the emotional condition of the respondent, the physical condition of the respondent, previous injuries or dysfunctions of the locomotive system. The study was based on data measuring the ground reaction forces (GRF) among 179 participants (3 315 gait cycles). Based on the classification, some kind of confusion matrix were established. On the basis of the data included in the matrix, it was concluded that the wrong classification was most affected by the similar weight of two confused people. It was also noted, that people of the same gender and similar BH were confused most often. On the other hand, previous body injuries and dysfunctions of the motor system were the factors facilitating the recognition of people. The results obtained will allow for the design of more accurate biometric systems in the future.

Marcin Skoczylas
Vision Analysis System for Autonomous Landing of Micro Drone

This article describes a concept of an autonomous landing system of UAV (Unmanned Aerial Vehicle). This type of device is equipped with the functionality of FPV observation (First Person View) and radio broadcasting of video or image data. The problem is performance of a system of autonomous drone landing in an area with dimensions of 1m×1m, based on CCD camera coupled with an image transmission system connected to a base station. Captured images are scanned and landing marker is detected. For this purpose, image features detectors (such as SIFT, SURF or BRISK) are utilized to create a database of keypoints of the landing marker and in a new image keypoints are found using the same feature detector. In this paper results of a framework that allows detection of defined marker for the purpose of drone landing field positioning will be presented.

Ewa Och
Frictional Heating during Sliding of Two Semi-Spaces with Arbitrary Thermal Nonlinearity

Analytical and numerical solution for transient thermal problems of friction were presented for semi limited bodies made from thermosensitive materials in which coefficient of thermal conductivity and specific heat arbitrarily depend on the temperature (materials with arbitrary non-linearity). With the constant power of friction assumption and imperfect thermal contact linearization of nonlinear problems formulated initial-boundary thermal conductivity, using Kirchhoff transformation is partial. In order to complete linearization, method of successive approximations was used. On the basis of obtained solutions a numerical analysis of two friction systems in which one element is constant (cermet FMC-845) and another is variable (grey iron ChNMKh or aluminum-based composite alloy AL MMC) was conducted.

Józef Błachnio, Wojciech I. Pawlak
Non-Uniformity of the Combustor Exit Flow Temperature in Front of the Gas Turbine

Various types of damages to gas-turbine components, in particular to turbine blades, may occur in the course of gas turbine operation. The paper has been intended to discuss different forms of damages to the blades due to non-uniformity of the exit flow temperature. It has been shown that the overheating of blade material and thermal fatigue are the most common reasons for these damages. The paper presents results from numerical experiments with use of the computer model of the aero jet engine designed for simulations. The model has been purposefully modified to take account of the assumed non-homogeneity of the temperature field within the working agent at the turbine intake. It turned out that such non-homogeneity substantially affects dynamic and stat-ic properties of the engine considered as an object of control since it leads to a lag of the acceleration time and to increase in fuel consumption. The summarized simulation results demonstrate that the foregoing properties of a jet engine are subject to consider-able deterioration in pace with gradual increase of the assumed non-homogeneity of the temperature field. The simulations made it possible to find out that variations of the temperature field non-homogeneity within the working agent at the turbine intake lead to huge fluctuation of the turbine rpm for the idle run.

Andrzej Koszewnik, Kamil Troc, Maciej Słowik
PID Controllers Design Applied to Positioning of Ball on the Stewart Platform

The paper presents the design and practical implementation of PID controllers for a Stewart platform. The platform uses a resistance touch panel as a sensor and servo motors as actuators. The complete control system stabilizing the ball on the platform is realized with the Arduino microcontroller and the Matlab/Simulink software. Two processes required to acquire measurement signals from the touch panel in two perpendicular directions X and Y, are discussed. The first process includes the calibration of the touch panel, and the second process - the filtering of measurement signals with the low pass Butterworth filter. The obtained signals are used to design the algorithm of the ball stabilization by decoupling the global system into two local subsystems. The algorithm is implemented in a soft real time system. The parameters of both PID controllers (PIDx and PIDy) are tuned by the trial-error method and implemented in the microcontroller. Finally, the complete control system is tested at the laboratory stand.

Adam Kotowski
Cross-Correlation-Based Method vs. Classical FFT for Spectral Analysis of Impulse Response

The paper presents comparison of results of impulse response spectral analysis that has been obtained using a method based on cross-correlation with results obtained using classical FFT. The presented non-Fourier method is achieved by correlating the analyzed signal and reference single-harmonic signals and using Hilbert transform to obtain an envelope of cross-correlation. The envelope of cross-correlation makes it possible to calculate appropriate indicator and make its plot in frequency domain as a spectrum. The spectrum obtained this way has its advantage over the FFT that the spectral resolution does not depend on duration of signal. At the same time, the spectral resolution can be much greater than spectral resolution resultant from FFT. Obtained results show that presented non-Fourier method gives frequency readout more accurate in comparison to FFT when the impulse response is a short-time signal e.g. few dozen of miliseconds lasting.

DIAGNOSIS OF DISCRETE-TIME SINGULARLY PERTURBED SYSTEMS BASED ON SLOW SUBSYSTEM

Adel TELLILI[*,*], Nouceyba ABDELKRIM[*,**], Bahaa JAOUADI[*], Mohamed Naceur ABDELKRIM[*,****]**

[*]Unité de Recherche MACS, Ecole Nationale d'Ingénieurs de Gabès, Avenue Omar Ibn El Khattab - Zerig - 6029 Gabès, University of Gabès, Tunisia
[**]Institut Supérieur des Systèmes Industriels de Gabès, Rue, Slaheddine El Ayoubi – 6032 Gabès, University of Gabès, Tunisia
[***]Institut Supérieur des Etudes Technologiques de Djerba, Avenue 7 novembre - 4116 Midoun Jerba, Tunisia
[****]Ecole Nationale d'Ingénieurs de Gabès, Avenue Omar Ibn El Khattab - Zerig - 6029 Gabès, University of Gabès, Tunisia

adel_tellili@lycos.com, nouceyba.naceur@laposte.net, jaouadibahaa@yahoo.com, naceur.abdelkrim@enig.rnu.tn

Abstract: This paper deals with the diagnosis of discrete-time singularly perturbed systems presenting two time scales property. Parity space method is considered to generate the fault detection residual. The focus is in two directions. First, we discuss the residual ill-conditioning caused by the singular perturbation parameter. Then, the use of the slow subsystem is considered to make the fault diagnosis easier. It is shown that the designed diagnostic algorithm based on reduced order model is close to the one synthesized using the full order system. The developed approach aims at reducing the computational load and the ill-conditioning for stiff residual generation problem. Two examples of application are used to demonstrate the efficiency of the proposed method.

Key words: Discrete-Time Singularly Perturbed System, Two Time Scales Property, Model Based Fault Diagnosis, Parity Space Approach, Slow Subsystem

1. INTRODUCTION

Singular perturbation systems involving in their realistic representation several small parameters like unmodelled parasitic, capacitances, time and inertia constants, found their applicability in chemical reactors, power system dynamics, control of large scale systems and similar settings (Khalil, 1987; Kokotovic et al., 1986; Tellili et al., 2007). The presence of high dimensionality and ill-conditioning in such systems, gives rise to difficulties in their fault diagnosis and control. These problems are considerably simplified if a decomposition of fast and slow dynamics can be achieved.

Singularly perturbed discrete-time systems are described through three models. The slow and the fast sampling rate models which are obtained through discretization of the singularly perturbed continuous-time system and the pure one which is discrete in nature (Litkouhi and Khalil, 1985; Naidu et al., 1987).

The vulnerability of those time-scale systems, like other automated complex systems, to malfunctions in control actuators, measurement sensors and process equipment requires the design of diagnosis methods to detect and isolate faults. Several approaches have been developed to design diagnosis systems using model-based methods like observer based methods (Frank, 1990; Patton and Chen, 1997), parameter estimation (Clark et al., 1975; Isermann, 1993; Pana and Stoian, 2008) and the parity relation approach which is one of the most commonly used techniques in fault detection and isolation (Chow and Willsky, 1984; Gertler, 1997; Patton and Chen, 1991). Many authors were interested in the fault diagnosis of singularly perturbed systems. Tellili et al. (2004) considered the fast subsystem as a modeling error and generated residuals by using robust parity space in order to detect and isolate faults in singularly perturbed systems. Gong and Khorasani (2005) used the observers relating to the slow and fast reduced subsystems to generate fault diagnosis algorithm in order to detect and isolate actuator faults in continuous singularly perturbed systems. Also Oloomi et al. (2004) employed Chang transformation to separate dynamics of continuous singularly perturbed systems and the original observer based fault diagnosis filter will be approximated by the slow and fast filters. Mease (2005) discusses the use of Lyapunov exponents and vectors to diagnose of the non-linear singularly perturbed systems in flight dynamics.

In this paper, the problem of fault diagnosis of discrete singularly perturbed systems is studied by designing residuals based on reduced slow subsystem. Using parity space approach, the residual for the original system will be generated and then reduced in order to be decoupled from singular perturbation parameter.

2. SYSTEM DESCRIPTION AND PROBLEM STATEMENT

Consider the following discrete-time singularly perturbed system (Litkouhi and Khalil, 1985; Naidu et al., 1987; Kafri and Abed, 1996):

$$\begin{cases} \begin{bmatrix} \mathrm{x}_1(k+1) \\ \mathrm{x}_2(k+1) \end{bmatrix} = \begin{bmatrix} \mathrm{A}_{11} & \varepsilon \mathrm{A}_{12} \\ \mathrm{A}_{21} & \varepsilon \mathrm{A}_{22} \end{bmatrix} \begin{bmatrix} \mathrm{x}_1(k) \\ \mathrm{x}_2(k) \end{bmatrix} + \begin{bmatrix} \mathrm{B}_1 \\ \mathrm{B}_2 \end{bmatrix} \mathrm{u}(k) \\ \mathrm{y}(k) = \begin{bmatrix} \mathrm{C}_1 & \varepsilon \mathrm{C}_2 \end{bmatrix} \begin{bmatrix} \mathrm{x}_1(k) \\ \mathrm{x}_2(k) \end{bmatrix} \end{cases} \quad (1)$$

where: $\mathrm{x}_1(k) \in R^{n_1}$, $\mathrm{x}_2(k) \in R^{n_2}$, are state vectors, $\mathrm{y}(k) \in R^p$ is the output, and $\mathrm{u}(k) \in R^m$ is the control input. The singular perturbation parameter ε satisfies $0 < \varepsilon < 1$. All matrices are assumed to have appropriate dimensions.

The above description is obtained by setting i and j to zero in the following model:

$$\begin{cases}\begin{bmatrix}\mathrm{x}_1(k+1)\\ \varepsilon^{2i}\mathrm{x}_2(k+1)\end{bmatrix}=\begin{bmatrix}\mathrm{A}_{11} & \varepsilon^{1-j}\mathrm{A}_{12}\\ \varepsilon^{j}\mathrm{A}_{21} & \varepsilon\mathrm{A}_{22}\end{bmatrix}\begin{bmatrix}\mathrm{x}_1(k)\\ \mathrm{x}_2(k)\end{bmatrix}+\\ \qquad\qquad\begin{bmatrix}\mathrm{B}_1\\ \varepsilon^{j}\mathrm{B}_2\end{bmatrix}\mathrm{u}(k)\\ \mathrm{y}(k)=\begin{bmatrix}\mathrm{C}_1 & \varepsilon^{1-j}\mathrm{C}_2\end{bmatrix}\begin{bmatrix}\mathrm{x}_1(k)\\ \mathrm{x}_2(k)\end{bmatrix}\end{cases} \quad (2)$$

which represents a pure singularly perturbed discrete system issued from the difference equations introducing a small positive parameter ε in the state vector (Naidu et al., 1987). Corresponding slow and fast subsystems can be obtained from the original system by singular perturbation approach or by block diagonalization (Litkouhi and Khalil, 1985; Naidu et al., 1987). The two approaches give identical results.

To derive the slow subsystem, it is assumed that the fast variables have reached their established regime by setting $\varepsilon = 0$. Then, we get the slow subsystem of dimension n_1 as:

$$\begin{cases}\mathrm{x}_l(k+1)=\mathrm{A}_{11}\,\mathrm{x}_l(k)+\mathrm{B}_1\mathrm{u}_l(k)\\ \mathrm{y}_l(k)=\mathrm{C}_1\,\mathrm{x}_l(k)\\ \mathrm{x}_l(k_0)=\mathrm{x}_{10}\end{cases} \quad (3)$$

The fast subsystem of dimension n_2, obtained by considering that the slow variables are constant during the fast transients, is given by:

$$\begin{cases}\mathrm{x}_r(k+1)=\mathrm{A}_r\,\mathrm{x}_r(k)+\mathrm{B}_r\mathrm{u}_r(k)\\ \mathrm{y}_r(k)=\mathrm{C}_r\,\mathrm{x}_r(k)+\mathrm{D}_r\mathrm{u}_r(k)\\ \mathrm{x}_r(k_0)=\mathrm{x}_{20}-\mathrm{A}_{22}^{-1}\mathrm{A}_{21}\mathrm{x}_{10}\end{cases} \quad (4)$$

where: $\mathrm{A}_r=\varepsilon\left(\mathrm{A}_{22}-\mathrm{A}_{21}\mathrm{A}_{11}^{-1}\mathrm{A}_{12}\right)$, $\mathrm{B}_r=\mathrm{B}_2-\mathrm{A}_{21}\mathrm{A}_{11}^{-1}\mathrm{B}_1$, $\mathrm{C}_r=\varepsilon\left(\mathrm{C}_2-C_1\mathrm{A}_{11}^{-1}\mathrm{A}_{12}\right)$, $\mathrm{D}_r=-\mathrm{C}_1\mathrm{A}_{11}^{-1}\mathrm{B}_1$, u_l and u_r verify $\mathrm{u}=\mathrm{u}_l+\mathrm{u}_r$ and represent respectively the fast and slow components of the input u.

Denote:

$$\mathrm{A}(\epsilon)=\begin{bmatrix}\mathrm{A}_{11} & \varepsilon\,\mathrm{A}_{12}\\ \mathrm{A}_{21} & \varepsilon\,\mathrm{A}_{22}\end{bmatrix},\ \mathrm{B}=\begin{bmatrix}\mathrm{B}_1\\ \mathrm{B}_2\end{bmatrix},\ \mathrm{C}(\varepsilon)=\begin{bmatrix}\mathrm{C}_1 & \varepsilon\,\mathrm{C}_2\end{bmatrix}$$

and $\mathrm{x}(k)=\begin{bmatrix}\mathrm{x}_1(k)\\ \mathrm{x}_2(k)\end{bmatrix}$.

Then system (1) can be rewritten, in presence of additive fault $\boldsymbol{f}(k)$, as follows:

$$\begin{cases}\dot{\mathrm{x}}(k)=\mathrm{A}(\varepsilon)\,\mathrm{x}(k)+\mathrm{B}\,\mathrm{u}(k)+\mathrm{E}_1\,\mathrm{f}(k)\\ \mathrm{y}(k)=\mathrm{C}(\varepsilon)\,\mathrm{x}(k)+\mathrm{E}_2\,\mathrm{f}(k)\end{cases} \quad (5)$$

where E_2 and E_2 are known as fault entry matrices of appropriate dimensions.

The problem under consideration is to design a fault diagnosis algorithm through the construction of an appropriate residual based on parity space method.

3. RESIDUAL GENERATION BASED ON THE ORIGINAL SYSTEM

The parity equations are obtained by calculating the outputs of the singularly perturbed systems (5) over an horizon $s \in \mathbb{N}^*$, that leads to the following relationship (Chow and Willsky, 1984):

$$\mathrm{Y}(k,s)=\mathrm{H}(s,\varepsilon)\,\mathrm{x}(k-s)-\mathrm{G}(s,\varepsilon)\;\mathrm{U}(k,s)+\mathrm{E}(s,\varepsilon)\;\mathrm{F}(k,s) \quad (6)$$

where: $\mathrm{F}(k,s)=[\mathrm{f}^T(k-s)\ \ \mathrm{f}^T(k-s+1)\ \ \ldots\ \ \mathrm{f}^T(k)]^T$,
$\mathrm{Y}(k,s)=[\mathrm{y}^T(k-s)\ \ \mathrm{y}^T(k-s+1)\ \ \ldots\ \ \mathrm{y}^T(k)]^T$,
$\mathrm{U}(k,s)=[\mathrm{u}^T(k-s)\ \ \mathrm{u}^T(k-s+1)\ \ \ldots\ \ \mathrm{u}^T(k)]^T$,
$\mathrm{G}(s,\varepsilon)=$

$$\begin{bmatrix}0 & 0 & \cdots & \cdots & 0\\ \mathrm{C}(\varepsilon)\,\mathrm{B} & 0 & 0 & \cdots & 0\\ \mathrm{C}(\varepsilon)\,\mathrm{A}(\varepsilon)\,\mathrm{B} & \mathrm{C}(\varepsilon)\,\mathrm{B} & 0 & \cdots & 0\\ \vdots & \vdots & \vdots & \vdots & \vdots\\ \mathrm{C}(\varepsilon)\,\mathrm{A}^{s-1}(\varepsilon)\,\mathrm{B} & \mathrm{C}(\varepsilon)\,\mathrm{A}^{s-2}(\varepsilon)\,\mathrm{B} & \cdots & \mathrm{C}(\varepsilon)\,\mathrm{B} & 0\end{bmatrix}$$

$$\mathrm{H}(s,\varepsilon)=\begin{bmatrix}\mathrm{C}(\varepsilon)\\ \mathrm{C}(\varepsilon)\,\mathrm{A}(\varepsilon)\\ \vdots\\ \mathrm{C}(\varepsilon)\,\mathrm{A}^{s}(\varepsilon)\end{bmatrix}\ \text{and}$$

$\mathrm{E}(s,\varepsilon)=$

$$\begin{bmatrix}\mathrm{E}_2 & 0 & \cdots & \cdots & 0\\ \mathrm{C}(\varepsilon)\,\mathrm{E}_1 & \mathrm{E}_2 & 0 & \cdots & 0\\ \mathrm{C}(\varepsilon)\,\mathrm{A}(\varepsilon)\,\mathrm{E}_1 & \mathrm{C}(\varepsilon)\,\mathrm{E}_1 & \mathrm{E}_2 & \cdots & 0\\ \vdots & \vdots & \vdots & \vdots & \vdots\\ \mathrm{C}(\varepsilon)\,\mathrm{A}^{s-1}(\varepsilon)\;\mathrm{E}_1 & \mathrm{C}(\varepsilon)\,\mathrm{A}^{s-2}(\varepsilon)\;\mathrm{E}_1 & \cdots & \mathrm{C}(\varepsilon)\,\mathrm{E}_1 & \mathrm{E}_2\end{bmatrix}$$

The choice of the horizon s must provide a maximum degree of freedom in designing fault isolation scheme and have to improve its performance (Chow and Willsky, 1984; Li and Shah, 2002). In deterministic case, it is sufficient to set $s = n$ where n is the state dimension, to ensure efficient fault detection algorithm (Maquin and Ragot, 2000).

A parity relation based residual generator can be designed as:

$$\mathrm{R}(k,\varepsilon)=\Omega(\varepsilon)\;\left(\mathrm{Y}(k,s)-\mathrm{G}(s,\varepsilon)\;\mathrm{U}(k,s)\right) \quad (7)$$

The dynamics of residual generator (5) are governed by:

$$\mathrm{R}(k,\varepsilon)=\Omega(\varepsilon)\;\mathrm{E}(s,\varepsilon)\;\mathrm{F}(k,\varepsilon) \quad (8)$$

where: $\mathrm{R}(k,s)$ is the residual signal, $\Omega(k,s)$ is the parity vector which satisfies:

$$\Omega(\varepsilon)\;\mathrm{H}(s,\varepsilon)=0\ \text{ and }\ \Omega(\varepsilon)\;\mathrm{E}(s,\varepsilon)\neq 0 \quad (9)$$

Under the assumption that the system parameters, in absence of fault, do not change, the residual $\mathrm{R}(k,s)$ verifies the following properties:

- $\mathrm{R}(k,s)=0$ in fault free case;
- $\mathrm{R}(k,s)\neq 0$ in presence of fault.

The so generated residual must be independent of the singular perturbation parameter ε to avoid the ill-conditioning and numerical difficulties. To alleviate this ill-conditioning and to reduce the amount of computation, reduction of the residual will be considered.

4. RESIDUAL REDUCTION

The reduction of the full order residual (5) is done by setting the singular perturbation parameter to zero. Eliminating ε from the matrices $\mathrm{G}(s,\varepsilon)$, $\mathrm{H}(s,\varepsilon)$ and $\mathrm{E}(s,\varepsilon)$, we get:

$\mathrm{G}(s,0)=$

$$\begin{bmatrix}0 & 0 & \cdots & \cdots & 0\\ [\mathrm{C}_1\mathrm{B}_1\ \ 0] & 0 & 0 & \cdots & 0\\ [\mathrm{C}_1\mathrm{A}_{11}\mathrm{B}_1\ 0] & [\mathrm{C}_1\mathrm{B}_1\ \ 0] & 0 & \cdots & 0\\ \vdots & \vdots & \vdots & \vdots & \vdots\\ [\mathrm{C}_1\mathrm{A}_{11}^{s-1}\mathrm{B}_1\ 0] & [\mathrm{C}_1\mathrm{A}_{11}^{s-2}\mathrm{B}_1\ \ 0] & \cdots & [\mathrm{C}_1\mathrm{B}_1\ \ 0] & 0\end{bmatrix},$$

$$\mathrm{H}(s,0)=\begin{bmatrix}[\mathrm{C}_1\ \ 0]\\ [\mathrm{C}_1\mathrm{A}_{11}\ \ 0]\\ \vdots\\ [\mathrm{C}_1\mathrm{A}_{11}^{s}\ \ 0]\end{bmatrix}\text{ and}$$

$$\mathrm{E}(s,0)=\begin{bmatrix}\mathrm{E}_2 & 0 & \cdots & \cdots & 0\\ [\mathrm{C}_1\mathrm{E}_1\ \ 0] & \mathrm{E}_2 & 0 & \cdots & 0\\ [\mathrm{C}_1A_{11}\mathrm{E}_1\ \ 0] & [\mathrm{C}_1\mathrm{E}_1\ \ 0] & \mathrm{E}_2 & \cdots & 0\\ \vdots & \vdots & \vdots & \vdots & \vdots\\ [\mathrm{C}_1\mathrm{A}_{11}^{s-1}\mathrm{E}_1\ \ 0] & [\mathrm{C}_1\mathrm{A}_{11}^{s-2}\mathrm{E}_1\ \ 0] & \cdots & [\mathrm{C}_1\mathrm{E}_1\ \ 0] & \mathrm{E}_2\end{bmatrix}$$

The above calculated residual matrices are ε independent, they correspond to the matrices determined using the slow subsystem (3): $\mathrm{H}(k,0)=\mathrm{H}_s(k)$, $\mathrm{G}(k,0)=\mathrm{G}_s(k)$ and $\mathrm{E}(k,0)=\mathrm{E}_s(k)$. Consequently, we get the reduced residual $\mathrm{R}(k,0)$ which matches the slow subsystem based residual $\mathrm{R}_s(k)$: $\mathrm{R}(k,0)=\mathrm{R}_s(k)$. It follows that additive faults diagnosis in discrete-time singularly perturbed system can be achieved using residual generated based on slow subsystem. That leads to the following proposition:

Proposition: Consider the discrete-time singularly perturbed system described by equation (1), the slow subsystem related to the original system is represented by equation (3). Under the assumption that the additive faults attack the system in steady state, additive fault detection and isolation of the original system can be ensured by residual generated based on slow subsystem and using parity space approach. It can be expressed as follows:

$$\mathrm{R}_s(k)=\Omega_s\ (\mathrm{Y}_s(k)-\mathrm{G}_s(s)\,\mathrm{U}_s(k)) \tag{10}$$

where all matrices are calculated based on the slow subsystem.

Consequently, the residual is independent of the singular perturbation parameter ε and generated using the slow subsystem model which order is less than the one of the original singularly perturbed system. By analogy with the commutativity of decomposition and discretization (Kenneth and David, 1992), we have shown that residual generation followed by reduction and system reduction followed by residual generation are commutative operations. This is shown in the following scheme:

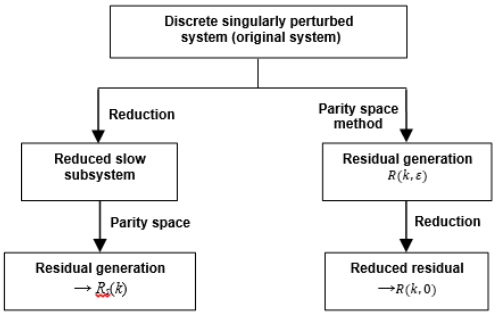

Fig. 1. Commutativity of residual generation and reduction

5. EXAMPLES OF APPLICATION

The following two examples illustrate the effectiveness of the derived diagnosis approach.

5.1. Example 1

The first example is based on a real laboratory two tanks system. We consider the following linear time-invariant discrete-time singularly perturbed system modeling the two tanks system with single input and single output:

$$\begin{cases}\begin{bmatrix}\tilde{\mathrm{x}}_1(k+1)\\ \tilde{\mathrm{x}}_2(k+1)\end{bmatrix}=\begin{bmatrix}0.9991 & 0.0014\,\varepsilon\\ 0.0705 & 7.7766\,\varepsilon\end{bmatrix}\begin{bmatrix}\tilde{\mathrm{x}}_1(k)\\ \tilde{\mathrm{x}}_2(k)\end{bmatrix}+\\ \qquad\qquad\begin{bmatrix}49.7359\\ 3895.1\end{bmatrix}\mathrm{u}(k)\\ \mathrm{y}(k)=[1\quad 0]\begin{bmatrix}\tilde{\mathrm{x}}_1(k)\\ \tilde{\mathrm{x}}_2(k)\end{bmatrix}\end{cases} \tag{11}$$

The discrete slow subsystem is obtained as:

$$\begin{cases}\tilde{\mathrm{x}}_l(k+1)=0.9991\ \tilde{\mathrm{x}}_l(k)+49.7359\,\mathrm{u}_l(k)\\ \mathrm{y}_l(k)=\tilde{\mathrm{x}}_l(k)\\ \tilde{\mathrm{x}}_l(0)=0\end{cases} \tag{12}$$

The residual $R_s(k)$ is generated based on the slow subsystem and using the parity space method. It is governed by:

$$R_s(k)=-5.437*10^{-4}\,y(k-1)+\\ 5.441*10^{-4}\,y(k)+0.0271\,u(k) \tag{13}$$

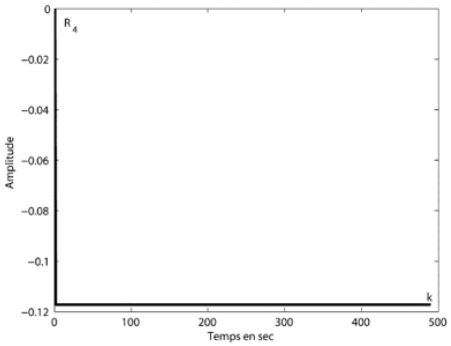

Fig. 2. Evolution of the residual $R_s(k)$ in fault free case

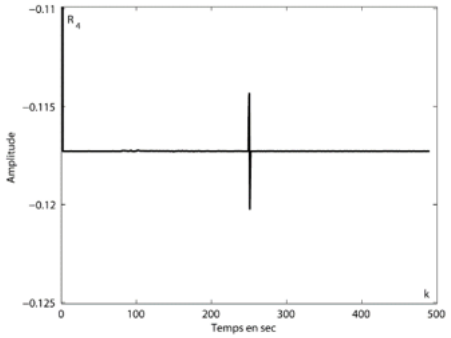

Fig. 3. Residual $R_s(k)$ after fault occurring

The Fig. 2 represents the residual time evolution in the fault free case. It shows that the residual do not presents remarkable deviations. But they take values different from zero, which can be explained by modelling and reduction errors.

The generation of an abrupt sensor fault at time instant 250 seconds leads to the time evolution of the residual $R_s(k)$ illustrated by Fig. 3. It shows a deviation at time 250 sec, which indicates the presence of fault. This result demonstrates that the residual generated based on the slow subsystem is sensitive to sensor additive fault affecting the original singularly perturbed system. This result makes the fault diagnosis of high order systems easier.

The real application is based on a real laboratory application. It is composed of three identical water tanks (see Fig. 4). A detailed model of this application has been presented in (Abdelkrim and Tellili, 2009). Only two tanks are considered.

Fig. 4. Three tanks hydraulic system

The external input flow is considered as control input and The water levels are represented by the states $x_1(t)$ and $x_2(t)$. Using the parity space method, the residual trajectory in the fault free case is shown in Fig. 5.

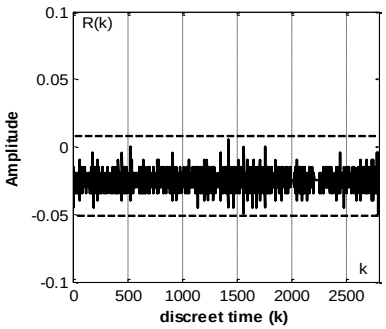

Fig. 5. Real time residual in fault free case

The residual shown in Fig. 5 takes values different from zero in spite of the absence of faults. This is due to several factors as the modelling errors and the disturbances affecting the real system. A threshold will be fixed over the fluctuations to avoid false alarms. A sensor fault is generated at time instance $k = 2500$ (which corresponds to $t = 250\,sec$). The resulting residual behaviour is shown in Fig. 6.

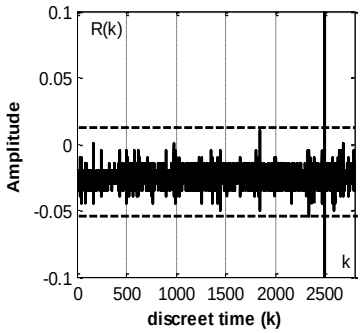

Fig. 6. Real time residual in presence of fault

It is clear on Figs. 5 and 6 that the presence of the fault at time $k = 2500$ induces a residual deviation which exceeds the fixed threshold. These results show that the residual generated on the basis of the discrete-time model, is able to detect the faults affecting the real system.

5.2. Example 2

In this second example, a discrete-time singularly perturbed system with two outputs and one input is considered. It is described by equation (1) with:

$$\mathbf{A}_{11} = \begin{bmatrix} -0.2 & 0.1 \\ 0.1 & -0.2 \end{bmatrix}, \mathbf{A}_{12} = \begin{bmatrix} -1 & 0.2 \\ -1 & 0.4 \end{bmatrix}, \mathbf{B}_1 = \begin{bmatrix} -1 \\ 4 \end{bmatrix},$$

$$\mathbf{A}_{21} = \begin{bmatrix} 0.6 & -0.5 \\ 0.05 & -0.2 \end{bmatrix}, \mathbf{A}_{22} = \begin{bmatrix} -0.1 & 0.03 \\ 0.1 & -0.1 \end{bmatrix}, \mathbf{B}_2 = \begin{bmatrix} 1 \\ 2 \end{bmatrix},$$

$$\mathbf{C}_1 = \begin{bmatrix} -1 & 2 \\ 0 & 2 \end{bmatrix} \text{ and } \mathbf{C}_2 = \begin{bmatrix} -0.1 & 3 \\ 1 & 0.2 \end{bmatrix}.$$

The first simulation depicts how close is the global system output to the slow subsystem output for various values of the singular perturbation parameter ε.

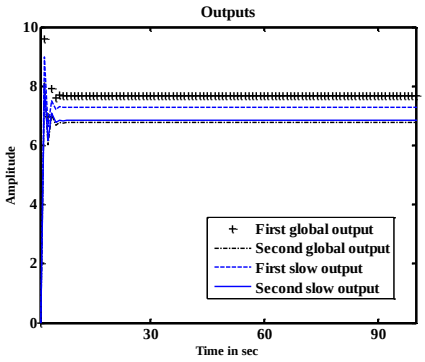

Fig. 7. Global system und slow subsystem outputs by $\varepsilon = 0.1$

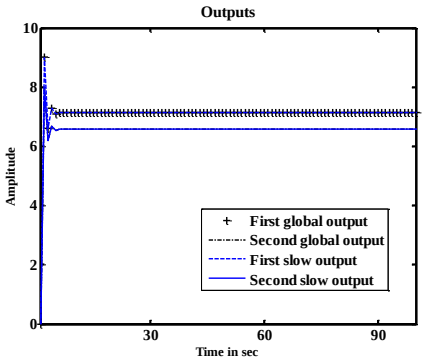

Fig. 8. Global system und slow subsystem outputs by ε=0.001

It is clear in Figs. 7 and 8 that the approximation of the global system with the slow subsystem is better if the singular perturbation parameter ε is smaller. This simulation result is obvious because the slow subsystem is obtained by letting ε to zero. The residual will be then generated using the slow subsystem obtained by applying the singular perturbation method. Knowing that for sufficient small singular perturbation parameter the slow subsystem provides an approximation of the global system, the residual is designed using the slow subsystem matrices and makes use of the global system input and outputs leading to the following residual vector:

$$\mathrm{R}(k)=\begin{bmatrix}\mathrm{R}_{l1}(k)=0.3589\mathrm{y}_1(k)-0.1368\,\mathrm{y}_2(k)+0.9256\,\mathrm{y}_1(k+1)-0.0337\,\mathrm{y}_2(k+1)+0.026\,\mathrm{y}_1(k+2)\\ \quad +0.0155\,\mathrm{y}_2(k+2)-7.9704\,\mathrm{u}(k)-0.3578\,\mathrm{u}(k+1)\\ \mathrm{R}_{l2}(k)=-0.0718\mathrm{y}_1(k)+0.0274\,\mathrm{y}_2(k)+0.0155\,\mathrm{y}_1(k+1)+0.0067\,\mathrm{y}_2(k+1)-0.0052\,\mathrm{y}_1(k+2)\\ \quad +\mathrm{y}_2(k+2)+1.5941\,\mathrm{u}(k)-7.9533\,\mathrm{u}(k+1)\end{bmatrix} \quad (14)$$

The theoretical signature fault matrix, which reflects the residual sensitivity against faults, will be used later to locate the fault (fault isolation). It is given by:

$$\Sigma=\begin{matrix}\\ R_{l1}\\ R_{l2}\end{matrix}\begin{matrix}\begin{matrix}y_1 & y_2 & u\end{matrix}\\ \begin{bmatrix}1 & -1 & -1\\ -1 & 1 & -1\end{bmatrix}\end{matrix} \quad (15)$$

The above mentioned incidence matrix can be interpreted as follow: a positive deviation of the first residual and a negative deviation of the second residual indicates the presence of fault in the first sensor (y_1) and so forth. In the fault free case, the residuals must be close to zero. In fact, Fig. 9 shows the time evolution of the slow subsystem based residuals in absence of failures, there are no deviations.

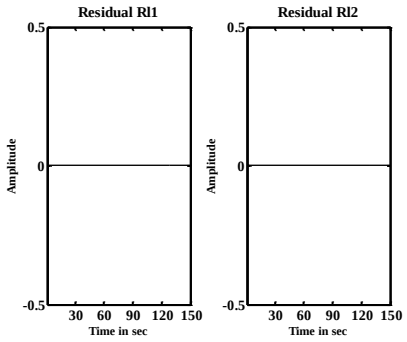

Fig. 9. Residuals in fault free case by $\varepsilon = 0.001$

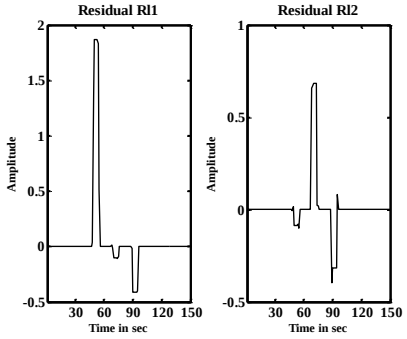

Fig. 10. Residuals in faulty case by $\varepsilon = 0.001$

Three additive faults, modelled by a measurement bias, occur in sensor (y_1) from $t = 50\,\mathrm{sec}$ to $t = 55\,\mathrm{sec}$, in sensor (y_2) between $t = 70\,\mathrm{sec}$ and $t = 75\,\mathrm{sec}$ and finally in actuator (u) from $t = 90\,\mathrm{sec}$ sec to $t = 95\,\mathrm{sec}$. Fig. 10 shows the time evolution of the residuals after fault happening. The values of both residuals at the considered time intervals underline the abnormal behaviour of the global system which indicates the residuals sensitivity towards the considered additive faults.

Once the faults are detected in the plant, the next step is to locate them through the instantaneous fault signatures which reflect the residuals behaviour after fault occurrence and take in this case the following values: $S_{50-55}=\begin{bmatrix}1\\-1\end{bmatrix}$, $S_{70-75}=\begin{bmatrix}-1\\1\end{bmatrix}$ and $S_{90-95}=\begin{bmatrix}-1\\-1\end{bmatrix}$. The comparison between theoretical and instantaneous fault signatures allows accurate fault isolation.

5.3. Interpretation and discussion

The above examples illustrate the developed method for the fault diagnosis of discrete-time singularly perturbed system based on the slow reduced subsystem. The designed algorithm is independent of the singular perturbation parameter ε (equation 14). The developed residuals show deviations further to the occurrence of additive sensor and actuator faults (Fig.10) which allows their detection and isolation.

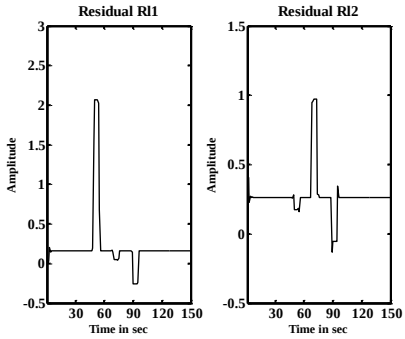

Fig. 11. Residuals in faulty case by $\varepsilon = 0.1$

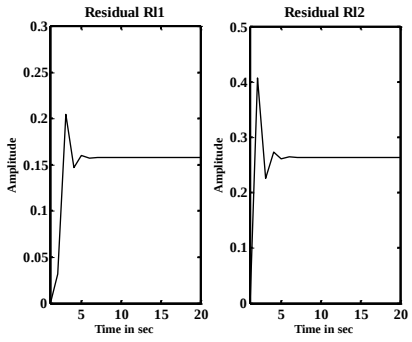

Fig. 12. Residuals in fault free case by $\varepsilon = 0.1$

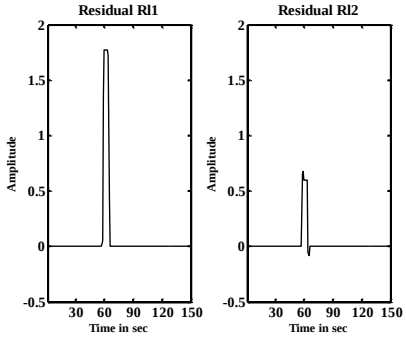

Fig. 13. Residuals in presence of simultaneous sensors faults

However, there are some constraints to respect. First, the singular perturbation parameter must be enough small to guaranty a gut approximation of the global system through the slow subsystem (Figs. 7 and 8); otherwise the residuals cannot be close to zero in absence of faults (risk of false alarm). In this case the residuals remain still sensitive to faults (Fig. 11). The second point concerns the residuals behaviour at the beginning (5 first seconds), they take values different from zero in spite of fault absence, which can lead to false alarms (Fig.12). So during the five first seconds in the second example, it is assumed that no faults happen. Finally the main disadvantage of the used parity space approach is that only failures occurring in different time intervals can be isolated. For example, if additive failures affect simultaneously the first and the second sensor between $t = 50\,\mathrm{sec}$ and $t = 55\,\mathrm{sec}$, the residuals detect the presence of fault during this period but the location of the faulty element using the theoretical and the instantaneous fault signatures is no longer possible (Fig.13).

6. CONCLUSION

In this paper we study model based fault diagnosis of discrete-time singularly perturbed system. The residual is generated using parity space method and depends on the singular perturbation parameter. The ill-conditioning problem of the residual fault generator is solved by the residual synthesis using the slow subsystem. In fact, the reduced order subsystem is independent from singular perturbation parameter and provides an approximation of the original system. A two water tanks application example has shown that the residual generated based on the slow subsystem is able to detect sensor fault occurred in the original singularly perturbed system. A second example is carried out to show the ability of the method to deal with multiple faults.

REFERENCES

1. **Abdelkrim N., Tellili A.** (2009), Model based fault diagnosis of a hydraulic system using singular perturbation approach, *International Review of Automatic Control* (*I.RE.A.CO*), Vol. 2, No. 6, 731-737.
2. **Chow E., Willsky A.** (1984), Analytical redundancy and the design of robust failure detection systems, *IEEE Transactions on Automatic Control*, Vol. 29, No. 7, 603-614.
3. **Clark R. N., Fasth D. C., Walton W. M.** (1975), Detecting instrument malfunctions in control systems, *IEEE Transactions on Automatic Control*, Vol. AES-16, No. 4, 468-473.
4. **Frank P. M.** (1990), Fault diagnosis in dynamic systems using analytical and knowledge-based redundancy, A survey and some new results, *Automatica*, Vol. 26, No. 3, 459-474.
5. **Gertler J.** (1997), Fault detection and isolation using parity relations, *Control Engineering Practice*, Vol. 5, No. 5, 653-661.
6. **Gong F., Khorasani K.** (2005), Fault Diagnosis of Linear Singularly Perturbed Systems, *Proceedings of the 44th IEEE Conference on Decision and Control, and the European Control Conference*, Seville, Spain.
7. **Isermann R.** (1993), Fault diagnosis of machines via parameter estimation and knowledge processing, *Automatica*, Vol. 29, No.4, 815-835.
8. **Kafri W., Abed E.** (1996), Stability analysis of discrete-time singularly perturbed systems, *IEEE Trans. On Circuits and Systems*, Vol. 43, No.10, 848-850.
9. **Kenneth R. S., David G. T.** (1992), On the commutativity of decomposition and discretization for linear singularly perturbed systems, *IEEE Proceedings of the 31st Conference on decision and control*, Arizona.
10. **Khalil H. K.** (1987), Output feedback control of linear two-time-scale systems, *IEEE Transactions on Automatic Control*, Vol. AC-32, No. 9, 784-792.
11. **Kokotovic P., Khalil H., O'Reilly J.** (1986), *Singular perturbation methods in control: analysis and design*, Academic press, Harcourt Brace Jovanovich Publishers.
12. **Li W., Shah S.** (2002), Structured residual vector-based approach to sensor fault detection and isolation, *Journal of Process Control*, Vol. 12, 429-443.
13. **Litkouhi B., Khalil H.** (1985), Multirate and Composite Control of Two-Time-Scale Discrete-Time Systems, *IEEE Transactions on Automatic Control*, Vol. 30, No. 7, 645-651.
14. **Maquin D., Ragot J.** (2000), *Diagnostic des systèmes linaires.* Hermes-science ed., France.
15. **Mease K. D.** (2005), Multiple time-scales in nonlinear flight mechanics: diagnosis and modelling, *Applied Mathematics and Computation*, Vol. 164, No. 2, 627–648.
16. **Naidu D. S., Price D. B., Hibey J. L.** (1987), Singular perturbations and time scales (SPaTS) in discrete control systems-an overview". *Proceedings of the 26th Conference on Decision and Control*, Los Angeles, USA.
17. **Oloomi H., Saif M., Shafai B.** (2004), On the Well Posedness of Singularly Perturbed Fault Detection Filters, *Proceeding of the 2004* American Control Conference Boston, Massachusetts.
18. **Pana C., Stoian V.**, (2008), A fault-tolerant control system for a hexapod mobile robot, *Acta Mechanica et Automatica*, Vol. 2, No. 3, 80-85.
19. **Patton R. J., Chen J.** (1991), A Review of Parity Space Approaches to Fault Diagnosis, *Proceedings of IFAC Symposium on Safeprocess*, Vol. 1, 239-255.
20. **Patton R. J., Chen J.** (1997), Observer-based fault detection and isolation : Robustness and application, *Control Engineering Practice*, Vol. 5, No. 5, 671-682.
21. **Tellili A., Abdelkrim M., Benrjeb M.** (2004), Model-based fault diagnosis of two-time scales singularly perturbed systems, *IEEE Control, Communications and Signal Processing*, 819-822.
22. **Tellili A., Abdelkrim M.N., Benrejeb M.** (2007), Reliable H_∞ control of multiple time scales singularly perturbed systems with sensor failure, *International Journal of Control*, Vol. 80, No. 5, 659-665.

THE IMPACT OF THE FLC CONTROLLER'S SETTINGS ON THE PRECISION OF THE POSITIONING OF A PAYLOAD TRANSFERRED BY A MOBILE CRANE

Jacek KŁOSIŃSKI*, Jarosław JANUSZ*, Rafał NYCZ*

*Faculty of Mechanical Engineering and Computer Science, University of Bielsko-Biała, ul. Willowa 2, 43-309, Bielsko-Biała, Poland

jklosinski@ath.bielsko.pl, jjanusz@ath.bielsko.pl, rafal.nycz@op.pl

Abstract: The paper presents a model of a control system of the slewing motion of a mobile crane in which the FLC controller was used, and then selected results of the numerical simulations of this model were presented. The influence of this controller's settings on the precision with which the payload is positioned after it has been transferred to a target point for different angles of rotation of the jib, different lengths of the rope and different input signals of the controller was investigated.

Key words: Mobile Crane, FLC Controller

1. INTRODUCTION

The oscillations of the payload that is transferred by lifting equipment considerably hinder the work of the device and increase transportation time, especially because of the time that is needed to damp these oscillations, and they may also constitute a threat to the operators and technological facilities that are located in the vicinity of the working equipment (Al-Humaidi and Hadipriono, 2009; Janusz and Kłosiński, 2008; Kłosiński and Majewski, 2009; Kłosiński, 2011). They may also hinder the positioning of the payload after it has been transferred to a target point – this is particularly important when heavy payloads are moved (Cho and Lee, 2002; Neupert et al., 2010; Yi et al., 2003). Therefore, in certain lifting devices control systems are installed. Such systems make it possible to minimise the oscillations of the payload at a target point. These are usually systems that implement a particular strategy of controlling the working motion which ensures that the carried payload stops at a target point and that, at the same time, the payload's oscillations are eliminated. When disturbances appear or the implementation of the adopted control strategy is interrupted, these systems do not ensure minimising the oscillations of the payload at a target point (Lee and Lee, 2002; Tomczyk et al., 2014). The transfer of the payload by using the rotational motion of a lifting device, as is the case with slewing, mobile or tower cranes, causes particular difficulty in this regard. Under these conditions, the use of a fuzzy logic controller seems to be a solution that may ensure higher quality control than classical control methods (Cho and Lee, 2002; Liu et al., 2005; Smoczek, 2014; Smoczek et al., 2013; Smoczek and Szpytko, 2013; Solihin et al., 2010).

This paper presents a model of a control system of the slewing motion of a mobile crane in which the FLC controller was used, and then selected results of the numerical simulations of this model were presented. The influence of this controller's settings on the precision with which the payload is positioned after it has been transferred to a target point for different angles of rotation of the jib, different lengths of the rope and different input signals of the controller was investigated.

2. MODEL OF A CONTROL SYSTEM OF THE WORKING MOTIONS OF A MOBILE CRANE

The analyses of models which are presented in other papers allow one to make assumptions with regard to creating a model of a crane (Hong and Ngo, 2012; Jerman et al., 2004; Ju et al., 2006; Schaub, 2008; Sochacki, 2007; Tereshima et al., 2007). This model is aimed to investigate the slewing motion of a crane's body. The following assumptions have been made (Kłosiński, 2005; Kłosiński and Janusz, 2009):

- the solids of the chassis and the body, of known masses and moments of inertia, are rigid and have six degrees of freedom; the only possible motion of the body in relation to the chassis is its rotation around the vertical axis;
- the support system was substituted with a set of springs; the mass of springs is omitted;
- the crane's body is rotated by means of a hydrostatic drive system through a mechanical gear of known rigidity, the centre of mass of the body lies on the axis of rotation of the body;
- the crane's jib is treated as a rigid bar of constant length, of known mass and moment of inertia; it is connected with the body by means of a cylindrical joint which only allows for a change in the jib's inclination angle;
- the payload hangs on an inextensible, weightless, flexible rope; the hanging payload can be treated as a spherical pendulum;
- the drum of the winch is rotated by means of a hydrostatic drive system through a mechanical gear of known rigidity,
- friction and clearances in all elements of the support system, jib and mechanical gear are not taken into consideration;
- damping in the system is taken into consideration;
- the characteristics of elastic constraints are assumed to be linear,
- three working motions are possible: the slewing motion of the crane's body, luffing as a consequence of a change in the jib's inclination angle which is caused by a change in the length of the hydraulic cylinder as well as the hoisting or lowering

of the payload as a consequence of reeling or unreeling the rope; a simultaneous association of all these motions is permitted;
- all supports of the crane are treated as unilateral constraints, the supports can come off the foundation.

A schematic diagram of the crane's model is presented in Fig. 1.

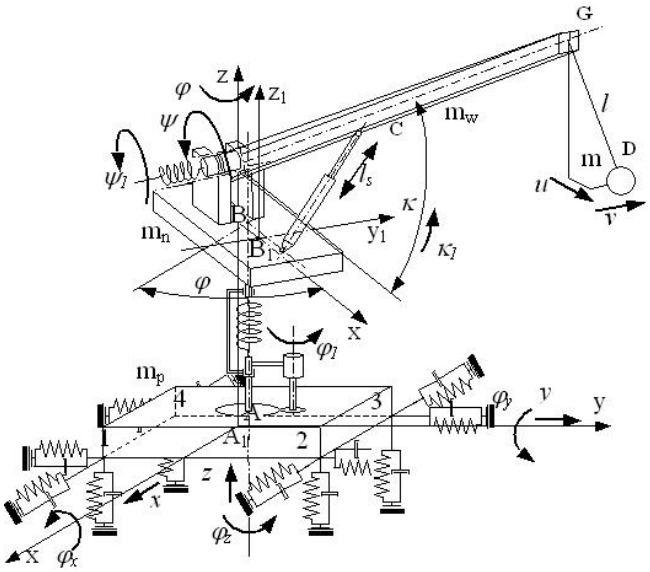

Fig. 1. Schematic diagram of crane model (Kłosiński, 2005)

Generalized co-ordinates of the model are put together in the n-element vector q. Its co-ordinates are as follows:

$$q = [x \ y \ z \ u \ v \ \varphi_x \ \varphi_y \ \varphi_z \ \kappa \ l]^T \tag{1}$$

where: x, y, z – linear displacements of the centre of mass of the chassis which is referred to as a fixed reference system, u, v – projections of the payload's displacement onto a horizontal plane in the radial direction, and in the tangential direction to the circle described by jib's head, respectively; these components are determined in a movable system rotating with the jib, φ – angle of rotation of the body and the jib round a vertical axis, $\varphi_x, \ \varphi_y, \varphi_z$ – angles of oscillation of the crane in reference to the axes that are connected with the centre of mass of the chassis, κ – the jib's inclination angle in reference to the horizontal plane, l – distance from the jib's head to the centre of gravity of the payload.

When calculating the kinetic and potential energies of the system and inserting the obtained formulas into the second-order Lagrange equation, which is written in the form:

$$\frac{\mathrm{d}}{\mathrm{d}t}\left(\frac{\partial E_k}{\partial \dot{q}}\right) - \frac{\partial E_k}{\partial q} + \frac{\partial E_p}{\partial q} + \frac{\partial E_R}{\partial q} = 0 \tag{2}$$

one can write a matrix, non-linear, differential equation in the following form (Kłosiński, 2005):

$$M(q)\ddot{q} = P(\dot{q}, \ddot{q}) \tag{3}$$

where: $M(q)$ – symmetrical block matrix whose elements are functions of masses, the inertial moments of the model's elements and generalized co-ordinates, $P(\dot{q}, \ddot{q})$ – n-element vector whose components are functions of generalized co-ordinates and their derivatives.

This equation can be transformed into an equation in the following form:

$$\ddot{q} = f(\dot{q}, q) + b(q)q_u \tag{4}$$

where: $q_u = [\varphi_1 \quad \kappa_1 \quad \psi_1]^T$, φ_1 – rotational angle of the shaft of the hydraulic motor which is used for putting the crane's body with the jib in slewing motion, κ_1 – inclination angle of the jib's longitudinal axis which is related to the horizontal plane; the axis is determined by two points: the point of vertical rotation of the jib and the point of fixing of the luffing cylinder to the jib, Ψ_1 – rotational angle of the motor-driven drum of the winding machine, $b(q)$ – vector whose components are functions of generalized co-ordinates and stiffness coefficients of elastic elements.

Formula (4) represents a motion equation of the crane model in matrix form describing the slewing motion of its body, changes in the jib reach through changes in the declination of the jib as well as the hoisting or lowering of the payload through winding or unwinding the rope from the drum. The components of the oscillations of the payload as well as the angle of rotation of the body can be calculated by means of the following equations:

$$v = c_1^T q \quad u = c_2^T q \quad \varphi = c_3^T q \tag{5}$$

where:
$c_1 = [0\,0\,0\,0\,1\,0\,0\,0\,0\,0\,0]^T$, $c_2 = [0\,0\,0\,1\,0\,0\,0\,0\,0\,0\,0]^T$,
$c_3 = [0\,0\,0\,0\,0\,1\,0\,0\,0\,0\,0]^T$.

The mathematical models of drive systems that are used for different work motions were derived in a similar way. They were proposed in the form of hydrostatic systems powered by engines with constant absorbing capacity (or by a servo-motor) and proportional valves as the elements which throttle oil flow (Kłosiński, 2005; Kłosiński and Janusz, 2009).

Apart from the equation of these models, i.e. equation (4), and formulas modelling the dynamics of fuzzy logic controller and the equation of the summation point, equations were obtained which were considered a mathematical model of the complete control system. A functional scheme of the control system is presented in Fig. 2 (Janusz and Kłosiński, 2008). In the scheme, the character e was used to describe an error signal which is an input to the controller. The character i describes a vector of variables which control the work of the hydrostatic systems that are used as the drive of a crane; these are usually currents of electro-hydraulic transformers that control hydraulic drive systems which are used in cranes.

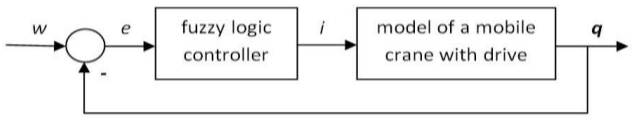

Fig. 2. Functional scheme of control system of mobile crane

3. SIMULATION INVESTIGATIONS OF THE SYSTEM

Numerical investigations of the model were performed for a Mamdani-type fuzzy logic controller (Kłosiński and Majewski, 2004; Kłosiński, 2011; Lee and Lee, 2002; Mahfouf et al., 2000; Pędrak and Kłosiński, 2009) which was used as a controller in the system. For slewing motion the following main elements of the controller can be distinguished:
- fuzzification block; input signals used in the simulation investigations were as follows:

– tangent co-ordinate of payload swings v and the angle distance of the jib from a target point, i.e.: $\Delta\varphi = \varphi_{zad} - \varphi$ or angle distance of the jib from a target point $\Delta\varphi = \varphi_{zad} - \varphi$ and angular velocity;
– fuzzification was performed by using triangular membership functions;
– qualifier block – based on the assumed rule database; a database consisting of 25 reasoning rules was used in the performed numerical simulations (Mahfouf et al., 2000; Pędrak and Kłosiński, 2009),
– defuzzification block – based on the centre-of-gravity method – COS.

Calculations were carried out for the above-mentioned combinations of input signals of the rotation motion controller, different lengths of the rope on which the payload was suspended and different angles of rotation of the jib as well as different values of the coefficients of amplification of particular signals in the controller. The amplification coefficients refer to the input and output signals of the controller. Selected results are presented in the form of graphs in Figs. 3-6.

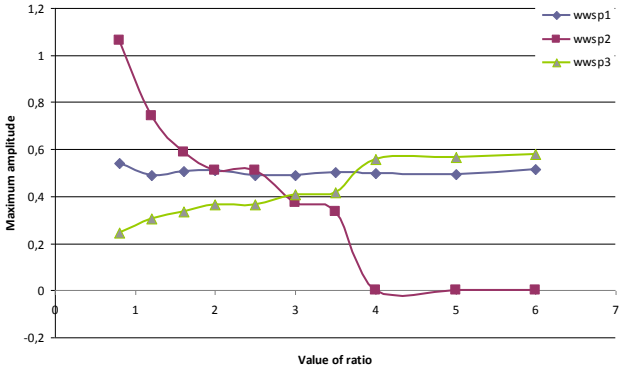

Fig. 3. Diagrams: max amplitude of the payload swings remained after ending of the rotating movement vs amplification coefficient of the controller input (wwsp1, wwsp2) and output (wwsp3) signals ($\varphi_{end} = \mathbf{1.57rad}, \boldsymbol{l} = \mathbf{4m}$)

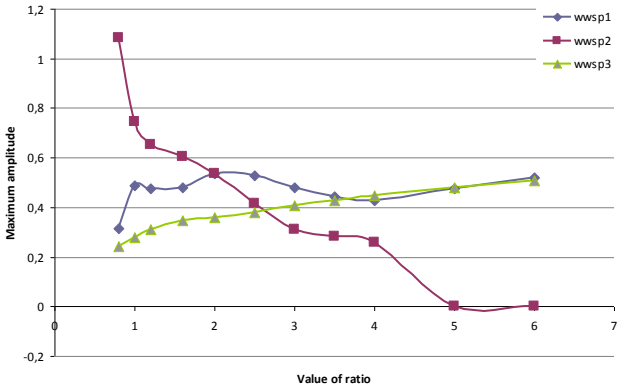

Fig. 4. Diagrams: max amplitude of the payload swings remained after ending of the rotating movement vs amplification coefficient of the controller input (wwsp1, wwsp2) and output (wwsp3) signals ($\varphi_{end} = \mathbf{1.05rad}, \boldsymbol{l} = \mathbf{4m}$)

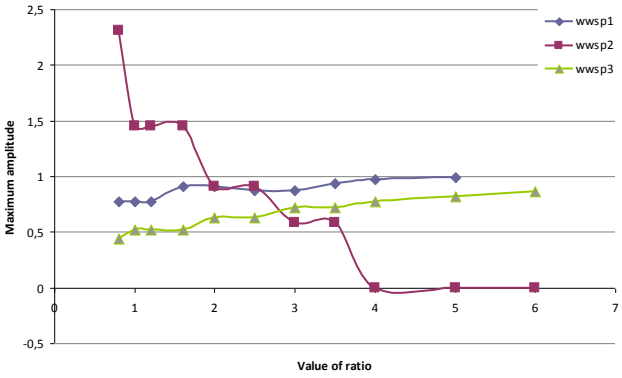

Fig. 5. Diagrams: max amplitude of the payload swings remained after ending of the rotating movement vs amplification coefficient of the controller input (wwsp1, wwsp2) and output (wwsp3) signals ($\varphi_{end} = \mathbf{1.57rad}, \boldsymbol{l} = \mathbf{12m}$)

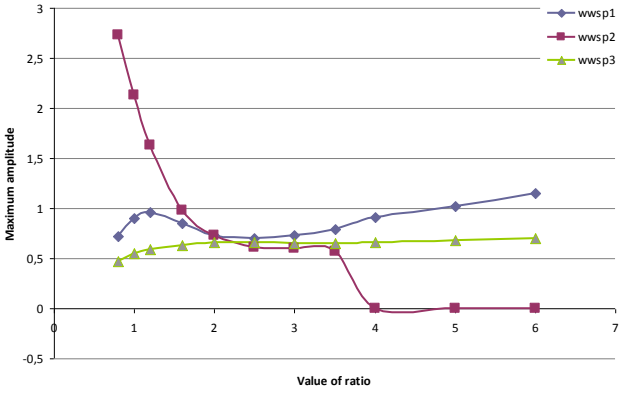

Fig. 6. Diagrams: max amplitude of the payload swings remained after ending of the rotating movement vs amplification coefficient of the controller input (wwsp1, wwsp2) and output (wwsp3) signals ($\varphi_{end} = \mathbf{1.05rad}, \boldsymbol{l} = \mathbf{12m}$)

The graphs showing the dependence of the maximum amplitude of the oscillations of the payload after a rotation and after the jib stops at a target point as a function of signal amplification coefficients in the FLC controller allow one to adopt a satisfactory value of the controller's settings.

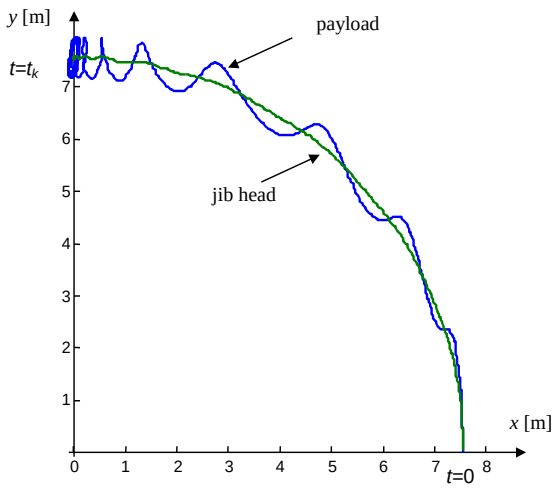

Fig. 7. Trajectories of the jib head and the payload for control system simulation ($\varphi_{end} = \mathbf{1.57rad}, \boldsymbol{l} = \mathbf{4m}$, wws1 = 2, wws2 = 3, wws3 = 7, inputs of controller: 1. $\varphi_{end} - \varphi$; 2.$\dot{\boldsymbol{q}}$)

Moreover, Figs. 7-8 show the trajectories of a crane's motion for a situation in which the operator selects the target point before motion start. These tests were carried out to evaluate the effectiveness of fuzzy logic control.

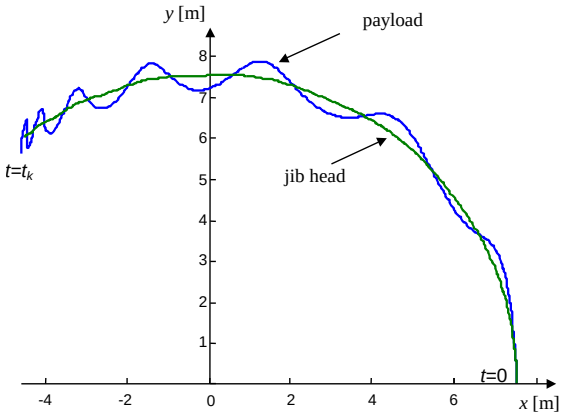

Fig. 8. Trajectories of the jib head and the payload for control system simulation $\varphi_{end} = \mathbf{2rad}$, , $\boldsymbol{l} = \mathbf{4m}$, wws1 = 1, wws2 = 2, wws3 = 1, inputs of controller: 1. $\varphi_{end} - \varphi$; $\mathbf{2}.\boldsymbol{v}$)

4. SUMMARY

Control with the use of the FLC controller eliminates the need to formulate a control strategy before a motion starts and is less sensitive to the disturbances in the implementation of the formulated control strategy. However, such control does not always ensure considerable elimination of the oscillations of the payload remaining after a motion – this is particularly true of the radial component of oscillations, which is mainly generated by a centrifugal inertial force, i.e. a force that acts in a direction for which it is impossible to control motion by only using a rotation drive.

The carried out numerical simulations of the crane model will be used to select the suitable amplification coefficients of the controller as well as to propose the modification of control system in order to achieve to better acuracy of the load positioning after ending the motion.

REFERENCES

1. **Al-Humaidi H. M., Hadipriono Tan F.** (2009), Mobile crane safe operation approach to prevent electrocution using fuzzy-set logic models, *Advances in Engineering Software*, 40, 686-696.
2. **Cho S. K., Lee H. H.** (2002), A fuzzy-logic antiswing controller for three-dimensional overhead cranes, *ISA Transactions*, 41, 235-243.
3. **Hong K. S., Ngo Q. H.** (2012), Dynamics of the container crane on a mobile harbor, *Ocean Engineering*, 53, 16-24.
4. **Janusz J., Kłosiński J.** (2008), Fuzzy controlling of a mobile crane ensuring stable work, *Acta Mechanica Slovaca*, 3-C, 215-222.
5. **Jerman B., Podrzaj P., Kramar J.** (2004), An investigation of slewing-crane dynamics during slewing motion – development and verification of a mathematical model, *International Journal of Mechanical Sciences*, 46, 729-750.
6. **Ju F., Choo Y. S. Cui F. S.** (2006),Dynamic response of tower crane induced by pendulum motion of the payload, *International Journal of Solids and Structures*, 43, 376-389.
7. **Kłosiński J.** (2005), Swing-free stop control of the slewing motion of the mobile crane, *Control Engineering Practice*, 13, 451-460.
8. **Kłosiński J. Majewski L.** (2004), Numerical investigations of the system with fuzzy logic controller used to controlling the working motion of mobile crane, *Proceedings of the IX Conference on the TMM*, Liberec, 445-450.
9. **Kłosiński J., Janusz J.** (2009), Control of operational motions of a mobile crane under a threat of loss of stability, *Solid State Phenomena*, Vol.144, 77-82.
10. **Kłosiński J.** (2011), Fuzzy logic-based control of a mobile crane slewing motion, *Mechanics and Mechanical Engineering*, Vol. 15, No 4, 73-80.
11. **Lee T. Y., Lee S. R.** (2002), Anti-sway and position 3D control of the nonlinear crane system using fuzzy algorithm, *Inter. Journal of the Korean Society of Precision Engineering*, Vol.3, No.1, 66-75.
12. **Liu D., Yi J., Zhao D., Wang W.** (2005), Adaptive sliding mode fuzzy control for a two-dimensional overhead crane, *Mechatronics*, 15, 505-522.
13. **Mahfouf M., Kee C. H., Abbod M. F., Linkens D. A.** (2000), Fuzzy logic-based anti-sway control design for overhead cranes, *Neural Computing & Applications*, 9, 38-43.
14. **Neupert J., Arnold E., Schneider K., Sawodny O.** (2010), Tracking and anti-sway control for boom cranes, *Control Engineering Practice*, 18, 31-44.
15. **Pędrak T., Kłosiński J.** (2009), Control of mobile crane by means of fuzzy logic controller, *Solid State Phenomena*, Vol.144, 202-207.
16. **Schaub H.** (2008), Rate-based ship-mounted crane payload pendulation control system, *Control Engineering Practice*, 16, 132-145.
17. **Smoczek J.** (2014), Fuzzy crane control with sensorless payload deflection feedback for vibration reduction, *Mechanical Systems and Signal Processing*, 46, 70-81.
18. **Smoczek J., Szpytko J**. (2012), Design of gain scheduling anti-sway controller using genetic fuzzy system, *17th IFAC Int. Conf. on Methods and Models in Automation and Robotics MMAR*, 573-578.
19. **Smoczek J., Szpytko J., Hyla, P**. (2013), The anti-sway crane control system with using dynamic vision system, *Solid State Phenomena*, 198, 589-593.
20. **Sochacki W.** (2007), The dynamic stability of a laboratory model of a truck crane, *Thin-Walled Structures*, 45, 927-930.
21. **Solihin M., Wahyudi I., Legowo A.** (2010), Fuzzy-tuned antiswing control of automatic gantry crane, *Journal of Vibration and Control*, 16(1), 127-145.
22. **Terashima K., Shen Y., Yano K.** (2007), Modeling and optimal control of a rotary crane using the straight transfer transformation method, *Control Engineering Practice*, 15, 1179-1192.
23. **Tomczyk J., Cink J., Kosucki A.** (2014), Dynamics of an overhead crane under a wind disturbance condition, *Automation in Construction*, 42, 100-111.
24. **Yi J., Yubazaki N., Hirota K.** (2003), Anti-swing and positioning control of overhead traveling crane, *Information Sciences*, 155,19-42.

NUMERICAL ANALYSIS OF TEMPERATURE FIELD IN A DISC BRAKE AT DIFFERENT COVER ANGLE OF THE PAD

Piotr GRZEŚ*

*Faculty of Mechanical Engineering, Department of Mechanics and Applied Computer Science, Bialystok University of Technology
ul. Wiejska 45C, 15-351 Bialystok, Poland

p.grzes@pb.edu.pl

Abstract: In the paper an influence of the cover angle of the pad on temperature fields of the components of the disc brake is studied. A three-dimensional finite element (FE) model of the pad-disc system was developed at the condition of equal temperatures on the contacting surfaces. Calculations were carried out for a single braking process at constant deceleration assuming that the contact pressure corresponds with the cover angle of the pad so that the moment of friction is equal in each case analysed. Evolutions and distributions of temperature both for the contact surface of the pad and the disc were computed and shown.

Key words: Temperature, Disc Brake, Cover Angle Of The Pad, Finite Element Method

1. INTRODUCTION

High temperature of sliding components of a disc brake in contact may result in deformations/cracks of a disc, degradation of a pad material, brake fluid vaporization, excessive wear of working surfaces, etc. (Ścieszka 1998; Yevtushenko and Grzes, 2010). Numerical calculations of temperature typically employ axisymmetric (Talati and Jalalifar, 2008, 2009; Yevtushenko and Grzes, 2014) or three-dimensional models of a disc brake (Adamowicz and Grzes, 2011a, 2011b, Baranowski et al. 2011, 2013). The first arrangement is used when the sliding velocity is high (uniform temperature distribution in the circumferential direction) or the coefficient of mutual overlap of the pad and the disc is close to the unity. Three-dimensional models allow to reveal non-uniformities on the rubbing path of the disc due to relative motion of the sliding components. However there are also approaches accounting for the three-dimensionality and a uniform distribution of a heat flux density on the contact surface of the disc for calculation of temperature (Ghadimi et al., 2013a) and thermal stresses (Ghadimi et al., 2013b). A review article on FEA of temperature fields in disc brakes and clutches was developed by Yevtushenko and Grzes (2010).

In general brake discs (single or multiple) made as solid, vented, drilled, divided etc., are combined with the pads covering the rubbing path of the disc(s) partly or within the entire circumference (aircrafts). The latter is used to increase the friction force at the same contact pressure. The pad also may be performed as single or multiple (e.g. mine hoist disc brake systems) friction areas per one side of the disc (Scieszka and Zolnierz, 2014). However, currently typical application of a disc brake system for a vehicle consists of two pads with a cover angle of about 60° each and one solid or vented brake disc.

In this study a 3D FE contact model of a disc brake was developed to study an influence of a cover angle of a pad on temperature fields of sliding components. Seven different angles of the pad θ_0 from 40° to 160° were tested for a single braking process at a constant deceleration, corresponding with operating parameters, dimensions, properties of materials of the disc brake of a typical passenger vehicle. Changes in transient distributions of temperature were calculated and compared at the established cover angles of the pad.

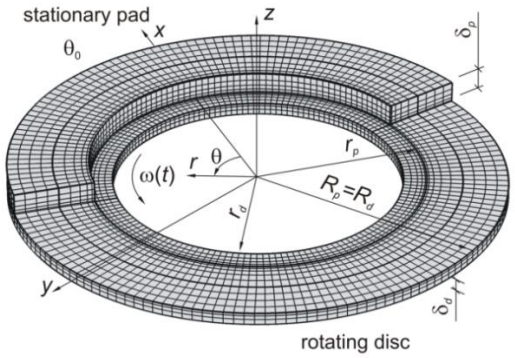

Fig. 1. 3D FE mesh of the pad-disc brake system for $\theta_0 = 160°$

2. BASIC EQUATIONS

Consider a frictional heating of components of a disc brake during a single braking process of a vehicle at constant deceleration from the initial velocity V_0 to standstill according to the formula:

$$V(t) = V_0\left(1 - \frac{t}{t_s}\right), 0 \le t \le t_s, \tag{1}$$

where: t – is time; t_s – is the braking time.

It is assumed that the contact presure p_0 is constant and unifromly distributed on the friction surfaces of the pad and the disc. Convective cooling at the constant heat transfer coefficient takes place on the free surfaces of the pad and the disc apart from the surface/plane of symmetry of the brake disc. Thermal radiation due to short duration of the process was omitted (Adamowicz and Grzes, 2011b).

Three-dimensional temperature fields $T_{p,d}(r,\theta,z,t)$ are calculated from the heat conduction equations for:

– the pad:

$$K_p\Delta T = \rho_p c_p \frac{\partial T}{\partial t},\ r_p < r < R_p,\ |\theta| < 0.5\theta_0 \quad 0 < z < \delta_p,\ \ 0 < t < t_s \tag{2}$$

and the disc:

$$K_d\Delta T = \rho_d c_d \left[\frac{\partial T}{\partial t} + \frac{V(t)}{R_w}\frac{\partial T}{\partial \theta}\right],\ r_d < r < R_d \quad 0 < \theta < 2\pi,\ -\delta_d < z < 0,\ \ 0 < t < t_s \tag{3}$$

at the following boundary conditions:

– within the contact region:

$$K_d \left.\frac{\partial T}{\partial z}\right|_{z=0^-} - K_p \left.\frac{\partial T}{\partial z}\right|_{z=0^+} = q(r,\theta,0,t) \quad (r,\theta) \in \Omega,\ 0 \le t \le t_s \tag{4}$$

$$T(r,\theta,0^+,t) = T(r,\theta,0^-,t),\ (r,\theta) \in \Omega,\ 0 \le t \le t_s \tag{5}$$

where:

$$q(r,t) = p_0 f r R_w^{-1} V(t),\ (r,\theta) \in \Omega,\ 0 \le t \le t_s \tag{6}$$

$$\Delta = \frac{\partial^2}{\partial r^2} + \frac{1}{r}\frac{\partial}{\partial r} + \frac{1}{r^2}\frac{\partial^2}{\partial \theta^2} + \frac{\partial^2}{\partial z^2} \tag{7}$$

K – is the thermal conductivity; c – is the specific heat; ρ – is the density; f – is the coefficient of friction; $r,\ R$ – is the inner and outer radius, respectively; T – is temperature; θ_0 – is the cover angle of the pad; p_0 – is the contact pressure; R_w – is the outer radius of the wheel; Ω – is the contact area; δ – is the thickness; subscripts p and d denote the pad and the disc, respectively.

On the free surfaces of the pad:

$$\mathrm{K_p}\left.\frac{\partial \mathrm{T}}{\partial \mathrm{r}}\right|_{\mathrm{r=r_p}} = \mathrm{h}\left[\mathrm{T(r_p,\theta,z,t) - T_a}\right] \quad |\theta| < 0.5\theta_0,\ 0 < \mathrm{z} < \delta_\mathrm{p},\ 0 \le \mathrm{t} \le \mathrm{t_s} \tag{8}$$

$$\mathrm{K_p}\left.\frac{\partial \mathrm{T}}{\partial \mathrm{r}}\right|_{\mathrm{r=R_p}} = \mathrm{h}\left[\mathrm{T_a - T(R_p,\theta,z,t)}\right] \quad \theta<0.5\theta0,\ 0<z<\delta p,\ 0\le t\le ts \tag{9}$$

$$\mathrm{K_p}\left.\frac{\partial \mathrm{T}}{\partial \theta}\right|_{\mathrm{\theta=-0.5\theta_0}} = \mathrm{h[T(r,-0.5\theta_0,z,t) - T_a]} \quad rp<r<Rp,\ 0<z<\delta p,\ 0\le t\le ts \tag{10}$$

$$\mathrm{K_p}\left.\frac{\partial \mathrm{T}}{\partial \theta}\right|_{\mathrm{\theta=0.5\theta_0}} = \mathrm{h[T_a - T(r,0.5\theta_0,z,t)]} \quad rp<r<Rp,\ 0<z<\delta p,\ 0\le t\le ts \tag{11}$$

$$\mathrm{K_p}\left.\frac{\partial \mathrm{T}}{\partial \mathrm{z}}\right|_{\mathrm{z=\delta_p}} = \mathrm{h}\left[\mathrm{T_a - T(r,\theta,\delta_p,t)}\right] \quad (r,\theta)\in\Omega,\ 0\le t\le ts \tag{12}$$

and the disc:

$$K_d\left.\frac{\partial T}{\partial r}\right|_{r=r_d} = h[T(r_d,\theta,z,t) - T_a] \quad 0 \le \theta \le 2\pi,\ -\delta_d < z < 0,\ 0 \le t \le t_s \tag{13}$$

$$K_d\left.\frac{\partial T}{\partial r}\right|_{r=R_d} = h[T_a - T(R_d,\theta,z,t)] \quad 0 \le \theta \le 2\pi,\ -\delta_d < z < 0,\ 0 \le t \le t_s \tag{14}$$

$$K_d\left.\frac{\partial T}{\partial z}\right|_{z=0^-} = h[T_a - T(r,\theta,0^-,t)] \quad r_d < r < r_p,\ 0 \le \theta \le 2\pi,\ 0 \le t \le t_s \tag{15}$$

$$K_d\left.\frac{\partial T}{\partial z}\right|_{z=0^-} = h[T_a - T(r,\theta,0^-,t)] \quad r_p \le r \le R_p = R_d,\ \theta \ge 0.5\theta_0,\ 0 \le t \le t_s \tag{16}$$

convective cooling takes place.

The surface of symmetry of the disc brake system is insulated:

$$\left.\frac{\partial T}{\partial z}\right|_{z=-\delta_d} = 0\ , r_d \le r \le R_d,\ 0 \le \theta \le 2\pi \quad t \ge 0, z = -\delta_d\ ,\ 0 \le t \le t_s \tag{17}$$

Initially the pad and the disc are at ambient temperature:

$$T(r,\theta,z,0) = T_a,\ r_p \le r \le R_p \quad |\theta| \le 0.5\theta_0,\ 0 \le z \le \delta_p \tag{18}$$

$$T(r,\theta,z,0) = T_a,\ r_d \le r \le R_d \quad 0 \le \theta \le 2\pi,\ -\delta_d \le z \le 0 \tag{19}$$

where: h – is the heat transfer coefficient, T_a – is the ambient/ initial temperature.

3. FE DISCRETIZATION

A considered thermal problem of friction is solved numerically using the finite element method. At the first step the parabolic type heat conduction equations (2), (3) were discretized using the Galerkin's method:

$$[C]\frac{d\{T\}}{dt} + [K]\{T\} = \{Q\} \tag{20}$$

where: $[C]$ – is the capacitance matrix; $\{T\}$ – is the vector of temperature, $[K]$ – is the conductivity matrix, $\{Q\}$ – is the vector of applied thermal loads.

In order to vanish in equation (20) the time derivative of temperature, the finite difference method is used with the betha parameter chosen from the range 0÷1:

$$\frac{1}{\Delta t}[\{T\}_{t+\Delta t} - \{T\}_t] = (1-\beta)\left\{\frac{dT}{dt}\right\}_t + \beta\left\{\frac{dT}{dt}\right\}_{t+\Delta t} \tag{21}$$

Substituting Eq. (21) to Eq. (20) we obtain the following set of algebraic equations:

$$\left[[C] + \beta\Delta t[K]\right]\{T\}_{t+\Delta t} = \left[[C] - (1-\beta)[K]\Delta t\right]\{T\}_t + (1-\beta)\Delta t\{Q\}_t + \beta\Delta t\{Q\}_{t+\Delta t} \tag{22}$$

Computations of temperature in the pad and the disc were carried out using Comsol Multiphysics 4.4 (2013). Based on the geometrical 3D model, the FE mesh was constructed using hex type elements (Fig. 1). A simple geometry of the model allowed to use regular mesh. At the first step, the quad type elements on the contact surface with different distribution in radial direction were built. Then, the plane elements were swept in axial direction for the pad and the disc, respectively. A non-uniform distribution of the elements dimensions applied in the model corresponded with the expected high temperature gradient both in axial and radial directions.

4. NUMERICAL ANALYSIS

Simulation of frictional heating in a pad-disc brake system during a single braking process of a vehicle from the initial velocity $V_0 = 100\ \mathrm{km/h}$ ($\omega_0 = 88.464\ \mathrm{s}^{-1}$) to standstill at constant deceleration $a = -7.015\ \mathrm{m/s^2}$ using FE based software Comsol Multiphysics 4.4 (2013) was carried out. The 3D FE mesh of the model for $\theta_0 = 160°$ is shown in Fig. 1. Initial/ambient temperature is equal $T_a = 20°\mathrm{C}$. Dimensions of the brake components are shown in Tab. 1. The pad is made of FC-16L and the disc is cast-iron ChNMKh (Tab. 2). The materials used are typical for the sliding components of a brake, namely the thermal conductivity of the friction material is several times lower, than the thermal conductivity of the disc. The convective heat transfer coefficient on the free surfaces of the pad and the disc is constant, independent of the velocity $h = 60\ \mathrm{W/(m^2K)}$ (Talati and Jalalifar, 2009).

The main goal of the FEA was to examine the influence of the cover angle of the pad $40° \div 160°$ on the temperature field of the friction pair during the single braking. In each case the work done was equal 392.1 kJ. To maintain the same moment of friction, the pressure was changed. For the automotive application, the cover angle of the pad equals approximately 60°, however e.g. in aircrafts the friction surface of the pad is consistent with the friction surface of the disc (rubbing path) 360°.

Tab. 1. Dimensions of the pad and the disc (Talati and Jalalifar, 2009)

dimension	pad	disc
inner radius, $r_{p,d}$ [m]	0.0765	0.066
outer radius, $R_{p,d}$ [m]	0.1135	0.1135
thickness $\delta_{p,d}$ [m]	0.01	0.0055
cover angle of the pad, θ_0 [deg]	40, 60, 80, 100, 120, 140, 160	

Tab. 2. Thermophysical properties of materials of the pad and the disc (Chichinadze et al., 1986)

thermophysical properties	FC-16L (pad)	cast iron ChNMKh (disc)
thermal conductivity, K [W/(mK)]	0.79	51
specific heat, c [J/(kgK)]	961	500
density, ρ [kg/m^3]	2500	7100

In order to identify the location of the maxiumum temperature in the pad-disc system, the distribution of temperature on the contact surface of the disc was analysed for $\theta_0 = 40°$ and $160°$ (Fig. 2). As expected, the temperature field is non-uniform both within the contact region and on the free surface for these two angles. The location of maxiumum temperature appears approximately for $r = R_d$ and $\theta = 0.5\theta_0$, which results from the direction of revolution of the disc and the applied heat flux density (Eq.(6)). Noticeable is the fact that the temperature for $\theta_0 = 160°$ is almost uniform in circumferential direction whereas for $40°$ the maxiumum temperature under the pad is higher.

Temperature distributions for $\theta_0 = 40° \div 160°$ on the outer edge of the constact surface of the disc at the moment of half of the braking time ($t = 2\ \mathrm{s}$) are shown in Fig. 3. The main difference is the maxiumum temperature reached, higher for smaller cover angle of the pad. The temperature out of the pad area is almost equal for each θ_0 presented.

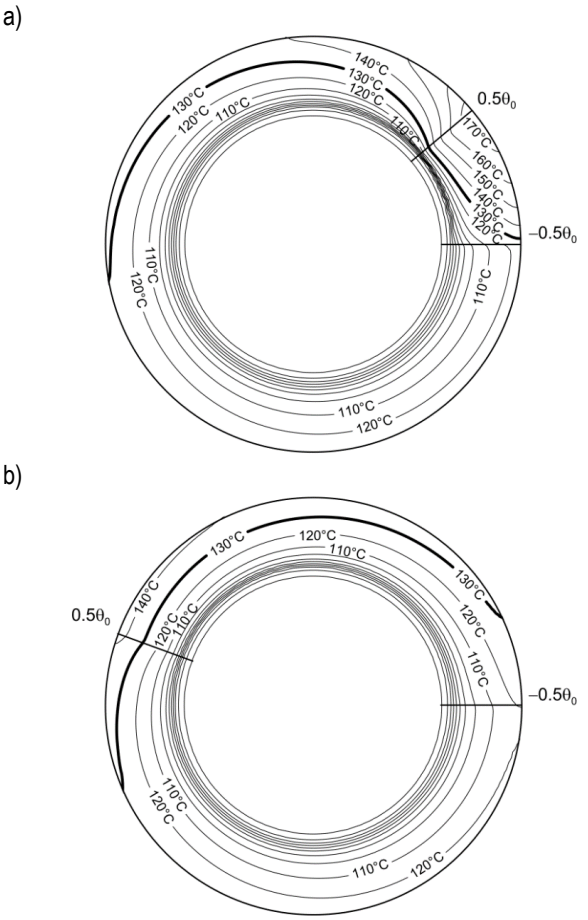

Fig. 2. Temperature distributions on the contact surface of the disc at the time moment ($t = 2\ \mathrm{s}$) for the cover angle of the pad: a) $\theta_0 = 40°$ and b) $\theta_0 = 160°$

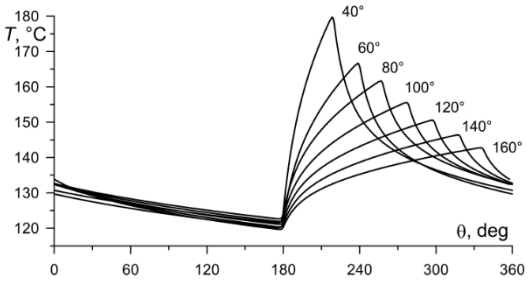

Fig. 3. Distributions of temperature in the circumeferential direction on the outer edge of the friction surface of the disc $r = R_d$ at different cover angles of the pad θ_0 ($t = 2\ \mathrm{s}$)

In this numerical analysis, the pad is fixed and the disc is rotating. Therefore it is convenient to analyse the temperature in the stationary region of the pad. The evolutions of the maximum temperature on the contact surface of the pad ($r = R_p$, $z = 0$, $\theta = 0.5\theta_0$ and $\theta = -0.5\theta_0$ are smooth (Fig. 4). At the beginning of the process the temperature increases, attaines the maxiumum value and decreases until the moment of standstill. However the temperature differences for variable angle are sllight, it may be observed that the lowest temperature is reached for the angle of the pad of $160°$.

It should be noted that the braking process for each angle is consistent, namely the friction force is the same irrespective of the angle θ_0. Thus the temperature calculated may be confronted and compared indicating the best geometrical configuration. Obviously when θ_0 is greater the force possible to apply would be higher.

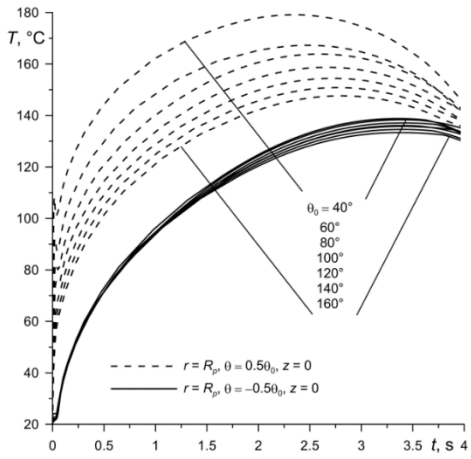

Fig. 4. Temperature evolutions on the contact surface of the pad $r = R_p,\ z = 0$ at $\theta = 0.5\theta_0$ and $\theta = -0.5\theta_0$

The presented in Fig. 4 evolutions for two point locations on the outer edge of the pad show the amplitude of oscilations of temperature of the disc presented in Fig. 5. Unlike the contact temperature of the pad, in Fig. 5 we can see the periods of frictional heating and dissipation of heat through conduction and convection to the surrounding air. An interesting is the fact that the minimum value of the oscilations through the enitre process is almost equal for each angle of the pad, wheras the maxiumum temperature is clearly higher for smaller cover angle of the pad. This relationship speaks for using greater angle of the pad.

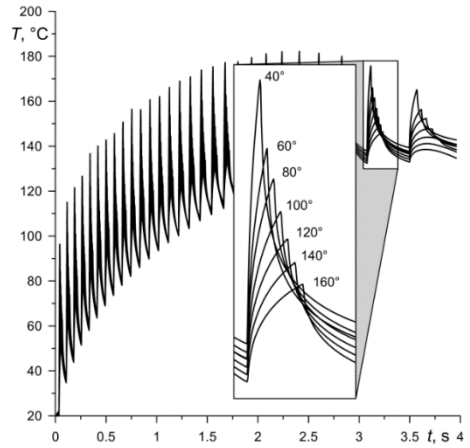

Fig. 5. Temperature evolutions on the contact surface of the disc $(r = R_d)$ at different cover angles of the pad θ_0

5. CONCLUSIONS

In this paper temperature fields of the components of the disc brake at different cover angle of the pad θ_0 were studied. Varying the contact pressure, for each θ_0 the friction force was equal in order to maintain the work done also equal. Based on the obtained temperature distributions and their changes during the single braking, the following conclusions were drawn:

- the maximum temperature of the pad-disc interface is reached for the smallest θ_0;
- the difference between the maximum temperatures for the corresponding points in braking time at different cover angles of the pad is slight; the lowest difference occurs at the moment of standstill (Figs. 4, 5);
- for each studied cover angle of the pad the maximum temperature of the disc at the end of braking was approximately equal (Fig. 5).

The obtained results show that there is a clear relationship between the maximum temperature and the cover angle of the pad. However it is known, that typically the pad does not cover the rubbing path of the disc entirely. This may result from more complex caliper geometry necessary to approve uniform pressure distribution on the contact surface when increasing the θ_0.

REFERENCES

1. **Adamowicz A., Grzes P.** (2011a), Analysis of disc brake temperature distribution during single braking under non-axisymmetric load, *Applied Thermal Engineering*, Vol. 31, No. 6-7, 1003-1012.
2. **Adamowicz A., Grzes P.** (2011b), Influence of convective cooling on a disc brake temperature distribution during repetitive braking, *Applied Thermal Engineering*, Vol. 31, No. 14-15, 2177-2185.
3. **Baranowski P., Damaziak K., Małachowski J.** (2013) Brake system studies using numerical methods, *Maintenance and Reliability*, Vol. 15, No. 4, 337-342.
4. **Baranowski P., Damziak K., Malachowski J., Mazurkiewicz L., Kastek M., Piatkowski T., Polakowski H.** (2011), Experimental and numerical tests of thermo-mechanical processes occurring on brake pad lining surfaces, Surface Effects and Contact Mechanics X, *Computational Methods and Experiments*, Edited By: J.T.M. DE HOSSON, University of Groningen, Netherlands and C.A. Brebbia, Wessex Institute of Technology, UK, Vol. 71, 15-24.
5. **Chichinadze A. V., Matveevski R.M., Braun E. P.** (1986), *Materials in tribotechnics non-stationary processes*, Nauka, Moscow (in Russian).
6. **COMSOL Multiphysics 4.4**, *Heat Transfer Module User's Guide*, 1998-2013.
7. **Ghadimi B., Kowsary F., Khorami M.** (2013a) Thermal analysis of locomotive wheel-mounted brake disc, *Applied Thermal Engineering*, Vol. 51, No. 1-2, 948-952.
8. **Ghadimi B., Sajedi R., Kowsary F.** (2013b) 3D investigation of thermal stresses in a locomotive ventilated brake disc based on a conjugate thermo-fluid coupling boundary conditions, *International Communications in Heat and Mass Transfer*, Vol. 49, 104-109.
9. **Ścieszka S. F.** (1998) Friction brakes – material, structural and tribological problems, ITE, Radom (in Polish).
10. **Scieszka S. F., Zolnierz M.** (2014), Experimental and numerical investigations of thermo-mechanical instability of the industrial disc brakes, Proceedings of the Institution of Mechanical Engineers, Part J: *Journal of Engineering Tribology*, Vol. 228, No. 5, 567-576.
11. **Talati F., Jalalifar S.** (2008), Investigation of heat transfer phenomena in a ventilated disk brake rotor with straight radial rounded vanes, *Journal of Applied Sciences*, Vol. 8, No. 20, 3583-3592.
12. **Talati F., Jalalifar S.** (2009), Analysis of heat conduction in a disk brake system, *Heat and Mass Transfer*, Vol. 45, 1047-1059.
13. **Yevtushenko A.A., Grzes P.** (2010), The FEM-modeling of the frictional heating phenomenon in the pad/disc tribosystem (a review). *Numerical Heat Transfer Part A-Applications*, Vol. 58, 207-226.
14. **Yevtushenko A.A., Grzes P.** (2014) Mutual influence of the velocity and temperature in the axisymmetric FE model of a disc brake, *International Communications in Heat and Mass Transfer*, Vol. 57, 341-346.

The work has been accomplished under the research project No. MB/WM/8/2014 at the Bialystok University of Technology.

THE IMPACT OF THE SUPPORT SYSTEM'S KINEMATIC STRUCTURE ON SELECTED KINEMATIC AND DYNAMIC QUANTITIES OF AN EXPERIMENTAL CRANE

Arkadiusz TRĄBKA*

*Faculty of Mechanical Engineering and Computer Science, Department of Engineering Fundamentals, University of Bielsko-Biala, ul. Willowa 2, 43-309 Bielsko-Biała, Poland

atrabka@ath.bielsko.pl

Abstract: This paper presents a comparative analysis of two kinematic structures of the support system (with supports with bilateral and unilateral constraints), which were used in an experimental model of a crane. The computational model was developed by using the ADAMS software. The impact of the kinematic structure of the support system on selected kinematic and dynamic values that were recorded during the slewing motion was analysed. It was found, among other things, that an increased number of degrees of freedom of the support system leads to multiple distortions of time characteristics of kinematic and dynamic quantities.

Key words: Experimental Crane, Multi-Body Systems, Supports, Unilateral Constraints, Bilateral Constraints

1. INTRODUCTION

Cranes are complex mechatronic systems whose operation reveals different types of constructional and technological problems as well as problems related to controlling cranes' operation (Trąbka, 2014). Many scientific papers were written in order to find the answers to the above-mentioned problems. Their authors most often used numerical models to analyse real structures. The models and the results of analyses were verified either by using computational models that had been developed based on other methods (Cha et al., 2010; Geisler and Sochacki, 2011; Paszkiewicz et al., 1999) or by using experimental models that had been constructed especially for this purpose (Jerman et al., 2004; Kłosiński, 2005; Maczyński, 2000; Smoczek, 2014; Smoczek and Szpytko, 2012; 2014; Sochacki, 2007; Terashima et al., 2007; Uchiyama, 2009; Uchiyama et al., 2013; Wu, 2006). Verification tests were conducted on real objects less frequently due to their high costs (Araya et al., 2004; Blackburn et al., 2010; Kilicaslan et al., 1999; Mijailović, 2011; Sosna, 1984; Trąbka, 2014).

Experimental models should have the same properties as the structures based on which these models have been developed (or properties that are as similar as possible to the properties of such structures). The models should be similar to real structures in terms of geometry, kinematics and dynamics in order to meet these conditions (Trombski, 2003). Since it is very difficult to meet all of the above criteria at the same time, certain construction solutions that are used in experimental models (for example, a crane's supports fastened to the ground) may raise concerns as to whether the properties of real objects are mapped correctly.

This paper presents a computational model of a mobile crane with a telescopic boom which was developed based on an experimental crane in which two variants of the kinematic structure of the support system were used. What was analysed was how the selection of a kinematic structure of the support system (with supports with unilateral or bilateral constraints) influences selected kinematic and dynamic quantities of the crane.

2. COMPUTATIONAL MODEL OF AN EXPERIMENTAL CRANE

The computational model was developed by using multi-body system analysis software ADAMS based on the real structure of an experimental crane (Fig. 1).

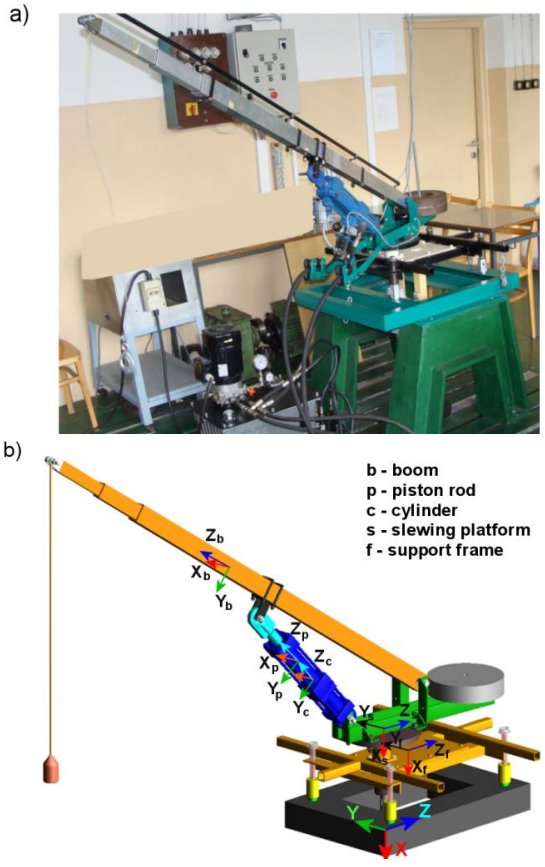

Fig. 1. a) Experimental crane, b) Computational model

The model included the majority of a crane's structural components, which were assumed to be non-deformable except for the supports and the rope. Two variants of the computational model were developed. In variant V1 the kinematic structure of a support system with supports having bilateral constraints was used (Fig. 2a) whereas in variant V2 supports with unilateral constraints were used (Fig. 2b).

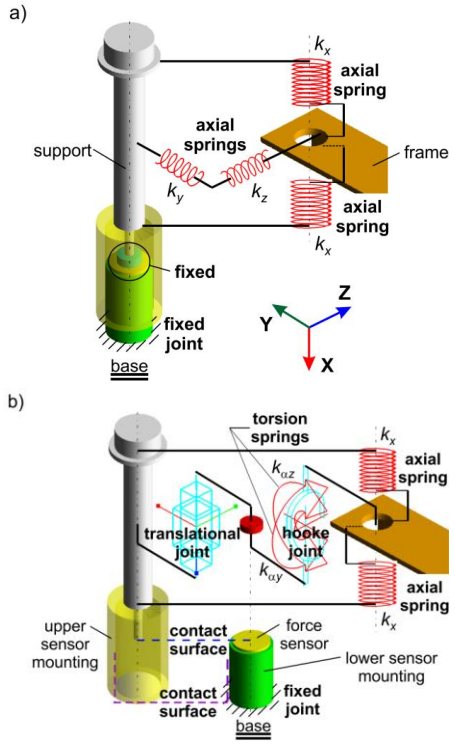

Fig. 2. Supports with: a) bilateral constraints (V1), b) unilateral constraints (V2)

The dimensions, masses and mass moments of inertia of the model's parts were determined based on the measurements of a real structure and the geometrical models of these parts which had been developed by using the Inventor software (Tab. 1).

The stiffnesses and dampings of the axial springs that were used to model the supports were determined experimentally. Since the same set of eight compression springs was used in both variants of the experimental crane to construct the supports, and all these springs came from the same production batch, it was decided that the same stiffness k_x should be adopted for all of the axial springs in the computational model. This stiffness was determined for a spring which had been randomly selected from the set of springs based on a series of 10 measurements of the dependence of deformation on the load, which were made by using a universal testing machine FP10. For each dependence of deformation on the load an average stiffness k_N was calculated based on equation (1) and then a substitute stiffness $k_x = 17.25 \times 10^3 \mathrm{N/m}$ was determined by using equation (2).

$$k_N = \frac{1}{m} \cdot \sum_{i=1}^{i=m} \frac{\Delta P_i}{\Delta l_i} \tag{1}$$

$$k_x = \frac{1}{s} \cdot \frac{1}{n} \cdot \sum_{N=1}^{N=n} k_N \tag{2}$$

where: N – measurement no., m – number of changes in a spring load, $s = 2$ – number of springs that are connected in parallel to each other in the crane support's model, n – number of measurements, ΔP_i – i-th change in the load carried by a spring, Δl_i – i-th change in a spring's length.

Damping coefficients c_u in the supports (systems of springs) were determined for the directions of the X, Y and Z axes of a reference frame by using the free vibration method. The damping coefficients were calculated by using equation (3) based on the changes in the position of the support frame over time with respect to the base (Giergiel, 1986).

$$c_u = \frac{2 \cdot M \cdot \delta}{T} \tag{3}$$

where: M – mass of the system of supports which depends on the location of the sensor of displacements and the direction of movement, δ – logarithmic damping decrement, T – period of damped vibration.

For every direction of movement 10 measurements were carried out and the average damping coefficients c_s were calculated based on these measurements. In the computational model a damping coefficient was assigned to each of the springs; such a damping coefficient was reduced in relation to the calculated average value proportionately to the number of the supports that were located in the area of the frame's recorded movement as well as to the number of springs that were connected in parallel to each other in a support. Finally, the following values were adopted for calculations: $c_{sx} = 0.277 \times 10^3 \mathrm{N \cdot s/m}$, $c_{sy} = 0.47 \times 10^3 \mathrm{N \cdot s/m}$, $c_{sz} = 0.59 \times 10^3 \mathrm{N \cdot s/m}$.

Apart from axial stiffnesses of the springs which were determined experimentally, also the stiffnesses of systems of springs, perpendicular to their axes, were taken into account. Lateral stiffnesses of the systems of springs $(k_y = k_z = 114 \times 10^3 \ \mathrm{N/m})$ were determined numerically; both the computational model and the calculations themselves were carried out by using the Ansys v11 software and following a method described in Kłosiński and Trąbka (2010).

Tab. 1. Masses and mass moments of inertia of the model's parts

Name of a given part	Mass [kg]	Mass moments of inertia with respect to the centres of masses of the model's parts [kg·m²]		
		J_{sx}	J_{sy}	J_{sz}
Support frame	17.3	0.792	0.567	0.235
Slewing platform	20.2	0.688	0.706	0.128
Boom	4.5	0.937	0.936	0.0025
Piston rod	3.7	0.068	0.067	0.0008
Cylinder	11	0.21	0.21	0.01

Torsion springs were added to the computational model for supports with unilateral constraints. Each of the support screws was connected to the support frame with two torsion springs. They were placed on planes that were parallel to planes XY and XZ of the frame of reference. The stiffnesses of torsion springs were determined experimentally based on tests of the dependence of the support's angle of rotation on the support frame as a function of the torsional moment. The same value of stiffness for all of the supports was adopted $(k_{ay} = k_{az} = 78.2 \ \mathrm{N \cdot m/deg})$.

At the points of contact between support screws and force sensors, contact joints were applied. As for these joints, the possibility of friction was taken into account (the Coulomb friction model was used).

3. NUMERICAL ANALYSIS OF THE MODEL

3.1. Assumptions for the calculations

- The model's initial position corresponds to a crane being in a state of static equilibrium; the initial tension of springs was taken into account;
- Flexibilities, clearances and friction in joints between the model parts were not taken into account;
- Flexibilities, clearances and friction in the drive were not taken into account; a constant value of the reduction gear ratio $i = 20$ was adopted;
- The rope's flexibility and the flexibility of the luffing hydraulic cylinder were not included in the model;
- A constant step of integration was 0.001 s.

3.2. Calculations

Calculations were carried out for two configurations of the model.

Configuration 1 included a boom inclined to the level at an angle of 22º, a crane radius of 1.64 m, a load of 3 kg and a counterweight of 45 kg.

Configuration 2 included a boom inclined to the level at an angle of 35º, a crane radius of 1.43 m, a load of 1 kg and a counterweight of 17 kg.

In both cases the distance between the centre of mass of the load and the point where the rope was attached to the boom was 1 m. The rotation angle of the body relative to the chassis was 90º. The kinematic input function was used for the slewing motion. The forms of the functions that were used to describe the input functions are presented in Fig. 3.

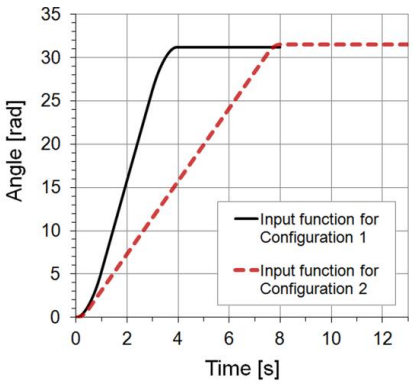

Fig. 3. Slewing motion input functions for both model configurations

The calculations were started by checking the correctness of the computational model. In order to do this, first it was checked whether there were no redundant constraints in the model; afterwards, the model was verified. Verification was conducted for both configurations by comparing the calculated support loads with the loads that were recorded during the tests. The results of the comparison for configuration 2, variant V2, are shown in Fig. 4. It was found that the model properly mapped the real object and the visible differences between characteristics were due to the omission of the flexibilities of particular parts as well as the flexibilities of connections, the friction and clearances in the connections, and most of all due to the omission of clearances in the drive.

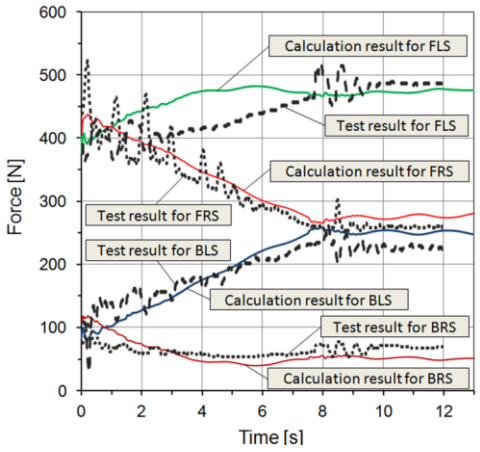

Fig. 4. A comparison of support loads for configuration 2, variant V2 with the loads that were recorded during the tests (BLS – back left support, BRS – back right support, FLS – front left support, FRS – front right support)

3.3. Results and discussion

This paper presents an evaluation of the impact of the kinematic structure of the support system on the trajectory of the load, the speed of rotation of the body relative to the chassis and the support loads.

Calculation results for configuration 1 of the computational model are presented in Fig. 5. A dashed line was used for variant V1 of the model and a solid line was used for variant V2. Fig. 5a presents the trajectory of the centre of mass of the load and Fig. 5b shows the changes in the speed of rotation of the body relative to the chassis. The distribution of the support loads is shown in Fig. 5c whereas Fig. 5d presents a quantitative comparison of the changes in variant V2 support loads in relation to variant V1.

The calculation results for configuration 2 of the computational model are presented in the next four figures (Figs. 6a-d) in the same way as for configuration 1.

Based on the calculation results (Figs. 5-6) it was found that:

- A change in the kinematic structure of the support system does not lead to significant differences in the load's trajectory regardless of the configuration and input functions.
- The speed of rotation of the body relative to the chassis is non-linear for both variants of the model in configuration 1 and for variant V2 in configuration 2. Moreover, this speed undergoes constant changes and these changes are considerably greater for variant V2 than for variant V1.
- The changes in the speed of rotation of the body are closely related to the vibration of the support frame which is caused by the horizontal displacement of the supports. Due to the additional degrees of freedom these vibrations have larger amplitudes and cause greater speed changes for variant V2.
- An increased number of the degrees of freedom of the support system, in particular the introduction of the possibility of the supports sliding against the base, contributes to the occurrence of short-term (impulsive) variations in the support loads.
- The maximum increase of the support loads, which is related to the change in their kinematic structure, does not exceed 14.7% for configuration 1 (Fig. 5d) and 13% for configuration 2 (Fig. 6d).

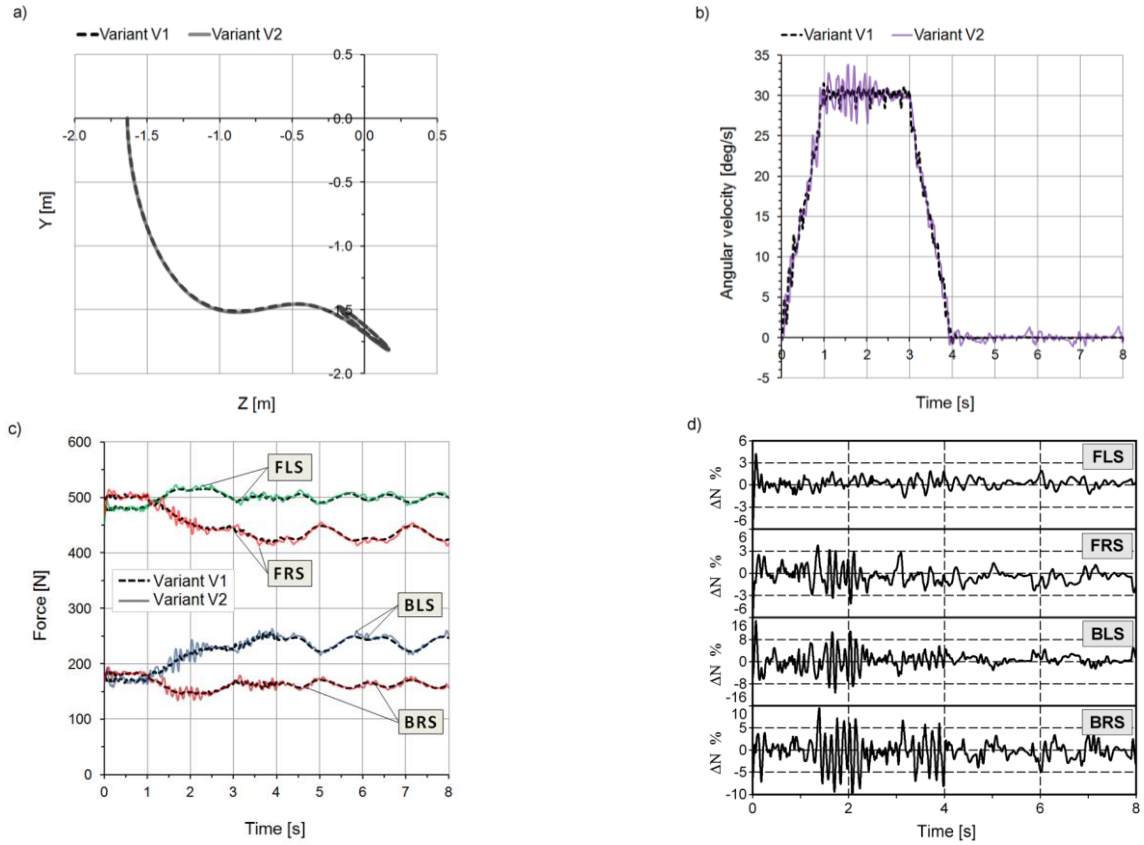

Fig. 5. Calculation results for configuration 1: a) a trajectory of the centre of mass of the load, b) the speed of rotation of the body relative to the chassis, c) a distribution of the support loads, d) a percentage comparison of the changes in variant V2 of support loads (ΔN) in relation to variant V1 (FLS – front left support, FRS – front right support, BLS – back left support, BRS – back right support)

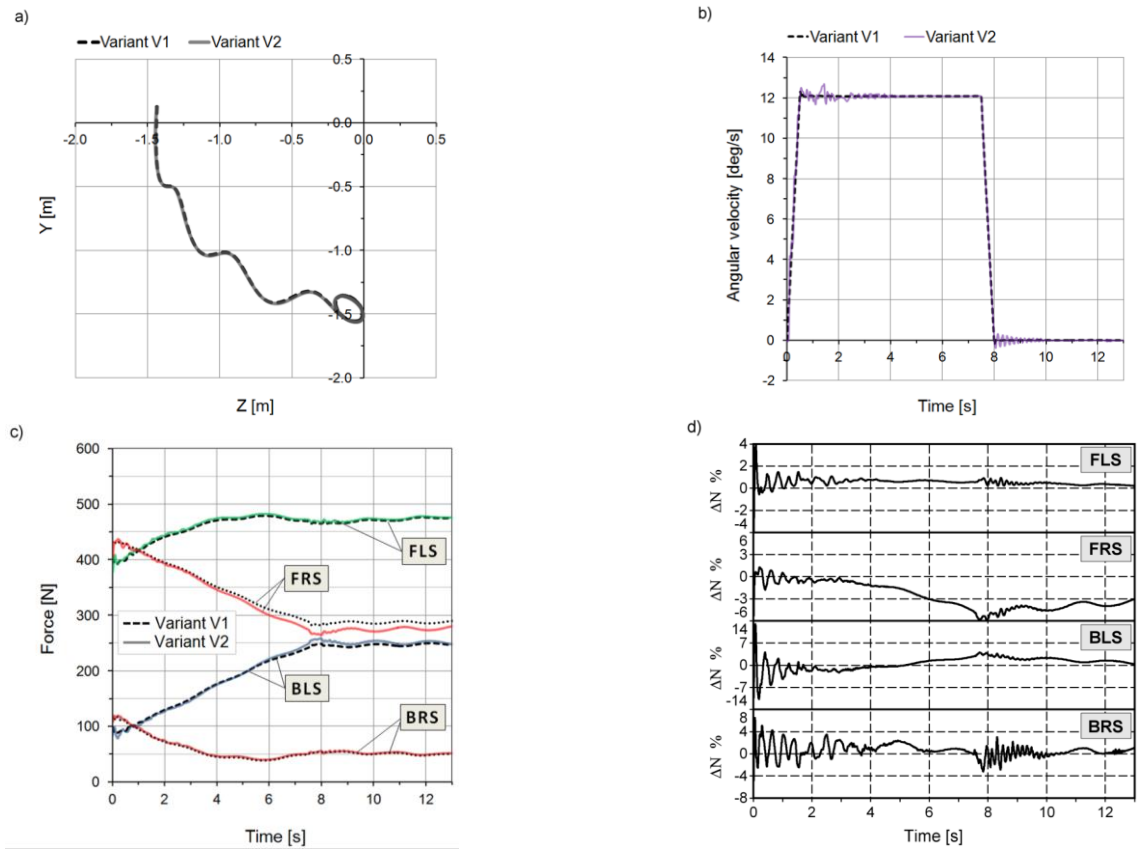

Fig. 6. Calculation results for configuration 2: a) a trajectory of the centre of mass of the load, b) the speed of rotation of the body relative to the chassis, c) a distribution of the support loads, d) a percentage comparison of the changes in variant V2 of support loads (ΔN) in relation to variant V1 (FLS – front left support, FRS – front right support, BLS – back left support, BRS – back right support)

4. SUMMARY AND CONCLUSIONS

This paper presents the results of numerical analyses of the computational model of an experimental crane which were carried out in order to evaluate the impact of the support system's kinematic structure on selected kinematic and dynamic quantities of a crane. Two variants of the model were developed – one with supports with bilateral constraints (V1) and the other with supports with unilateral constraints (V2). The stiffnesses and dampings of the supports were determined experimentally. The model did not include flexibilities or clearances in the connections, except for the supports.

On the basis of the numerical analyses, it was found that:

- A support system with unilateral constraints introduces multiple distortions of time characteristics of the monitored kinematic and dynamic quantities. These distortions are caused by the possibility of the supports moving relative to the base (slides in the clearance area) and by impact loads which are caused by the interaction between mountings of force sensors (the upper one is connected to the support screw and the lower one to the base). The maximum excess of the support loads, which is due to the above-mentioned causes (Fig. 5d), does not exceed 14.7% of the value which was obtained for a system with supports with bilateral constraints.
- The time characteristics of selected kinematic and dynamic quantities which were obtained for variant V1 of the model, with the same input functions as those which were used for variant V2, are almost completely free from distortions. At subsequent moments of time, particular kinematic and dynamic quantities assume values which correspond to the average values that were determined for the model with unilateral constraints.
- Although a support system with supports having bilateral constraints is inconsistent with a crane's real support system, it can be used in experimental models. Both kinematic and dynamic quantities assume proper values for this variant of the model under the condition that the input functions that are used for the motion are chosen so that the structure does not lose its stability (so that no fictitious forces appear in the model).
- On the basis of the calculations it was found that an increase in the coefficient of friction between support screws and the base has a positive influence on the dynamic loads of the supports – distortions of time characteristics are less frequent and the load changes of the supports are smaller relative to the loads in the system with bilateral constraints.

REFERENCES

1. **Araya H., Kakuzena M., Kinugawab H., Arai T.** (2004), Level luffing control system for crawler cranes, *Automation in Construction*, 13, 689–697.
2. **Blackburn D., Lawrence J., Danielson J., Singhose W., Kamoi T., Taura A.** (2010), Radial-motion assisted command shapers for nonlinear tower crane rotational slewing, *Control Engineering Practice*, 18, 523–531.
3. **Cha J.H., Roh M.I., Lee K.Y.** (2010), Dynamic response simulation of a heavy cargo suspended by a floating crane based on multibody system dynamics, *Ocean Engineering,* 37 (14-15), 1273–1291.
4. **Geisler T., Sochacki W.** (2011), Modelling and research into the vibrations of truck crane, *Scientific Research of the Institute of Mathematics and Computer Science*, 1 (10), 49-60.
5. **Giergiel J.** (1986), *Damping of mechanical vibrations* (in Polish), Wyd. AGH, Kraków.
6. **Jerman B., Podrzaj P., Kramar J.** (2004), An investigation of slewing-crane dynamics during slewing motion—development and verification of a mathematical model, *International Journal of Mechanical Sciences*, 46, 729–750.
7. **Kilicaslan S., Balkan T., Ider S.K.** (1999), Tipping loads of mobile cranes with flexible booms, *Journal of Sound and Vibration*, 223 (4), 645-657.
8. **Kłosiński J.** (2005), Swing-free stop control of the slewing motion of a mobile crane, *Control Engineering Practice*, 13, 451–460.
9. **Kłosiński J., Trąbka A.** (2010), Frequency analysis of vibratory device model (in Polish), *Pneumatyka*, 1, 46-49.
10. **Maczyński A.** (2000), The influence of crane support flexibility on load motion, *4th EUROMECH Solid Mechanics Conference, Book of abstracts II, General sessions*, Metz, France, June 26-30, 519.
11. **Mijailović R.** (2011), Modelling the dynamic behaviour of the truck-crane, *Transport*, 26 (4), 410–417.
12. **Paszkiewicz T., Osiński M., Wojciech S.** (1999), Dynamic analysis of an offshore crane on offshore installations, *4th International Offshore Cranes Conference*, Stavanger, Norway, April 26-28, 2-38.
13. **Smoczek J.** (2014), Fuzzy crane control with sensorless payload deflection feedback for vibration reduction, *Mechanical Systems and Signal Processing*, 46, 70–81.
14. **Smoczek J., Szpytko J.** (2012), Fuzzy rules-based approach to estimate the availability of transportation system, *International Journal of Intelligent Systems Technologies and Applications*, 11 (1/2), 117-137.
15. **Smoczek J., Szpytko J.** (2014), Evolutionary algorithm-based design of a fuzzy TBF predictive model and TSK fuzzy anti-sway crane control system, *Engineering Applications of Artificial Intelligence*, 28, 190–200.
16. **Sochacki W.** (2007), The dynamic stability of a laboratory model of a truck crane, *Thin-Walled Structures*, 45, 927–930.
17. **Sosna E.** (1984), Influence of flexibility of support system on dynamics of the telescopic mobile crane (in Polish), *Praca doktorska*, Politechnika Łódzka.
18. **Terashima K., Shen Y., Yano K.** (2007), Modeling and optimal control of a rotary crane using the straight transfer transformation method, *Control Engineering Practice*, 15, 1179–1192.
19. **Trąbka A.** (2014), Dynamics of telescopic cranes with flexible structural components, *International Journal of Mechanical Sciences*, 88, 162–174.
20. **Trombski M.** (Editor) (2003), *Control algorithms of telescopic crane operating cycle* (in Polish), Wyd. ATH w Bielsku-Białej.
21. **Uchiyama N.** (2009), Robust control of rotary crane by partial-state feedback with integrator, *Mechatronics*, 19, 1294–1302.
22. **Uchiyama N., Ouyang H., Sano S.** (2013), Simple rotary crane dynamics modeling and open-loop control for residual load sway suppression by only horizontal boom motion, *Mechatronics*, 23, 1223–1236.
23. **Wu J.J.** (2006), Finite element analysis and vibration testing of a three-dimensional crane structure, *Measurement*, 39, 740–749.

DOI 10.2478/ama-2014-0035

EXAMINATION OF THE EFFECT OF PSYCHOPHYSICAL FACTORS ON THE QUALITY OF HUMAN GAIT RECOGNITION

Marcin DERLATKA*

* Department of Automatic Control and Robotics, Faculty of Mechanical Engineering, Bialystok University of Technology, ul. Wiejska 45c, 15-351 Bialystok, Poland

m.derlatka@pb.edu.pl

Abstract: The paper presents an analysis concerning the influence of selected psychophysical parameters on the quality of human gait recognition. The following factors have been taken into account: body height (BH), body weight (BW), the emotional condition of the respondent, the physical condition of the respondent, previous injuries or dysfunctions of the locomotive system. The study was based on data measuring the ground reaction forces (GRF) among 179 participants (3 315 gait cycles). Based on the classification, some kind of confusion matrix were established. On the basis of the data included in the matrix, it was concluded that the wrong classification was most affected by the similar weight of two confused people. It was also noted, that people of the same gender and similar BH were confused most often. On the other hand, previous body injuries and dysfunctions of the motor system were the factors facilitating the recognition of people. The results obtained will allow for the design of more accurate biometric systems in the future.

Key words: Human Gait Recognition, Ground Reaction Forces, Classification

1. INTRODUCTION

Among behavioral biometrics human gait deserves a particular attention. In comparison with other methods of person recognition gait measurement does not require any unnatural interaction of the person with the measuring devices and the person under examination does not have to be aware that is subject to this procedure. Increase in interest in gait as a biometric occurred in 2003, when the DARPA in the USA began its research on the project "Human Identification at a Distance" (Xu et al., 2013).

Currently, within the research on human gait biometrics, we can distinguish three main categories, depending on the signals registered. They are methods based on the data obtained from (Gafurov et al., 2011):

- cameras (Balista J. A. et al., 2010);
- instruments measuring interactions between the foot and the ground (Kumar and Ramakrishnan, 2011; Nakajima et al., 2000; Rodriguez et al., 2009; Yao et al., 2010);
- instruments, markers installed on the examined person (Klempous, 2012).

The most popular methods of human gait recognizing and simultaneously having the broadest spectrum of potential applications are based on measurements obtained from video cameras. In this case the picture registered is usually converted frame by frame into silhouette sequences. Subsequently, depending on the applied methods there occurs an attempt at reading of selected parameters of the human's gait and classification of a person. Advantages of these methods are undoubtedly a possibility of free motion of the person under examination, identification of many people simultaneously and these people's approval of the presence of cameras in buildings (Katiyar et al., 2013). Next group of methods based on the measurement of the interaction of the ground with the lower limbs of the person under examination. Here the examined person must walk along an appropriately-prepared measurement path equipped with force plates (Derlatka, 2012) or special foor with a network of photo interrupter sensors (Yun, 2011). In the case of these methods the main problem is an accurate hit in the measuring device.

In the last method mentioned above the person under examination fully cooperates during the time of measurement. He/she is provided with measurement equipment, such as: accelerators (Gafurov et al., 2011), opto-reflective markers (Lin et al., 2011), or else special insoles in the shoes registering foot pressures on the surface (Porwik et al., 2010).

The process of acquisition of the data describing a human's gait and potential extraction of its features is followed by a classification with such methods as neural networks (Lin and Lin, 2013), Naïve Bayes classifier (Switonski et al., 2011), genetic algorithms (Goldy and Mary, 2012) and others (Moustakidis et al., 2009).

It should be pointed out that very few research, analysing the impact of various parametres on the quality of the biometric system based on human gait, were published. Most often the subject area of acticles represents a choice of: measured signals (Lin and Lin, 2013) or method of features extraction (Pataky et al., 2012). One of the few exceptions, where factors imfluencing the quality of human gait recognition were mentioned, is (Katiyar et al., 2013) According to it problems with recognizing people in the systems based on video cameras are generated by the examined person's change of clothes, a possibility of covering the silhouette of the examined person by objects or other people, changes in lighting as well as the sensitivity of certain parameters sought for to the position angle of the object in relation to the camera

For the methods based on the measurement of the interaction between the foot and the ground practically only at work (Jenkins and Ellis, 2007), the influence of the weight of the participant on the obtained accuracy of the recognition has been tested.

The authors used both normalised to the BW and non-normalised GRF as the input for the biometric system. The results for the non-normalised GRF were significantlly weaker. It is also important to emphasize, however, that previous works were based on an exceptionally low number of people under examination (Gafurov et al., 2011; Lin et al., 2011; Moustakidis et al., 2009; Switonski al., 2011). Very few of scarce exceptions are (Derlatka, 2013; Pataky et al, 2012; Rodriguez et al., 2009), which presented a research based on the group of over 100 people. Unfortunately in those cases, the authors do not usually conduct an in-depth analysis of the results based on the presented material.

The main objective of this paper is to analyse of erroneous classifications in respect of selected psychophysical parameters like body weight, body height, emotions of subjects as well as injuries of organs of movement experienced in the past.

2. METHODOLOGY

2.1. Materials

179 people (66 women and 113 men) took part in the research conducted in the Bialystok University of Technology. It should be stressed out that it is the biggest database containing data describing human gait using GRF. The participants in the research were 21.28 ± 1.04 years old, body weight 75.49 ± 16.64 kilos and body height 174.95 ± 9.29 cm.

Before the research a questionnaire was carried out, where the people under examination provided information on their musculoskeletal dysfunctions and episodes from their past which may affect the gait pattern as well as about their current physico-emotional state.

On the basis of the questionnaires it was concluded that among the system users there were 70 people who did not suffer from any ailments of musculoskeletal system and did not report any incidents from the past. 43 volunteers in this group used to have sprained ankles, including 8 with both ankles. 28 people reported scoliosis, 9 unequal length of lower limbs with at least 0.5 cm of difference, 17 people had broken legs or briken foot's finger in the past, and 8 subjects have flat feet. Moreover, single reports referred to such injuries as: spinal disc herniation, chondromalacia patella, forefoot adduction, kyphosis, lordosis, foot without two fingers (I and II) etc.. In total, the participants reported 24 different types of injuries or dysfunctions of the musculoskeletal system.

Furthermore, in the questionnaire mentioned earlier, the participants determined emotions accompanying them at a given moment and described their physical condition. When determining emotions the participants could choose from the following: serenity, joy, anxiety, uncertainty, nervousness, rush, impatience, excitement, curiosity, irritability. As far as the physical condition is concerned, the participants could select one of the five following options: drowsy, slightly drowsy, well-rested, slightly tired, tired.

2.2. Measurements

This paper, as a basis for recognizing people by gait, adopted three component forces of the ground reaction force: vertial, anterior/posterior and medial/lateral. In the biomechanical sense the ground reaction force (GRF) is a force which affects the person under examination as a result of the ground reaction to pressure. GRF as well as COP are measured by means of the force plates. The detailed description of the force plates can be found in Idźkowski and Walendziuk (2009).

Peaks for the vertical component Fy correspond with the moments of: transferring the weight of the whole body on the limb measured (the first peak force: the peak forces during weight acceptance and the forefoot loading (heel off the ground) just before the toe-off moment; the second peak force: peak forces during terminal stance).

These peaks, for correct feet, reach approximately 120% of the body's weight. This results from the need for maintaining balance while walking. Therefore the value of the reaction forces is higher than the weight force. At the half of the stance period, the whole active surface of the foot touches the ground. This is a period of unloading force during mid-stance (a minimum of the unloading force).

The anterior/posterior component Fx has two phases. In the first one its value is negative. This is a result of decelerate of the registered lower limb: the direction of the force is opposite to the direction of walking. The minimum of the inhibiting phase is usually reached just before the peak force during the weight acceptance occurs for vertical component Fy. Analogically, in the second phase the anterior/posterior component takes positive values. Then there begins the process of acceleration completed with taking the toes off the ground. During the whole period the direction of force Fx is the same as the direction of walking. The peak of the acceleration phase occurs at the initial toe-off phase. This takes place the moment after maximum propulsion for vertical component Fy. The value of component Fx equals zero at the moment of the rear leg is passing the front leg. This corresponds, more or less, with the moment of occurrence of the minimum unloading phase for vertical component Fy. The extreme values of component Fx reach approximately 20% of the body weight of the person under examination.

The direction of the component Fz depends on the examined lower limb. Usually it is assumed that values of Fz are positive for the left lower limb and negative for the right lower limb. A slight exceptions are the moments of initial contact and toe-off, where the foot is at a slight supination. The value of force Fz depends on the style of putting feet on the ground by the person under examination. This force should be greater both in the case of foot pronation as well as in the case of foot abduction. Extremes for Fz are called the same as in the case of vertical component Fy: peak forces during weight acceptance and terminal stance, unloading-force during midstance. The values of these forces make approximately 10% of the examined person's body weight.

During the examinations the person moved at a free speed in his/her own sport shoes on the measurement path, in which 2 Kistler force plates were hidden, working at the frequency of 1 kHz. The volunteers performed several walks (14-20), as a result of which over 3300 strides were registered.

2.3. Dynamic Time Warping

The distance (similarity) between time series has been calculated based on well-known Dynamic Time Warping (DTW) algorithm (generalized the Levenshtein's distance). The result of DTW algorithm is the minimal cost of the so called warping paths, which adjust one time series to another. This investigation take into consideration all three components of two GRFs so the total distance The distance between n and m patterns has been calcu-

DOI 10.2478/ama-2014-0035

lated according to following formula:

$$D(n,m) = \sum_{c=1}^{6} D_c \quad (1)$$

where: D_c – is the DTW distance between the c −th component of GRF for patterns n and m.

2.4. Human gait recognition

The recorded strides have been divided into two sets. 1432 patterns were treated as prototype points (a learning set) and 1883 patterns obtained were treated as a testing set.

The modified version of the k −NN algorithm, presented in Derlatka (2013), has been used for the data classification in this article. The author is aware that there are more advanced algorithms which enable to obtain better classification results. In this case, nonetheless, getting the best human recognition is not as important as the analysis of crucial factors that influence the quality of the recognition. It is only possible when one has a sufficient number of classifier errors which in turn are not random errors but exhibit a steady tendency. According to the author, this criterion is met by the modified k −NN version with a selected $\vartheta = 0.4$ threshold.

The modified k −NN classification algorithm was as follows (Derlatka M., 2013):

1. Determine distance D of the biometric pattern under examination from all prototype patterns in the data base.
2. Select k prototype patterns whose distances D to the pattern under examination are the shortest.
3. By majority vote determine the ID of the user in the data base. If two or more users are equally numerously represented among the patterns selected in point 2 (or the remaining after rejection in point 4) – select the one whose average distance from the selected pattern is the shortest.
4. Reject k' prototypes, for which distance D is longer than $\rho_{\vartheta i}$ for the given threshold ϑ of the user whose ID was selected in point 3.
5. Check in compliance with the procedure in point 3, whether ID for $K = k - k'$ of prototypes remained unchanged. If so, we finish the classification assigning the examined biometric pattern to the ID class. If not, return to point 3.
6. In the case when $k = k'$ $(K = 0)$, we recognize that a given biometric pattern cannot be classified in any of the classes at the assumed threshold ϑ.

2.5. Confusion matrix

Lets $X = \{x_1, x_2, \dots, x_9\}$, where: x_1 – user ID, x_2 – ID predicted by the biometrics system, x_3 – body heigh (BH), x_4 – body weight (BW), x_5 – emotional state, x_6 – physical state, x_7 – user's sex, x_8 – injures in the past {1 – yes; 0 – no}, x_9 – classification {correct, bad}.

The x_8 parameter does not distinguish between different types of past bodily injury or dysfunctions of the motor system which affect the movement pattern. Such a decision was made as the number of kinds of injuries is too big when compared with the number of incorrect classifications. As a consequence, it precludes conducting a reliable analysis.

Of course we have:

$$x_1 = x_2 \Rightarrow x_9 = 'correct' \quad (2)$$

$$x_1 \neq x_2 \Rightarrow x_9 = 'bad' \quad (3)$$

Let's define sets G and B as:

$$G = \{X: x_9 = 'correct'\} \quad (4)$$

$$B = \{X: x_9 = 'bad'\} \quad (5)$$

where: $G \cup B = X$ and $G \cap B = \{\phi\}$

Next we created set $X' = \{x'_1, x'_2, \dots, x'_9\}$ in the following way:

$$MG = \{X': \bigwedge_{\substack{i,j=1,\dots,n \\ i \neq j}} G_i \times G_j\} \quad (6)$$

where: $x'_1 = x_{1i}$, $x'_2 = x_{1j}$, $x'_9 = x_{9i}$, $x'_3 = abs(x_{3i} - x_{3j})$, $x'_4 = abs(x_{4i} - x_{4j})$, x'_5 is equal 0 if $x_{5i} \neq x_{5j}$ and 1 otherwise, x'_6 is equal 0 if $x_{6i} \neq x_{6j}$ and 1 otherwise, x'_7 is equal 0 if $x_{7i} \neq x_{7j}$ and 1 otherwise, x'_8 is equal 0 if $x_{8i} \neq x_{8j}$ and 1 otherwise .

$$MB = \{X': \bigwedge_{i=1,\dots,m} B_i\} \quad (7)$$

where: $x'_1 = x_{1i}$, $x'_2 = x_{1j}$, $x'_9 = x_{9i}$, $x'_3 = abs(x_{3i} - x_{3|x_{2i}})$, $x'_4 = abs(x_{4i} - x_{4|x_{2i}})$, x'_5 is equal 0 if $x_{5i} \neq x_{5|x_{2i}}$, and 1 otherwise, x'_6 is equal 0 if $x_{6i} \neq x_{6|x_{2i}}$and 1 otherwise, x'_7 is equal 0 if $x_{7i} \neq x_{7|x_{2i}}$and 1 otherwise, x'_8 is equal 0 if $x_{8i} \neq x_{8|x_{2i}}$ and 1 otherwise.

As a result we obtained confusion matrix P as:

$$P = MG \cup MB \quad (8)$$

3. RESULTS AND DISCCUSSION

As a result of classifying participants based on the modified kNN algorithm, only 61 strides (3.21%) were assigned to wrong person. This provides evidence showing high discriminatory abilities of human gait as biometrics and presented classification method.

According to (8) the matrix P has been created. It consists of 31868 patterns.

Figure 1 shows the percentage contribution of parametres such as: 'the same sex', 'the same emotions', 'the same physical condition', 'previous injuries', which amount equivalent to 1 for parametres x'_5, x'_6, x'_7 and x'_8 broken down into data correctly and incorrectly classified. The results indicate that in almost 90% cases of errors (precisely 86.89%) people of the same gender were confused. In the case of correct classification, the result obtained is approximately equal to the expected value of 50%. The achieved conclusion is confirmed in e.g. (Yu et al., 2009) where the differences in gait of different genders were indicated.

For parametres describing the identity of emotions, physical condition and past injuries of both the participant and the person representing the model in the training set, only slightly higher value of incorrect classification was noted (25.8% for correct classification and 27.87% for incorrect classification in 'the same emotions', 50.69% and 55.74% respectively in the case of 'the same physical condition' and 51.87% and 59.32% for "past injuries").

Attention should, however, be paid to the fact that the results are processed based on the data collected from questionnaire filled out by the participants and, as a result, should be treated

with some suspicion. Therefore, to be able to describe the influence of a particular parameter on the performance of the biometric system, the difference between two groups being analysed must be noticable enough so as not to cast any reservation. In the situation under analysis, it can be concluded that the biometric system has less problems with correct recognition when only one of the people being compared has had an injury in the past or has a dysfunction of the motor system influencing the movement pattern. This conclusion can be confirmed e.g. in Derlatka and Ihnatouski (2010) where the possobility for a quite accurate automatic recognition of a limited number of motor system dysfunctions was shown.

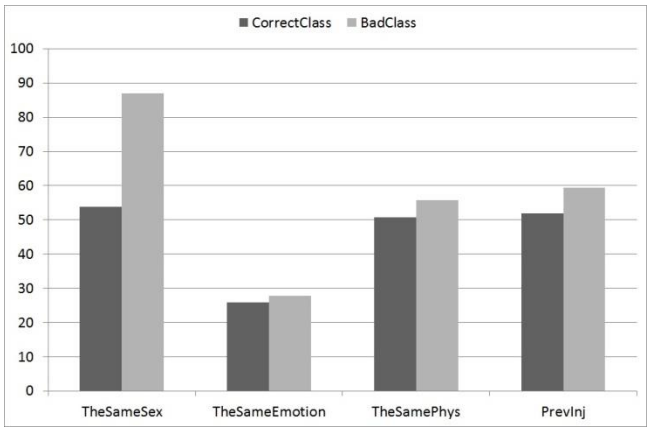

Fig. 1. The precentage contribution of parameters x'_5, x'_6, x'_7, x'_8 in both cases: correct recognition (CorrectClass) and bad recognition (BadClass)

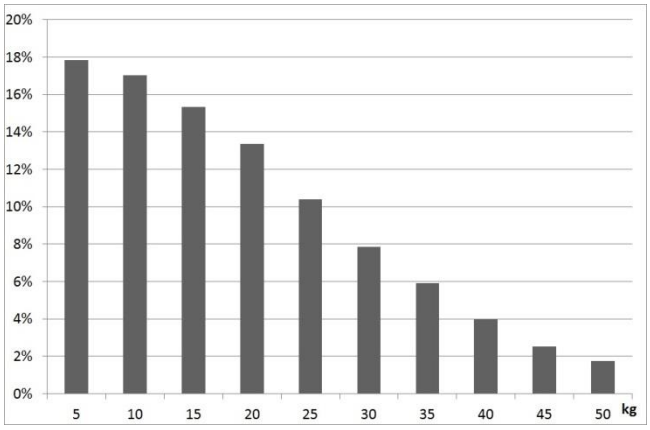

Fig. 2. Normalise histogram of the difference in the BW of relevant subjects in the case of correct recognition

The comparison of normalised histograms of the difference in the BW of relevant people in the case of both correct and incorrect classification clearly indicates that the incorrect classification in only possible when the difference is minor. In the analysed data, the maximum difference in the incorrect classification is 5.3 kg. It it worth pointing out that in the case of correct classification the analysed data take a form similar to the normal distribution. This demonstrates that there is a close relationship between the difference in weight of individuals and the possibility for error occurence. It should be stressed out, that it is in line with the results presented in Jenkins and Ellis (2007) and intuition as the GRF values are proportional to the weight of the participant.

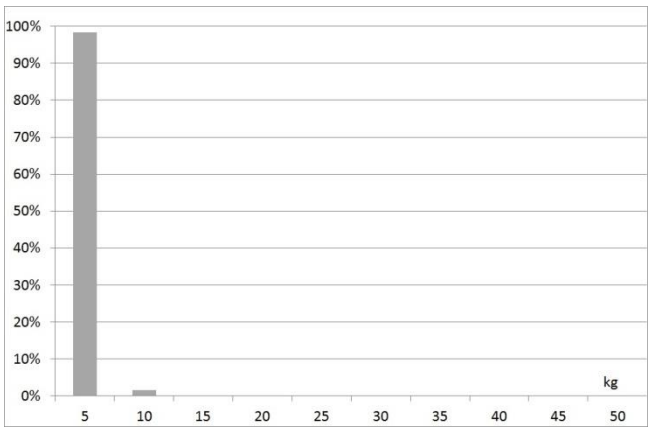

Fig. 3. Normalise histogram of the difference in the BW of relevant subjects in the case of bad recognition

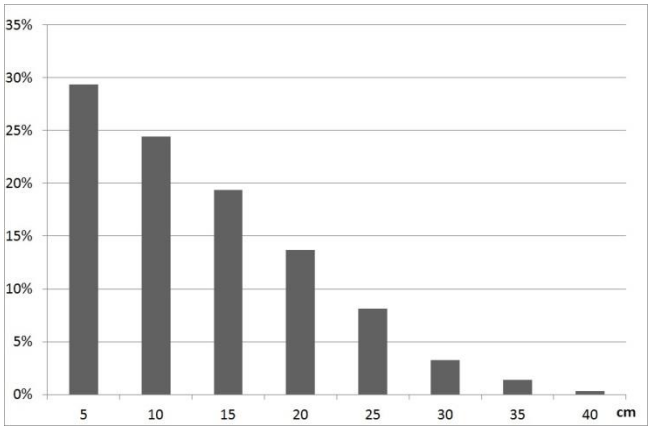

Fig. 4. Normalise histogram of the difference in the BH of relevant subjects in the case of correct recognition

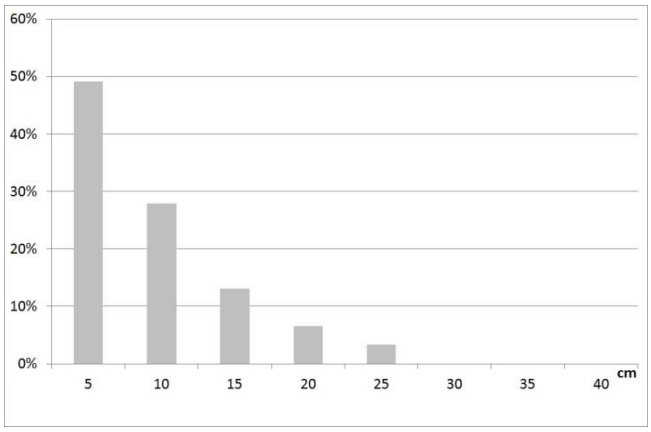

Fig. 5. Normalise histogram of the difference in the BH of relevant subjects in the case of bad recognition

The analysis of the charts shown in the figures 4 and 5 indicates, that the distribution of the data presented differs between the correct and incorrect classifications. This concerns not only the scope of the data (the maximum diffierence in BH in the incorrect classifications is 23.3 cm whereas in the case of correct classification this limit is exceeded in 8% of cases) but also the character of the distribution – the normal disctribution for the correctly classified data and the exponential distribution for errors. In this case the U Mann-Whitney test was also carried out and it confirmed that this value is in a statistically significant way different in both groups.

DOI 10.2478/ama-2014-0035

4. CONCLUSIONS

The study is an analysis of the influence of selected factors on the quality of recognition of the biometric system based on human gait. In order to enable the search for the connections between these parametres and the incorrect recognition, data describing the gait of almost 180 people was collected.

Summarising the results it should be concluded that there is no significant influence of parametres connected with participants' emotions and physical condition on the quality of the classification. It was also concluded that the biometric system has less problems with correct recognition when only one of the people being compared has had an injury in the past or has a dysfunction of the motor system influencing the movement pattern.

The most significant influence was observed in the case of the weight of the participants. During recognition, only people with a difference in weight of less than 5.3 kg were confused. A slightly less important influence was noticed in the case of both gender and body height of the participants. The author is, of course, aware of the fact that people of the same weight are most often of the same sex and of similar height. Irregardless, it is planned to conduct an analysis which will allow for the elimination of the influence of the difference in body weight on both of these factors. It was also noted, that people of the same gender and similar BH were confused most often.

The author is convincied that this knowledge allows for the design of more accurate biometric systems in the future.

REFERENCES

1. **Balista J. A. F., Soriano M. N., Saloma C.A** (2010), Compact time-independent pattern representation of entire human gait cycle for tracking of gait irregularities*, Pattern Recognition Letters*, 31, 20-27.
2. **Derlatka M.** (2012), Human gait recognition based on signals from two force plates, *ICAISC'2012 - LNCS:LNAI*, 7268, 251-258.
3. **Derlatka M.** (2013), Modyfied kNN algorithm for improved recognition accuracy of biometrics system based on gait, *CISIM'2013 – LNCS*, 8104, 59-66.
4. **Derlatka M., Ihnatouski M.** (2010), Decision tree approach to rules extraction for human gait analysis, *ICAISC'2010 – LNCS:LNAI*, 597-604.
5. **Gafurov D., Bours P., Snekkenes E.** (2011) User authentication based on foot motion, *Signal, Image and Video Processing*, 5, 457-467.
6. **Goldy F. R, Mary R. P.** (2012), Genetic Algorithm for self occlusion gait recognition, *International Journal of Advanced Research in Computer and Communictation Engineering*, 1, 10, 865-869.
7. **Idźkowski A., Walendziuk W.** (2009), Evaluation of the static posturograph platform accuracy, *Journal of Vibroengineering,* 11, 3, 511-516.
8. **Jenkins J., Ellis C.** (2007), Using ground reaction forces from gait analysis: body mass as a weak biometrics, *LNCS*, 4480, 251-267.
9. **Katiyar R., Pathak V. K., Arya K. V.** (2013), A study on existing gait biometrics approaches and challenges, *International Journal of Computer Science,* 10(1), 135-144.
10. **Klempous R.** (2012), The different possibilities for gait identification based on motion capture*, EUROCAST, LNCS*, 6928, 187–194.
11. **Kumar A., Ramakrishnan M.** (2011), Legacy of footprints recognition – a review, *International Journal of Computer Applications*, 35(11), 9-16.
12. **Lin Y. C, Lin Y. T**. (2013), Human recognition based on plantar pressure patterns during gait*, J. of Mechanics in Medicine and Biology*, 13(2).
13. **Lin Y. C, Yang B. S, Lin Y. T, Yang Y. T.** (2011) Human recognition based on kinematics and kinetics of gait, *Journal of Medical and Biological Engineering*, , 31(4), 255-263.
14. **Moustakidis S. P, Theocharis J. B**., **Giakas G.** (2009), Feature extraction based on a fuzzy complementary criterion for gait recognition using GRF signals**,** *17th Mediterranean Conference on Control & Automation*, Greece, IEEE, 1456-1461.
15. **Nakajima K., Mizukami Y., Tanaka K., Tamura T.** (2000), Footprint-based personal recognition, *IEEE Transactions on Biomedical Engineering*, 47(11),1534-1537.
16. **Pataky T. C, Mu T., Bosch K., Rosenbaum D., Goulermas J. Y.** (2012), Gait recognition: highly unique dynamic plantar pressure patterns among 104 individuals, *J. R. Soc. Interface*, 9(69), 790-800.
17. **Porwik P., Zygula J., Doroz R, Proksa R.** (2010), Biometric recognition system based on the motion of the human body gravity centre analysis, *Journal of Medical Informatics and Technologies*, 15, 61-69.
18. **Rodriguez V. R., Manson J., Evans N.** (2009), *Assessment of a footstep biometric verification System Handbook of Remote Biometrics*, eds. Tistarelli et al. Advances in Pattern Recognition, London, 313-327.
19. **Switonski A., Polanski A.**, **Wojciechowski K.**. (2011), Human identification based on gait paths, *ACIVS LNCS*, 6915, 531-542.
20. **Wu J., Wang J., Liu L.** (2007), Feature extraction via KPCA for classification of gait patterns, *Human Movement Science*, 26, 393 – 411.
21. **Xu X., Tang J., Zhang X., Liu X., ZXhang H., Qiu Y.** (2013), Exploring techniques for vision based human activity recognition: methods, systems and evaluation, *Sensors,* 13, 1635-1650.
22. **Yao Z. M., Zhou X., Lin E. D, Xu S., Sun Y. N.** (2010), A novel biometric recognition system based on ground reaction force measurements of continuous gait. Human System Interactions, *3rd Conf. on Digital Object Identifie*r, Rzeszow Poland, 452-458.
23. **Yu S., Tan T., Huang K., Jia K., Wu X.**, (2009), A study on gait-based gender classification, *IEEE Transactions on Image Processing,* 18, 8, 1905-1910.
24. **Yun J**. (2011), User Identification using gait patterns on UbiFloorII, *Sensors*, 11, 2611-2639.

.

VISION ANALYSIS SYSTEM FOR AUTONOMOUS LANDING OF MICRO DRONE

Marcin SKOCZYLAS*

*Faculty of Computer Science, Bialystok University of Technology, ul. Wiejska 45A, 15-351 Białystok, Poland

marcin.skoczylas@pb.edu.pl

Abstract: This article describes a concept of an autonomous landing system of UAV (Unmanned Aerial Vehicle). This type of device is equipped with the functionality of FPV observation (First Person View) and radio broadcasting of video or image data. The problem is performance of a system of autonomous drone landing in an area with dimensions of $1\mathrm{m} \times 1\mathrm{m}$, based on CCD camera coupled with an image transmission system connected to a base station. Captured images are scanned and landing marker is detected. For this purpose, image features detectors (such as SIFT, SURF or BRISK) are utilized to create a database of keypoints of the landing marker and in a new image keypoints are found using the same feature detector. In this paper results of a framework that allows detection of defined marker for the purpose of drone landing field positioning will be presented.

Key words: Unmanned Aerial Vehicle, Micro Drone, Image Analysis, CCD Camera, Keypoints Descriptors, SIFT, SURF, BRISK, Object Tracking, Camshift

1. INTRODUCTION

This article describes a concept of an autonomous landing system of UAV (Unmanned Aerial Vehicle). This type of device is equipped with the functionality of FPV observation (First Person View) and radio broadcasting video or image data. Additionally often these flying objects are supplied also with advanced on-board equipment capable of performing autonomous flight. The problem is performance of a system of autonomous drone landing in an area with dimensions of $1\mathrm{m} \times 1\mathrm{m}$. Usage of GPS devices for this purpose is not a good option due to their limited accuracy. Therefore to bring down a flying apparatus in a predetermined point then so-called manual landing procedure has to be used, in this scenario a pilot brings the machine on the ground using radio equipment (radio control device). The proposed autonomous landing system based on CCD camera coupled with an image transmission system connected to a base station and a PC determines the direction of movement of the object during the landing procedure (see Fig. 1). It is worth noting that the developed system supports other on-board equipment such as a GPS receiver, barometric sensor, accelerometer sensors, magnetometer and gyroscope.

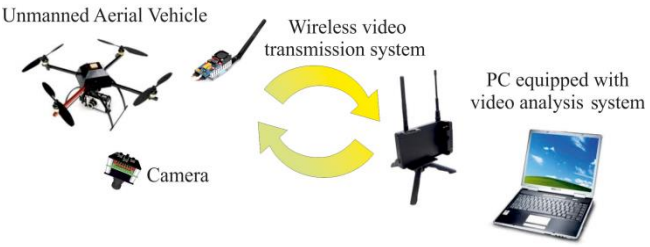

Fig. 1. The general concept of components needed to implement an autonomous landing

2. REQUIREMENTS

In this section main purposes of the presented approach, as well as differences in existing applications will be delineated.

The main purpose of the solution is a possibility of proper detection of landing markers by flying drone in real-time. Markers, representing landing positions, are defined before capturing images on-site and are reused in following runs of the algorithm. The drone captures surroundings using its mobile camera, and as a result of the procedure, the algorithm should give to the drone electronics information about positions of detected landing markers. In overall the algorithm has to be robust with low computational complexity, but also with high accuracy. It's important to note, that the landing markers will be visible in drone's surroundings in different scales and rotations. The solution should handle this situation gracefully, giving to the drone possibility of different capture angles and light intensities, possibly without complicated calibration. Also, captured image can be garbled by radio noise and very often that noise overlaps the landing marker, thus tricking the detection.

To solve the problem above, for the purpose of proper detection of the landing marker even in low quality images, image features detectors are utilized to create a database of keypoints of the landing marker.

Different keypoint extracting algorithms were invented by authors over last many years, these include for example Scale-Invariant Feature Transform (SIFT (Lowe et al., 2004)) or Speeded Up Robust Features (SURF (Bay et al., 2008)), but also recently presented Binary Robust Invariant Scalable Keypoints (BRISK (Leutenegger et al., 2011)) and many others.

3. RELATED WORK

Recognition of defined objects in captured images is a well-known problem and many solutions are existing. Different ap-

proaches to image recognition problems, using texture features classifiers (Skoczylas et al., 2011), image processing filters, etc do exist, and these solutions can perform correct image detection and recognition in captured images as static (Ding et al., 2012), but also moving images (Pan et al., 2013).

Topic of images recognition using keypoints descriptors became recently very popular. For example, SURF algorithm was successfully utilized for face recognition (Li et al., 2013) and road obstacle recognition (Besbes et al., 2010). The BRISK algorithm was implemented into traffic sign recognition as presented in Zheng et al. (2012). These objects are recognized using keypoints detector and descriptors of the points from training images are used to find similar descriptors in captured images. One of such examples is also implementation of SIFT object recognizer in FPGA presented recently (Wang et al., 2013). Authors implemented their algorithm using some of the concepts that are also a base for this publication.

There exist also different approaches to markers recognition as for example recently presented in Yu et al. (2013). Authors are classifying vehicle logos using SVM based on a Bag-of-Words (BoW) approach. The algorithm extracts SIFT features and quantizes features into visual words by 'soft-assignment'. The database is then used for new objects recognition.

Recently, also topic of autonomous detection of markers for Unmanned Aerial Vehicles was researched, for example vision based victim detection system was implemented in Andriluka et al. (2010) where authors successfully used histogram of oriented gradients (HOG) detector for human detection (Dalal et al., 2005). In Shaker et al. (2010) authors presented vision-based autonomous landing system using reinforcement learning.

4. FEATURE DESCRIPTORS

Image feature descriptors are becoming a standard in current state of the art of image recognition algorithms. Their application is mainly for detection and recognition purposes, however there are additional tasks such as medical image registration (Lukashevich et al., 2011).

For this study, author selected most common and popular feature detectors: SIFT, SURF, and BRISK. Main principles of these three algorithms are delineated in the following paragraph.

- Scale-Invariant Feature Transform (SIFT). The SIFT algorithm is quite computational extensive algorithm that detects features in images. Best thing about SIFT is that it is invariant to scale changes, but also rotations and light intensity changes. The original image is incrementally scaled down by a half. This operation generates multiple scale pyramids. Local extrema are identified and key point candidates are detected from which relative orientation is found and removed giving rotation invariance. Orientation histograms over 4x4 regions are extracted and a descriptor vector is created by concatenating all orientation histogram entries. Finally that vector is normalized and a SIFT key point descriptor vector is obtained that contains 128 values.
- Speeded Up Robust Features (SURF). SURF algorithm is also known as an approximate version of SIFT. Main idea of the algorithm is similar, however in SURF authors drew attention to the performance and applied algorithm optimizations. As presented by authors, the algorithm outperforms SIFT in terms of the quality and performance. Scale pyramid is not constructed as in SIFT, instead different filter sizes (octaves) are used to achieve the same purpose (the scale space is analysed by up-scaling the filter size rather than iteratively reducing the image size [Oyallon et al., 2013]). SURF key point descriptor vector contains 64 values.
- Binary Robust Invariant Scalable Keypoints (BRISK). BRISK is a novel algorithm presented recently. As authors state the quality of key point detection is compared to top state-of-the-art key detector SURF, but needs less computation time. This is achieved by detecting key points in octave layers of image scale pyramid, but also in layers in-between in continuous domain via quadratic function fitting. As a result a bit-vector is constructed.

5. DETECTION OF LANDING MARKERS

First, landing marker images database is created. From all images from the landing markers database keypoints are detected using one of features detector described in previous section. Keypoints feature descriptors associated to landing marker image from the database are stored, these are reference vectors of descriptors used for further detection procedure. Thus, for each marker image, a set D_m of vectors representing features descriptors is created. Note, that these vectors have equal sizes in set D_m, but $|D_m|$ can differ, depending on complexity of the image.

In a new image keypoints are found using the same feature detector, these keypoints form a set $K_c = p_1, p_2, \ldots$ and are considered as candidates for keypoints that correspond to the marker image. For all keypoints in the set K_c feature descriptors D_c are calculated, so that each element from set K_c corresponds to one descriptor from set D_c. From the set of candidates K_c, only keypoints that match keypoints existing in the marker image are further processed. For this purpose all keypoints descriptors from training marker D_m are compared with all keypoints descriptors detected in the captured image D_c. A similarity factor, distance (for SIFT and SURF algorithms the similarity factor is distance of vectors, and for BRISK this factor is calculated based on bit operators (Leutenegger et al., 2011)) s of all these descriptors is calculated and keypoints are associated to each other.

Found pairs are filtered to find good matches using technique described in Bradski et al., (2000): first, the minimum distance (min) is found from all matches, and then all distances that are bigger than (this parameter was set empirically; in the literature different parameters for this distance can be found) $2 \cdot min$ are discarded. If calculated distance between two keypoint descriptors is less than a predefined factor, then such keypoint is marked as valid — thus, it is detected and exists in that captured image and is added to the set of found keypoints K_{valid}. Process is repeated for all keypoints from set K_c. If the number of keypoints in set K_{valid} (keypoints in the captured image that correspond to keypoints in marker image, thus with sufficient distance) does not exceed predefined factor $f_v \cdot |D_m|$ thus is not satisfactory, that means that marker object is not visible in the captured image and the algorithm is stopped. In other case, when enough valid keypoints are existing in that captured image, then the algorithm searches for largest cluster of keypoints.

Largest cluster is an area of points that are near to each other. Continuously Adaptive Mean Shift (Camshift) algorithm (Bradski et al., 1998) is applied on the set of detected keypoints K_{valid}

to find largest cluster of keypoints K_{object}. The starting point $p_s = (x_s, y_s)$ for the algorithm is selected from detected keypoints set K_{valid} in such a way that $\forall p = (x, y) \in K_{valid}, \sqrt{(x_s - x)^2 + (y_s - y)^2}$ is minimum. Algorithm iteratively moves point p_s towards center of mass of points inside defined neighbourhood. If the center of mass of points in neighbourhood is equal p_s then algorithm is stopped and cluster K_{object} is found.

And finally, keypoints that reside inside that cluster are considered as keypoints from the marker image. If the number of keypoints inside that found cluster exceeds some predefined factor $f_o \cdot |D_m|$ then that cluster is a detected object marker. The algorithm calculates the center p_o of K_{object} and that center is defined as a landing point for the drone.

All algorithm steps are presented in Fig. 2.

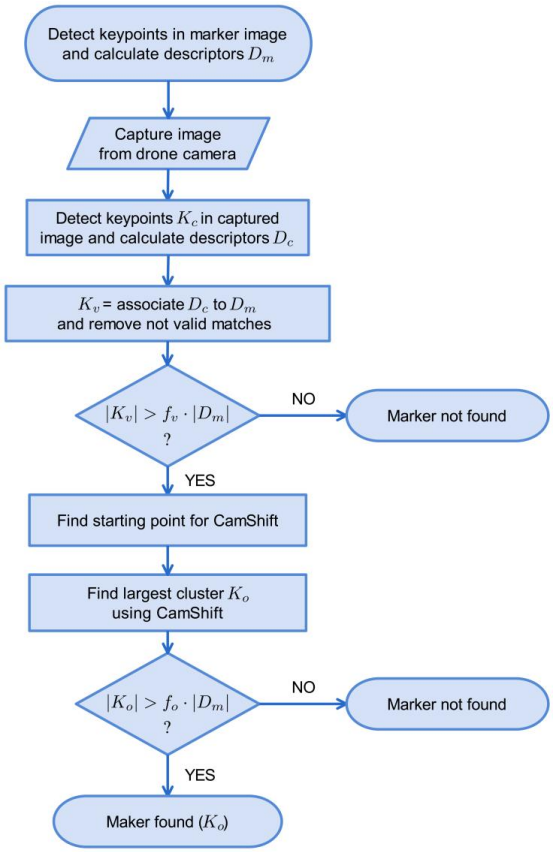

Fig. 2. The Flow chart of marker detection algorithm steps

6. METHODS AND RESULTS

It is very important to select proper keypoint detector algorithm depending on run time and image conditions. Considering, that the whole procedure will be run in an environment with limited resources, the selected algorithm must be robust. Thus, the speed and run time of the algorithm is favored over the accuracy, but from the other hand high accuracy also must be achieved. The keypoint detector is most crucial part for the whole procedure, as it's the most computationally exhaustive part.

To select the keypoint detector algorithm, a database of images was created. Author created a $1\text{m} \times 1\text{m}$ marker and it was put on the ground in the University campus. Image of the marker is shown in Fig. 3.

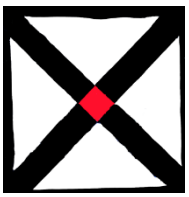

Fig. 3. $1\text{m} \times 1\text{m}$ marker image used for experiments

Micro drone photographed that marker during the flight above the ground. Videos in real-life scenarios from micro drone camera were captured and several video frames were extracted for further processing. These images presented landing marker in different conditions (rotated, scaled and in different lighting conditions). Such database was evaluated using algorithms described in previous sections.

The first test was performed as follows: on the original learning image a keypoint detector algorithm was run, keypoints descriptors were stored in a resulting set D_{learn} together with their positions K_{learn} on the image. That image was further processed and altered by four tests. Each of the tests was performed independently and all the results of individual steps were combined for better readability.

These test runs included:

- scale was changed to a factor of $(0.1, 10.0)$ with a step of 0.1;
- image was rotated and additional black frame was added around the image (rotated by a step of $15°$ from $0°$ to $360°$);
- a gaussian random noise was applied: $I_{test}(x, y) = I_{orig}(x, y) + random$ from 10 to 1000 with a step of 10;
- lightness was altered: $I_{test}(x, y) = I_{orig}(x, y) + lightness$ from -250 to 250 with a step of 5.

After changes to the image were applied, then the whole detection procedure was performed:

1. On a new image keypoints K were detected.
2. Keypoints pairs were matched and largest cluster was found.
3. Number $|K_{fit}|$ of valid keypoints from the marker image inside that largest cluster in captured image was calculated.
4. To calculate the $ratio$, a number of keypoints $|K_{fit}|$ is divided by a number of all keypoints $|K|$ from the marker image, and multiplied by 100 for readability.
5. $time$ to perform calculations was recorded.

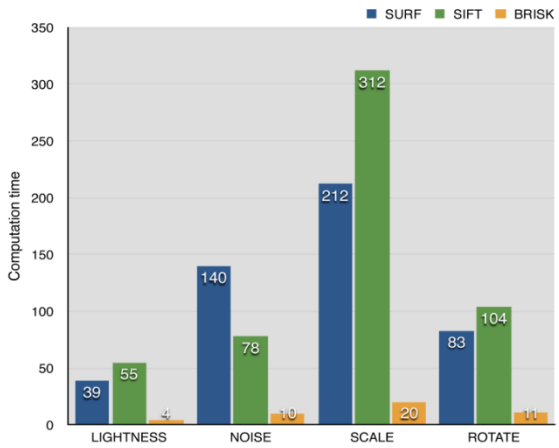

Fig. 4. Comparison of keypoint descriptors computation time in *ms* for lightness, noise, scale and rotate changes

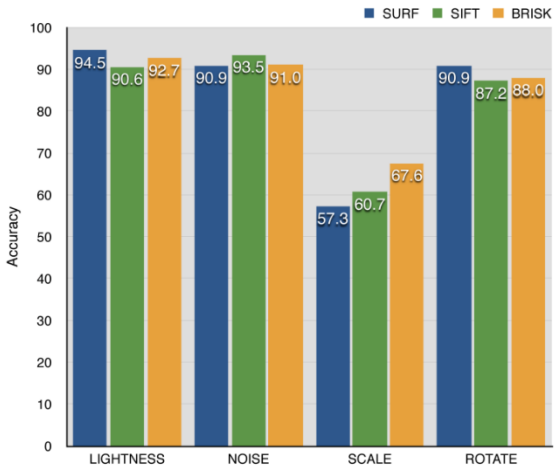

Fig. 5. Comparison of keypoint descriptors accuracy for lightness, noise, scale and rotate changes

On each image from original learning data set a test procedure was run, result $ratios$ and $times$ needed to perform the test were recorded. From all these tests overall results were created by combining all results into two charts: time and accuracy of each algorithm for lightness, noise, scale and rotate changes. Algorithm was run on 2.6 GHz Intel Core i7 machine. Results of the above computations are shown in Fig. 4 and 5.

During the second approach experimental setup was tested in real-life conditions (see Fig. 6).

Fig. 6. Experimental setup overview

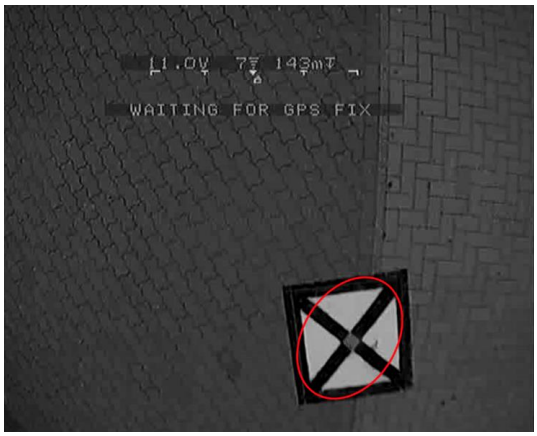

Fig. 7. Example marker detection results in real-life captured image

Fig. 8. Example marker detection result in real-life captured image. Captured image contains radio noise that overlaps the marker

Images were transmitted to a base station and captured. Detection result of the marker in real-life captured image examples are shown in Fig. 7 and Fig. 8.

7. DISCUSSION

Complexity of the whole recognition procedure mainly depends on the number of detected keypoints candidates K_c in the captured image. Also, number of keypoints from original image marker K_m is crucial, as descriptors of both keypoints sets are compared to each other. If the image is complex, the more keypoints are detected and large numbers of keypoints cause a reduction of recognition speed, due to the fact that all these points have to be compared with all keypoints from the marker image.

Recognition accuracy depends on the selected keypoints algorithm, but it is important to note that the algorithm presented in this paper has two factor values that have to be defined empirically. These factors f_v and f_o determine interval when not enough points (or correct points) are found, thus denoting that the marker image is missing in the image (in such case algorithm is stopped). Wrong values of these factors can cause a situation that when marker image is not existing in the image it is in fact incorrectly detected. From the other hand when image has a huge noise, then appropriate settings can guide the algorithm to properly detect even not-readable image, as it is shown in Fig. 9.

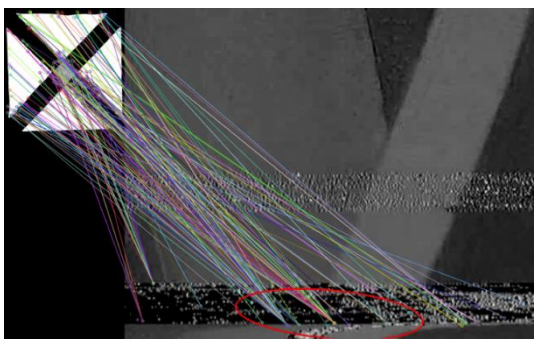

Fig. 9. Example marker detection result in real-life captured image with radio noise, lines show marker keypoints (left-up part of the figure) corresponding to keypoints detected in the captured image (right part of the figure)

Let's analyze result from Fig. 9 that shows correctly detected landing marker when f_o and f_v values were set to low. Due to noise disturbances keypoints are garbled with respect to marker image axes, but the number of detected keypoints is enough to correctly find that cluster. However, that could lead to a situation that when marker is not existing in the captured image it is incorrectly detected as in Fig. 10. Keeping these factors high can cause a situation that marker keypoints is not detected at all and thus false negative results, but too low values cause wrong false positives. Further study is needed to correctly define impact of these factors on recognition procedure accuracy and computation times in real-life scenarios.

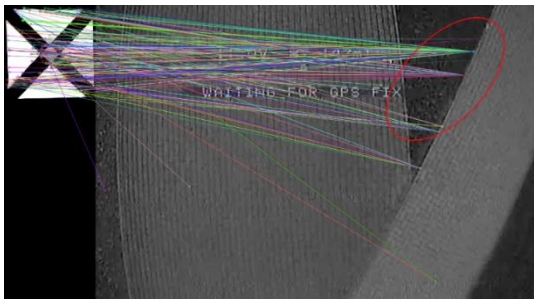

Fig. 10. Example non-existing marker detection result in real-life captured image with incorrectly set f_o and f_v parameters

It is important to note, that from all keypoint detectors, the BRISK algorithm gives the best accuracy for different scales, keeping very good accuracy for rotations. Considering that drone will mostly have to deal with scaled and rotated landing marker image but not noise and lightness changes, this seems as a good feature of this algorithm.

In addition, BRISK outperforms SURF and SIFT in terms of performance considerably, thus BRISK with no doubt is the best choice for further analysis and implementation in embedded environment.

8. CONCLUSIONS

The problem of proper detection of landing marker in user surroundings of the drone can be solved by the algorithm from previous sections. Shapes, representing landing marker, are detected using SURF or BRISK algorithm with very good rate, their low computation time allows the user to run it in limited environment, even in real-time. Proper and fast keypoints matching solves different angles and light intensities, without any calibration, also with existing radio noise. However, it is still necessary to perform further study on the performance of these algorithms in real-life scenarios.

REFERENCES

1. **Andriluka M., Schnitzspan P., Meyer J., Kohlbrecher S., Petersen K., Stryk O., Roth S., Schiele B.** (2010), Vision based victim detection from unmanned aerial vehicles, *IEEE/RSJ International Conference on Intelligent Robots and Systems (IROS)*.
2. **Bay H., Ess A., Tuytelaars T., Van Gool L.** (2008), Speeded-Up Robust Features (SURF), *Comput. Vis. Image Underst.*, Vol. 110(3), 346–359.
3. **Besbes B., Apatean A., Rogozan A., Bensrhair A.** (2010), Combining SURF-based local and global features for road obstacle recognition in far infrared images. *2010 13th International IEEE Conference on Intelligent Transportation Systems (ITSC)*, 1869 – 1874.
4. **Bradski G.** (2000), The OpenCV Library, *Dr. Dobb's Journal of Software Tools*.
5. **Bradski R.** (1998), Computer vision face tracking for use in a perceptual user interface, *Proceedings of the Fourth IEEE Workshop on Applications of Computer Vision*, 214-219.
6. **Dalal N., Triggs B.** (2005), Histograms of oriented gradients for human detection, *Computer Vision and Pattern Recognition, 2005. CVPR 2005, IEEE Computer Society Conference* , Vol. 1, 886–893.
7. **Ding D., Yoon J., Lee C.** (2012), Traffic sign detection and identification using SURF algorithm and GPGPU, *SoC Design Conference (ISOCC),* 506–508.
8. **Leutenegger S., Chli M., Siegwart R.** (2011), BRISK: Binary Robust invariant scalable keypoints, *Computer Vision, IEEE International Conference,* 2548–2555.
9. **Li H., Xu T., Li J., Zhang L.** (2013), Face recognition based on improved SURF, *Third International Conference on Intelligent System Design and Engineering Applications (ISDEA)*, 755 – 758.
10. **Lowe D.** (2004), Distinctive Image Features from Scale-Invariant Keypoints, *Int. J. Comput. Vision*, Vol. 60(2), 91–110.
11. **Lukashevich P., Zalesky B., Ablameyko S.** (2011), Medical image registration based on surf detector, *Pattern Recognit. Image Anal.*, Vol. 21(3), 519–521.
12. **Oyallon E., Rabin J.** (2013), An analysis and implementation of the SURF method, and its comparison to SIFT, *Image Processing On Line*, 1-31.
13. **Pan J., Chen W., Peng W.** (2013), A new moving objects detection method based on improved SURF algorithm, *25th Chinese Control and Decision Conference (CCDC)*, 901–906.
14. **Shaker M., Smith M. N. R., Shigang Y., Duckett T.** (2010), Vision-based landing of a simulated unmanned aerial vehicle with fast reinforcement learning, *International Conference on Emerging Security Technologies (EST),* 183–188.
15. **Skoczylas M., Rakowski W., Cherubini R., Gerardi S.** (2011), Unstained viable cell recognition in phase-contrast microscopy, *Opto-Electronics Review*, Vol. 19(3), 307–319.
16. **Wang Z., Xiao H., He W., Wen F., Yuan K.** (2013), Real-time SIFT-based object recognition system, *IEEE International Conference on Mechatronics and Automation (ICMA)*, 1361 – 1366.
17. **Yu S., Zheng S., Yang H., Liang L.** (2013), Vehicle logo recognition based on bag-of-words, *10th IEEE International Conference on Advanced Video and Signal Based Surveillance (AVSS)*, 353 – 358.
18. **Zheng Z., Zhang H., Wang B., Gao Z.** (2012), Robust traffic sign recognition and tracking for advanced driver assistance systems, *International IEEE Conference on Intelligent Transportation Systems (ITSC)*, 704 – 709.

The work has been accomplished under the funding S/WI/1/2013 financed by Faculty of Computer Science, Bialystok University of Technology.

DOI 10.2478/ama-2014-0037

FRICTIONAL HEATING DURING SLIDING OF TWO SEMI-SPACES WITH ARBITRARY THERMAL NONLINEARITY

Ewa OCH

Faculty of Mechanical Engineering, Bialystok University of Technology, 45C Wiejska Street, Bialystok, 15-351, Poland

e.och@doktoranci.pb.edu.pl

Abstract: Analytical and numerical solution for transient thermal problems of friction were presented for semi limited bodies made from thermosensitive materials in which coefficient of thermal conductivity and specific heat arbitrarily depend on the temperature (materials with arbitrary non-linearity). With the constant power of friction assumption and imperfect thermal contact linearization of nonlinear problems formulated initial-boundary thermal conductivity, using Kirchhoff transformation is partial. In order to complete linearization, method of successive approximations was used. On the basis of obtained solutions a numerical analysis of two friction systems in which one element is constant (cermet FMC-845) and another is variable (grey iron ChNMKh or aluminum-based composite alloy AL MMC) was conducted.

Key words: Frictional Heating, Arbitrary Thermal Non-Linearity, Thermosensitive Materials

1. INTRODUCTION

Developing analytical or analytical – numerical solutions of heat conduction problems with regard to the frictional heating is necessary in designing new types of friction nodes (eg. the choice of friction material, estimation of the temperature level, selection of the process operational parameters, etc.). In such modeling method the real friction pairs are replaced by systems such as: strip - half-space, strip - strip or semi-space - semi-space.

Friction heat problem solution for a homogeneous semi-space sliding at constant speed on the surface of the second semi-space, with constant thermophysical materials properties and perfect thermal contact condition fulfillment are presented in Grylitsky (1996) monograph, and solution taking into account imperfect thermal contact – in work: Sazonov (2008).

Frictional heating during two semi-space, strip and semi-space, slipping with a constant delay and the two strips system with regard to various kinds of conditions of thermal contact was examined in works: Nosko et al. (2009), Yevtushenko et al. (2013, 2014), Barber (1976). Details on methods for solving one-dimensional thermal problems of friction with constant thermophysical materials properties are given in monograph Kuciej (2012).

The analysis of literature sources concerning analytical or analytical-numerical modeling of heat generation processes due to frictional forces, shows that models considering constant thermophysical properties of friction materials are very well developed. Whereas, solutions involving a non-linearity of frictional materials pairs have been so far developed in an insufficient number of cases.

Homogeneous semi-space surface frictional heating with linear dependence of thermal conductivity coefficients and specific heat of the temperature at a constant ratio of the thermal diffusivity (material with a simple non-linearity) was examined in the work: Abdel-Aal, (1997), Abdel-Aal et al. (1997), Abdel-Aal and Smith (1998, 1998b). Methods of solving one-dimensional initial-boundary problems of thermal conductivity for the two semi-spaces sliding against one another at a constant linear velocity or semi-space made of materials with a simple non-linearity, are proposed in the work: Och (2013), Evtushenko et al. (2014), Yevtushenko et al. (2014, 2014b), whereas solutions involving arbitrary non-linearity (thermophysical properties of materials change under the influence of temperature in any way) in the work: Yevtushenko et al. (2014c, d).

Surveys of analytical and numerical methods for solving initial-boundary problems of heat conduction for materials with temperature-dependent thermal properties are presented in the work: Kushnir and Popovych (2011), Yevtushenko and Kuciej (2012).

The present work is a continuation of studies presented in article Och (2013), where case of simple thermal nonlinearity of materials was considered. Whereas in this work friction elements materials are characterized by arbitrary non-linearity.

2. STATEMENT OF THE PROBLEM

Let the two semi-limited thermally sensitive bodies with the same initial temperature T_0 be compressed at infinite and constant pressure p_0 in the parallel direction to the z axis of the Cartesian coordinate system $Oxyz$ (Fig. 1). At initial point of time $t = 0$ bodies start to slip with a constant speed V_0 in the positive direction of y-axis. Due to the friction forces, on the contact surface $z = 0$ heat is generated, which penetrates into the contacting bodies - heating them.

It was assumed, that the sum of heat fluxes intensities directed perpendicularly from the contact surfaces to the inside of each contacting body, is equal to the specific power of friction forces $q_0 = fV_0p_0$ (Yevtushenko and Kuciej, 2012). Whereas the heat transfer through the surface of the friction takes place with constant coefficient of contact thermal conductivity h (Podstrigach, 1963; Barber, 1970).

Further in these article, all values referring to the upper and lower semi-spaces will respectively have subscripts 1 and 2.

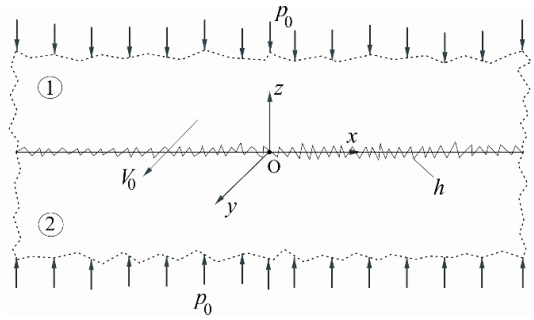

Fig. 1. The scheme of frictional heating

Both, coefficient of thermal conductivity K_l and specific heat c_l, $l = 1, 2$ of the two semi-spaces materials depend on temperature T:

$$K_l(T) = K_{l,0}\, K_l^*(T),\ K_{l,0} \equiv K_l(T_0)$$
$$c_l(T) = c_{l,0}\, c_l^*(T), c_{l,0} \equiv c_l(T_0) \quad (1)$$

$K_l^*(T), c_l^*(T)$ – dimensionless functions. Densities ρ_l, $l = 1, 2$ of considered bodies materials are constant.

Taking into account mentioned above assumptions, the distribution of transient temperature field $T(z,t)$ in semi-spaces is found from the following heat conduction problem boundary-value solution:

$$\frac{\partial^2 T_1^*}{\partial \zeta^2} = \frac{1}{k_0^* k_1^*(T_1^*)} \frac{\partial T_1^*}{\partial \tau},\ \zeta > 0,\ \tau > 0 \quad (2)$$

$$\frac{\partial^2 T_2^*}{\partial \zeta^2} = \frac{1}{k_2^*(T_2^*)} \frac{\partial T_2^*}{\partial \tau},\ \zeta < 0,\ \tau > 0 \quad (3)$$

$$K_2^*(T_2^*) \frac{\partial T_2^*}{\partial \zeta}\Big|_{\zeta=0^-} - K_0^*\ K_1^*(T_1^*) \frac{\partial T_1^*}{\partial \zeta}\Big|_{\zeta=0^+} = 1,\ \tau > 0 \quad (4)$$

$$K_2^*(T_2^*) \frac{\partial T_2^*}{\partial \zeta}\Big|_{\zeta=0^-} + K_0^*\ K_1^*(T_1^*) \frac{\partial T_1^*}{\partial \zeta}\Big|_{\zeta=0^+} = Bi\ [T_1^*(0^+, \tau) - T_2^*(0^-, \tau)],\ \tau > 0 \quad (5)$$

$$T_l^*(\zeta, \tau) \to T_0^*,\ |\zeta| \to \infty,\ l = 1,2 \quad (6)$$

$$T_l(\zeta, 0) = T_0^*,\ |\zeta| < \infty,\ l = 1,2 \quad (7)$$

where:

$$\zeta = \frac{z}{a},\ \tau = \frac{k_2 t}{a^2},\ K_0^* = \frac{K_{1,0}}{K_{2,0}},\ k_0^* = K_0^* \frac{\rho_2 c_{2,0}}{\rho_1 c_{1,0}},\ Bi = \frac{h\, a}{K_{2,0}} \quad (8)$$

$$T_a = \frac{q_0 a}{K_{2,0}},\ T_l^* = \frac{T_l}{T_a},\ T_0^* = \frac{T_0}{T_a}, l = 1,2 \quad (9)$$

$$k_l^*(T_l^*) = \frac{K_l^*(T_l^*)}{c_l^*(T_l^*)}, l = 1,2 \quad (10)$$

a – is a characteristic linear dimension. Further, as the value of this parameter, we take the effective depth of heat penetration, i.e. the distance from the contact surface, on which the temperature is equal to 5% of the maximal temperature on the surface of friction (Chichinadze et al., 1979).

3. LINEARIZATION OF THE PROBLEM

In order to linearize the non-linear boundary-value heat conduction problem of friction (2) – (7) we introduce the Kirchhoff's function (Kirchhoff, 1894):

$$\Theta_l(\zeta, \tau) = \int_{T_0^*}^{T^*} K_l^*(T_l^*)\, dT_l^*,\ l = 1,2 \quad (11)$$

As a result, we obtained a sequence of linear boundary-value problems in relation to the functions $\Theta_l^{(i)}(\zeta, \tau)$, $i = 0,1,\ldots$, that are successive approximations of the sought Kirchhoff's function (Yevtushenko et al., 2014c, d):

$$\frac{\partial^2 \Theta_1^{(i)}}{\partial \zeta^2} = \frac{1}{k_0^*\, k_1^{*(i)}} \frac{\partial \Theta_1^{(i)}}{\partial \tau},\ \zeta > 0,\ \tau > 0 \quad (12)$$

$$\frac{\partial^2 \Theta_2^{(i)}}{\partial \zeta^2} = \frac{1}{k_2^{*(i)}} \frac{\partial \Theta_2^{(i)}}{\partial \tau},\ \zeta < 0,\ \tau > 0 \quad (13)$$

$$\frac{\partial \Theta_2^{(i)}}{\partial \zeta}\Big|_{\zeta=0} - K_0^* \frac{\partial \Theta_1^{(i)}}{\partial \zeta}\Big|_{\zeta=0} = 1, \tau > 0 \quad (14)$$

$$\frac{\partial \Theta_2^{(i)}}{\partial \zeta}\Big|_{\zeta=0} + K_0^* \frac{\partial \Theta_1^{(i)}}{\partial \zeta}\Big|_{\zeta=0} = Bi^{(i)}\ [\Theta_1^{(i)}(0, \tau) - \Theta_2^{(i)}(0, \tau)], \tau > 0 \quad (15)$$

$$\Theta_l^{(i)}(\zeta, \tau) \to 0,\ |\zeta| \to \infty,\ \tau \geq 0,\ l = 1,2 \quad (16)$$

$$\Theta_l^{(i)}(\zeta, 0) = 0,\ |\zeta| < \infty,\ l = 1,2 \quad (17)$$

gdzie:

$$k_l^{*(0)} = 1, k_l^{*(i)} = k_l^*\left\{T^*\left[\Theta_l^{(i-1)}(\zeta^*, \tau^*)\right]\right\},\ i = 1,2,\ldots;\ l = 1,2 \quad (18)$$

$$Bi^{(0)} = Bi,$$
$$Bi^{(i)} = Bi \frac{\{T^*[\Theta_1^{(i-1)}(0,\tau^*)] - T^*[\Theta_2^{(i-1)}(0,\tau^*)]\}}{[\Theta_1^{(i-1)}(0,\tau^*) - \Theta_2^{(i-1)}(0,\tau^*)]},\ i = 1,2,\ldots, \quad (19)$$

(ζ^*, τ^*) – these are established values of dimensionless coordinate and time (8), for which we perform iteration.

4. KIRCHHOFF FUNCTION

By applying the Laplace integral transform (Sneddon, 1972):

$$\overline{\Theta}_l^{(i)}(\zeta, p) \equiv L\ [\Theta_l^{(i)}(\zeta, \tau); p] = \int_0^\infty \Theta_l^{(i)}(\zeta, \tau)\, e^{-p\tau} d\tau \quad (20)$$

to the linear boundary-value problem (11)–(19), we obtain the following boundary problem for two ordinary differential equations of the second order:

$$\frac{d^2 \overline{\Theta}_1^{(i)}(\zeta, p)}{d\zeta^2} - \frac{p}{k_0^* k_1^{*(i)}} \overline{\Theta}_1^{(i)}(\zeta, p) = 0,\ \zeta > 0 \quad (21)$$

$$\frac{d^2 \overline{\Theta}_2^{(i)}(\zeta, p)}{d\zeta^2} - \frac{p}{k_2^{*(i)}} \overline{\Theta}_2^{(i)}(\zeta, p) = 0,\ \zeta < 0 \quad (22)$$

$$\frac{d\overline{\Theta}_2^{(i)}}{d\zeta}\Big|_{\zeta=0} - K_0^* \frac{d\overline{\Theta}_1^{(i)}}{d\zeta}\Big|_{\zeta=0} = \frac{1}{p} \quad (23)$$

$$\frac{d\overline{\Theta}_2^{(i)}}{d\zeta}\Big|_{\zeta=0} + K_0^* \frac{d\overline{\Theta}_1^{(i)}}{d\zeta}\Big|_{\zeta=0} = Bi^{(i)}[\overline{\Theta}_1^{(i)}(0, p) - \overline{\Theta}_2^{(i)}(0, p)] \quad (24)$$

$$\overline{\Theta}_l^{(i)}(\zeta, p) \to 0,\ |\zeta| \to \infty,\ l = 1,2 \quad (25)$$

Solution to the problem (21)-(25) takes form:

$$\overline{\Theta}_1^{(i)}(\zeta, p) = \frac{\sqrt{k^{*(i)}} e^{-\zeta_1^{(i)}\sqrt{p}}}{2\varepsilon p(\sqrt{p} + \beta^{(i)})} \left(1 + Bi^{(i)} \sqrt{\frac{k_2^{*(i)}}{p}}\right),\ \zeta \geq 0,$$
$$\overline{\Theta}_2^{(i)}(\zeta, p) = \frac{e^{-\zeta_2^{(i)}\sqrt{p}}}{2\varepsilon p(\sqrt{p} + \beta^{(i)})} \left(\varepsilon + Bi^{(i)} \sqrt{\frac{k_1^{*(i)}}{p}}\right),\ \zeta \leq 0, \quad (26)$$

$$\zeta_1^{(i)} = \frac{\zeta}{\sqrt{k_0^* k_1^{*(i)}}}, \zeta_2^{(i)} = \frac{|\zeta|}{\sqrt{k_2^{*(i)}}}, \quad (27)$$

$$\beta^{(i)} = 0.5\varepsilon^{-1} Bi^{(i)} m^{(i)}, \quad m^{(i)} = \sqrt{k^{*(i)}} + \varepsilon, \quad (28)$$

$$k^{*(i)} = \frac{k_1^{*(i)}}{k_2^{*(i)}}, \varepsilon = \frac{K_0^*}{\sqrt{k_0^*}}. \quad (29)$$

Applying the inversion formulae (Bateman and Erdelyi, 1954):

$$L^{-1}\left[\frac{\beta\, e^{-\alpha\sqrt{p}}}{p\sqrt{p}(\sqrt{p}+\beta)}; \tau\right] = \Phi(\alpha,\tau) - \beta^{-1}\Psi(\alpha,\beta,\tau) \quad (30)$$

$$L^{-1}\left[\frac{\beta\, e^{-\alpha\sqrt{p}}}{p(\sqrt{p}+\beta)}; \tau\right] = \Psi(\alpha,\beta,\tau), \alpha,\beta \geq 0 \quad (31)$$

$$\Phi(\alpha,\tau) = 2\sqrt{\tau}\,\mathrm{ierfc}\left(\frac{\alpha}{2\sqrt{\tau}}\right), \tau \geq 0 \quad (32)$$

$$\Psi(\alpha,\beta,\tau) = \mathrm{erfc}\left(\frac{\alpha}{2\sqrt{\tau}}\right) - e^{\alpha\beta+\beta^2\tau}\mathrm{erfc}\left(\frac{\alpha}{2\sqrt{\tau}} + \beta\sqrt{\tau}\right) \quad (33)$$

to the solutions (26)-(29), we obtain:

$$\Theta_1^{(i)}(\zeta,\tau) = \frac{1}{m^{(i)}}\left[\Phi\left(\zeta_1^{(i)},\tau\right) + \gamma_1^{(i)}\Psi\left(\zeta_1^{(i)},\beta^{(i)},\tau\right)\right], \quad \zeta \geq 0, \tau \geq 0 \quad (34)$$

$$\Theta_2^{(i)}(\zeta,\tau) = \frac{\sqrt{k^{*(i)}}}{m^{(i)}}\left[\Phi\left(\zeta_2^{(i)},\tau\right) + \gamma_2^{(i)}\Psi\left(\zeta_2^{(i)},\beta^{(i)},\tau\right)\right] \quad \zeta \leq 0,\ \tau \geq 0 \quad (35)$$

$$\gamma_1^{(i)} = \frac{(\sqrt{k^{*(i)}}-\varepsilon)}{\sqrt{k_2^{*(i)}}(\sqrt{k^{*(i)}}+\varepsilon)\, Bi^{(i)}}, \gamma_2^{(i)} = \frac{\varepsilon(\varepsilon-\sqrt{k^{*(i)}})}{\sqrt{k_1^{*(i)}}(\sqrt{k^{*(i)}}+\varepsilon)\, Bi^{(i)}} \quad (36)$$

In particular case $\zeta = 0$ from solutions (34)–(36) we obtain:

$$\Theta_1^{(i)}(0,\tau) = \frac{1}{m^{(i)}}\left[\varphi(\tau) + \gamma_1^{(i)}\psi(\beta^{(i)},\tau)\right], \tau \geq 0\,, \quad (37)$$

$$\Theta_2^{(i)}(0,\tau) = \frac{\sqrt{k^{*(i)}}}{m^{(i)}}\left[\varphi(\tau) + \gamma_1^{(i)}\psi(\beta^{(i)},\tau)\right], \quad (38)$$

$$\varphi(\tau) = 2\sqrt{\frac{\tau}{\pi}}, \quad (39)$$

$$\psi(\beta^{(i)},\tau) = 1 - e^{\beta^{(i)^2}\tau}\mathrm{erfc}(\beta^{(i)}\sqrt{\tau}). \quad (40)$$

5. ITERATIVE SCHEME

To find the relation between temperature and Kirchhoff's function the form of functions $K_l^*(T_l^*)$ and $c_l^*(T_l^*)$ should be specified (1). We assume that these are polynomials:

$$K_l^*(T_l^*) = \sum_{n=0}^{N_l} a_{l,n}(T_l^*)^n, c_l^*(T^*) = \sum_{n=0}^{M_l} b_{l,n}(T_l^*)^n \quad (41)$$

where $a_{l,n}$ and $b_{l,n}$ - are known coefficients for materials of each considered friction pairs. We use both equations (41) to find the function $k_l^*(T_l^*)$ (10). In addition, substituting the function $K_l^*(T_l^*)$ (41) into equation (10), after integration we obtain the relation between temperature and Kirchhoff's function:

$$\Theta_l(\zeta^*,\tau^*) = \sum_{n=0}^{n} a'_{l,n}\{[T^*(\zeta^*,\tau^*)]^{n+1} - (T_0^*)^{n+1}\} \quad (42)$$

where $a'_{l,n} = a_{l,n}/(1+n)$, $l = 1,2$. Using the method of least squares we located dependency inverse to (42):

$$T_l^*(\zeta^*,\tau^*) = \sum_{n=0}^{N_l} c_{l,n}[\Theta_l(\zeta^*,\tau^*)]^n, l = 1,2 \quad (43)$$

where$c_{l,n}$ - are known coefficients.

For the zero approximation ($i = 0,\ k_l^{(0)} = 1,\ Bi^{(0)} = Bi$) solutions (34) – (40) are coincident with boundary-value problems solutions with constant thermo-physical properties of materials (Sazonov, 2008). The relation between temperature and Kirchhoff's function at this iterative step is linear:

$$T_l^{*(0)}(\zeta^*,\tau^*) = \Theta_l^{(0)}(\zeta^*,\tau^*) + T_0^*,\ l = 1,2. \quad (44)$$

For successive approximations ($i \geq 1$) we begin with calculating the values of $k_l^{*(i)}$, $l = 1,2$, (17) and $Bi^{(i)}$ (18) and finding the function $\Theta_l^{(i)}(\zeta^*,\tau^*)$ (34) - (36) or $\Theta_l^{(i)}(0,\tau^*)$ (37) – (40), $l = 1,2$. Then from the formula (43), we obtain an approximation of the dimensionless temperature $T_l^{*(i)}(\zeta^*,\tau^*)$ or $T_l^{*(i)}(0,\tau^*)$, $l = 1,2$. The convergence of an iterative process in (ζ^*,τ^*) is monitored by checking the inequality (Euclidean norm):

$$\sqrt{\left(\frac{T_1^{*(i)}-T_2^{*(i-1)}}{T_1^{*(i)}}\right)^2 + \left(\frac{T_2^{*(i)}-T_2^{*(i-1)}}{T_2^{*(i)}}\right)^2} \leq 10^{-6}. \quad (45)$$

6. NUMERICAL ANALYSIS AND CONCLUSIONS

The calculations have been made for the following friction pairs: gray iron ChNMKh - cermet FMC-845 and composite on aluminum alloy base AL MMC - FMC-845. These materials are used to produce friction elements of braking systems (Chichinadze et al., 1986; Kim el al., 2008). The values of the thermophysical properties of selected materials at temperature $T_0 = 20$ °C are given in Tab. 1. Graphs of functions $K_l^*(T^*)$ and $c_l^*(T^*)$ (41), for the consideraded friction materials are shown in Fig. 2, and the corresponding values of the coefficients $a_{l,n}$, $b_{l,n}$ and $c_{l,n}$, $n = 0,1,2,3$ are given in Tab. 2. We can notice that the coefficient of thermal conductivity of gray iron ChNMKh and cermet's FMC-845 decreases with increasing temperature, and AL MMC increases in the range $0 \leq T^* \leq 0.5$, and then for $0.5 < T^* \leq 1.3$ decreases, and next for $T^* > 1.3$ rise again. Specific heat of all considered materials increases with increase of temperature. Calculations were performed for the following input parameters: $q_0 = 1\mathrm{MW/m}$, $a = 5$ mm, $T_a = 204$ °C and $Bi = 5$.

Tab. 1. The thermo-physical coefficients values of the materials at the$T_0 = 20$ °C

Materials	K_0 W/(m · C)	c_0 J/(kg · C)	ρ kg/m³
FMC-845 (Chichinadze et al., 1986)	24.5	392.2	6000
ChNMKh (Chichinadze et al., 1986)	51	500.1	7100
AL MMC (Kim el al., 2008)	155.75	874	2730

Evolutions of the dimensionless temperature on the contact surface of two selected friction pairs ChNMKh–FMC-845 and AL MMC–FMC-845 are presented in Fig. 3. The calculations have been made with taking into account friction materials thermal properties changes influenced by temperature (solid lines) and at the constant thermal properties of these materials (dashed lines).

Tab. 2. The approximation coefficients values

	n	0	1	2	3
FMC-845	a_n	1	0.001799	-0.019018	0.001953
	b_n	1	0.000547	0.048323	0.001003
	c_n	0.098041	0.99977	0.001746	0.005215
ChNMKh	a_n	1	-0.112		
	b_n	1	0.325214	0.065993	-0.027336
	c_n	0.098543	1.012837	0.05264	0.011315
AL MMC	a_n	1	0.356782	-0.421682	0.141147
	b_n	1	0.209544	-0.147707	0.062199
	c_n	0.097949	0.926329	0.002449	-0.00639

The temperature increases monotonically during the whole process of frictional heating, which is characteristic for the heating process at the constant power of friction forces (Grylitsky, 1996). The effect of thermal sensitivity with temperature increase is most noticeable for the cermets in the case of frictional pair ChNMKh-FMC-845 (Fig. 3a). However for gray iron ChNMKh temperature difference after certain time from beginning of the frictional heating process ($\tau \approx 0.5$), reaches predetermined value. Taking into account FMC-845 thermal sensibility results in temperature increase, and decrease in ChNMKh, compared to the temperature values found at constant thermophysical properties of materials. This is caused by cermet FMC-845 coefficient of thermal conductivity (1%) and specific heat (2.5%) decrease at $0 \leq \tau \leq 2$. Corresponding values for ChNMKh gray iron are 7% decrease of K^* and 21% increase of c^*. It is a significant increase of c^* in the gray iron semi-space (despite the K^* decrease) which caused a slight decrease in temperature.

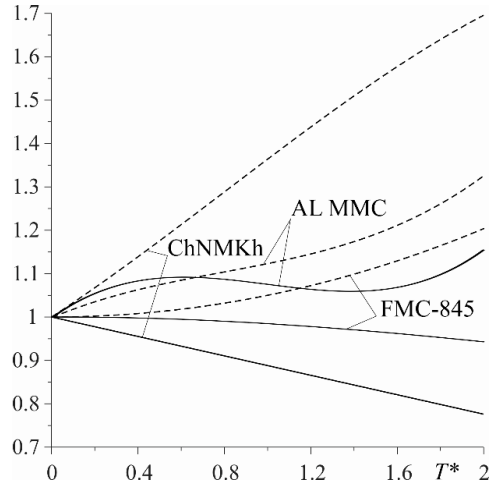

Fig. 2. Dependence of thermal conductivity K^* (solid lines) and specific heat c^* coefficient (dashed lines) on the dimensionless temperature T^* for the considered materials: ChNMKh, AL MMC, FMC-845.

In the case of the second friction couple AL MMC - FMC-845 (Fig. 3b), the difference between the temperature calculated with taking into consideration nonlinearity of materials and at constant thermo-physical properties is also increasing, but much more slower than in the case of the first friction pair. Consideration of materials thermal sensitivity causes a decrease in temperature on surfaces of both semi-spaces. For an AL MMC aluminum alloy 10% increase in coefficient of thermal conductivity K^* and 6% increase in specific heat c^* at $0 \leq \tau \leq 2$ causes, that the temperature difference calculated with and without taking into consideration the thermal sensitivity is significantly greater than cermet FMC-845.

In both considered cases, the temperature on semi-spaces surface made from cermet FMC-845 is always higher than the temperature on gray iron ChNMKh semi-spaces surface or aluminum alloy base composite AL MMC. This is due to significantly worst inferior thermal conductivity of FMC-845 when compared to ChNMKh and AL MMC (Tab. 1 and 2).

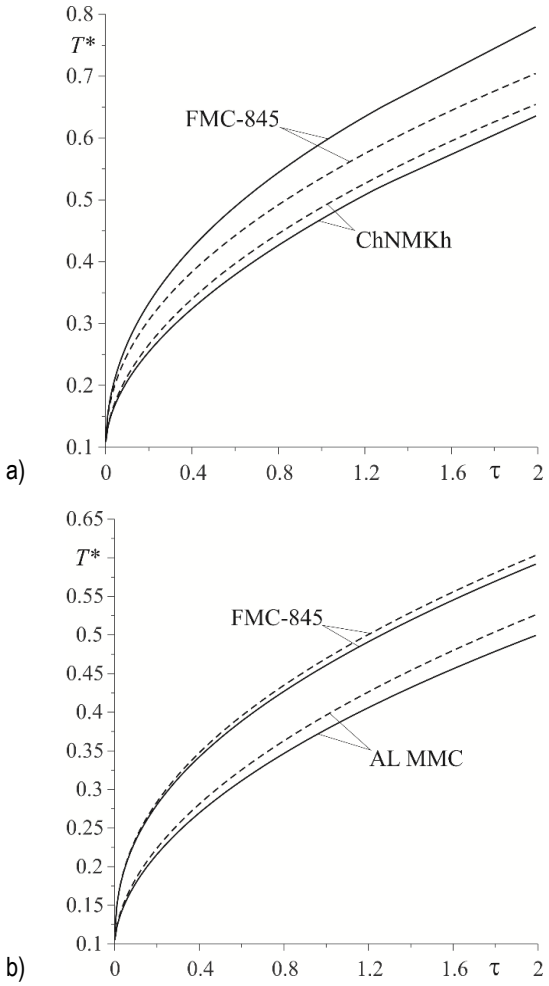

Fig. 3. Evolution of the dimensionless temperature on the contact surface for two friction pairs at $Bi = 5$: a) ChNMKh – FMC-845, b) AL MMC – FMC-845 (solid lines – calculations with considered materials thermal sensitivity; dashed lines – without materials thermal sensitivity consideration

Nomenclature: a – characteristic dimension; Bi – Biot number; c – specific heat; c_0 – specific heat at an initial temperature; $\mathrm{ierfc}(x) = \pi^{-1/2}e^{-x^2} - x\,\mathrm{erfc}(x)$, $\mathrm{erfc}(x) = 1 - \mathrm{erf}(x)$, $\mathrm{erf}(x)$ – Gauss error function; f – friction coefficient; h – coefficient of thermal conductivity of contact; K – coefficient of thermal conductivity; K_0 – coefficient of thermal conductivity at an initial temperature; k – coefficient of thermal diffusivity; p_0 – pressure; q_0 – specific power of friction; T – temperature; T_0 – initial temperature; T^* – dimensionless temperature; t – time; V_0 – sliding speed; z – spatial coordinate; Θ – Kirchhoff's variable; ρ – specific density; τ – Fourier number; ζ – dimensionless spatial coordinate.

REFERENCES

1. **Abdel-Aal H. A.** (1997), On the distribution of friction-induced heat in the dry sliding of metallic solid pairs, *Int. Comm. Heat Mass Trans.*, Vol. 24, 989–998.
2. **Abdel-Aal H. A., Smith S. T.** (1998a), Thermal compatibility of metallic pairs in sliding contact, *Int. Comm. Heat Mass Trans.*, Vol. 25, 599–608.
3. **Abdel-Aal H. A., Smith S. T.** (1998b), On friction-induced temperatures of rubbing metallic pairs with temperature-dependent thermal properties, *Wear*, Vol. 216, 41–59.
4. **Abdel-Aal H. A., Smith S.T., Patten J. A.** (1997), On the development of surface temperatures in precision single-point diamond abrasion of semiconductors, *Int. Comm. Heat Mass Trans.*, Vol. 24, 1131–1140.
5. **Barber J.R.** (1970), The conduction of heat from sliding solids, *Int. J. Heat. Mass Tran.*, Vol. 13, 857–869.
6. **Barber J. R.** (1976), Some thermoelastic contact problems involving frictional heating, *Quarterly Journal of Mechanics and Applied Mathematics*, Vol. 29, 1-13.
7. **Bateman H., Erdelyi A.** (1954), *Tables of integral transforms*, V. 1, McGraw-Hill, New York.
8. **Chichinadze A. V., Matveevski R. M., Braun E. P.** (1986), *Materials in tribotechnics non-stationary processes*, Nauka, Moscow (in Russian).
9. **Chichinadze A. V., Braun E. D., Ginsburg A. G., Ignat'eva Z. V.** (1979), *Calculation, Test and Selection of Frictional Couples*, Nauka, Moscow (in Russian).
10. **Evtushenko O, Kuciej M., Och E.** (2014), Influence of the thermal sensivity of materials on the temperature at friction, *Mat. Sci.*, Vol. 50, 117–122.
11. **Grylitsky D. V.** (1996), *Thermoelastic contact problems in tribology*, A Textbook, Institute of the Contents and Methods of Education, Ministry of Education of the Ukraine, Kiev.
12. **Kim S. W., Park K., Lee S. H., Kang K. H., Lim K. T.** (2008), Thermophysical properties of automotive metallic brake disk materials, *Int. J. Thermophys.*, Vol. 29, 2179–2188.
13. **Kirchhoff G. R.** (1894), *Heat theory lectures* B.G. Teubner, Leipzig (in Germany).
14. **Kuciej M.** (2012), *Analytical models of transient frictional heating*, Oficyna Wydawnicza Politechniki Białostockiej, Białystok (in Polish).
15. **Kushnir R. M., Popovych V. S.** (2011), Heat conduction problems of thermosensitive solids under complex heat exchange, Heat conduction – Basic Research, V. Vikhrenko Ed., *In Tech*, Croatia, 131–154.
16. **Nosko A. L., Belyakov N. S., Nosko A. P.** (2009), Application of the generalized boundary condition to solving thermal friction problems, *J. Frict. Wear*, Vol. 30, 615–625.
17. **Och E.** (2013), Frictional Heating During Sliding of Two Semi-Spaces with Simple Thermal Nonlinearities, *Acta Mech. Autom.*, Vol. 7, 236–240.
18. **Podstrigach Ya. S.** (1963), The temperature field in a system of rigid bodies coupled by thin interface*, Inzh.-Fiz. Zh.*, Vol. 6, No 10, 129–136, (in Russian).
19. **Sazonov V. S.** (2008), Nonideal contact problem of nonstationary heat conduction for two half-spaces, *J. Eng. Phys. Thermophys.,* Vol. 81, 397–408.
20. **Sneddon I. N.** (1972), *The use of integral transforms*, McGraw-Hill, New York.
21. **Yevtushenko A., Kuciej M., Och E.** (2014a), Effect of Thermal Sensitivity of Materials of Tribojoint on Friction Temperature, *J. Frict. Wear*, Vol. 35, 77–83.
22. **Yevtushenko A., Kuciej M., Och E.** (2014b), Influence of thermal sensitivity of the pad and disk materials on the temperature during braking, *Int. Comm. Heat Mass Transf.*, Vol. 55, 84–92.
23. **Yevtushenko A., Kuciej M., Och E.** (2014c), Temperature in thermally nonlinear pad-disk brake system, *Int. Comm. Heat Mass Transf.*, Vol. 57, 274–281.
24. **Yevtushenko A., Kuciej M., Och E.** (2014d), Some methods for calculating the temperature during friction of the thermosensitive materials, *Num. Heat Transf.*, Vol. 67, 696–718.
25. **Yevtushenko A. A., Kuciej M.** (2012), One-dimensional thermal problem of friction during braking: The history of development and actual state, *Int. J. Heat Mass Tran.*, Vol. 55, 4118–4153.
26. **Yevtushenko A. A., Kuciej M., Yevtushenko O.** (2013), The boundary conditions on the sliding surface in one-dimensional transient heat problem of friction, *Int. J. Heat Mass Trans.*, Vol. 59, No 1, 1-8.
27. **Yevtushenko A. A., Kuciej M., Yevtushenko O.** (2014), The asymptotic solutions of heat problem of friction for a three-element tribosystem with generalized boundary conditions on the surface of sliding, I*nt. J. Heat Mass Trans.*, Vol. 70, 128–136.
28. **Yune Y. G., Bryant M. D.** (1988), Transient nonlinear thermal runaway effects in carbon graphite electrical brushers, *IEEE Trans. on Components, Hybrids, and Manufacturing Technology*, Vol. 11, 91–100.
29. **Yune Y. G., Bryant M. D.** (1989), Thermal evolution of hot spots in thermally nonlinear carbon graphite sliders, *Trans. ASME. J. Tribology*, Vol. 111, 591–596.

The present paper is financially supported by the National Science Centre of Poland (project No 2011/01/B/ST8/07446).

NON-UNIFORMITY OF THE COMBUSTOR EXIT FLOW TEMPERATURE IN FRONT OF THE GAS TURBINE

Józef BŁACHNIO*, Wojciech I. PAWLAK*

*Bialystok University of Technology, Faculty of Mechanical Engineering, ul. Wiejska 45C, 15-351, Białystok, Poland
*Air Force Institute of Technology, ul. Księcia Bolesława 6, 01-494 Warszawa, Poland

j.blachnio@pb.edu.pl, wojciech.pawlak@itwl.pl

Abstract: Various types of damages to gas-turbine components, in particular to turbine blades, may occur in the course of gas turbine operation. The paper has been intended to discuss different forms of damages to the blades due to non-uniformity of the exit flow temperature. It has been shown that the overheating of blade material and thermal fatigue are the most common reasons for these damages. The paper presents results from numerical experiments with use of the computer model of the aero jet engine designed for simulations. The model has been purposefully modified to take account of the assumed non-homogeneity of the temperature field within the working agent at the turbine intake. It turned out that such non-homogeneity substantially affects dynamic and static properties of the engine considered as an object of control since it leads to a lag of the acceleration time and to increase in fuel consumption. The summarized simulation results demonstrate that the foregoing properties of a jet engine are subject to considerable deterioration in pace with gradual increase of the assumed non-homogeneity of the temperature field. The simulations made it possible to find out that variations of the temperature field non-homogeneity within the working agent at the turbine intake lead to huge fluctuation of the turbine rpm for the idle run.

Key words: Gas Turbine, Blade, Simulation Model, Working Agent Temperature Field, Health/Maintenance Status

1. INTRODUCTION

A turbine is a component included in the thermal turbomachinery category. It converts enthalpy of the working medium, also called the working fluid (exhaust stream, gaseous decomposition products or compressed gas), into the mechanical work, which results in the rotation of the rotor. The advantages of gas turbines such as the ability to develop high power in a compact and low-weight structure, relatively high energy conversion efficiency of the process, simple structure, ease of use under different climatic conditions (particularly, at low ambient temperatures), and a fairly high reliability have made it were widely used in, e.g. power engineering, traction, marine and aircraft engines, and aerospace technology. Unfortunately, gas turbines have also their drawbacks, the most essential being high operating temperature of some of their parts such as blades, and large rotor speeds.

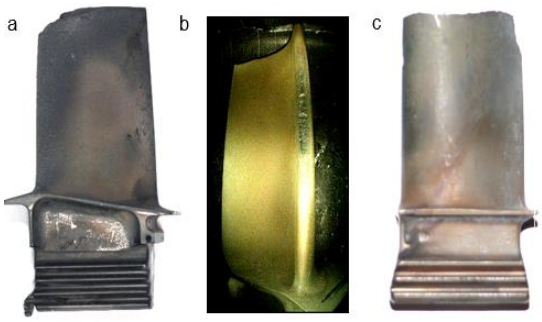

Fig. 1. Instances of thermal damages to gas turbine blades: a) – the region of material overheating at the end of the leading edge, b) – overheating region and a fracture on the leading edge, c) – the blade broken off due to material overheating (Spychała et al., 2008)

Different types of damages to gas turbine components keep occurring throughout the whole process of their exploitation (Błachnio and Pawlak, 2011; Błachnio et al., 2014; Bogdan and Błachnio, 2010). Parts of the turbine that are most vulnerable to damages are blades, the condition of which is crucial to the reliability and service life of the entire turbine and a system it is built (Marsh, 2013). The main reasons why gas turbine blades get damaged are the overheating and thermal fatigue (Fig. 1).

The reaction of blade material to mechanical loads depends mainly on its operating temperature. To select material to produce a blade of some specific strength one should take account of mechanical properties and stresses in the region of the maximum blade temperature (Błachnio and Pawlak, 2011). A typical temperature distribution along the blade is severely non-uniform (Fig. 2).

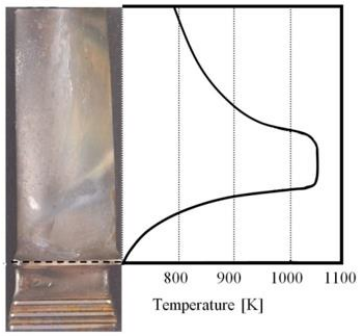

Fig. 2. Typical temperature distribution along the gas turbine blade (Bogdan and Błachnio, 2010)

The blade overheating results from the permissible average values of the exit-flow temperature being exceeded. Another reason is a non-uniform temperature distribution along the turbine

blade-rim circumference (Fig. 3). The non-uniform temperature distribution behind the turbine results, in turn, from fuel being incorrectly sprayed by fuel injectors in the combustion chamber. Most often, the problem is effected by carbon deposits from fuel of poor quality/properties (Żółtowski and Cempel, 2004; Spychała et al., 2008).

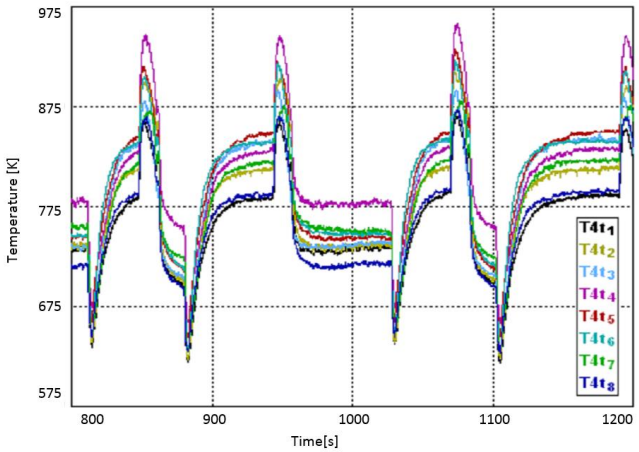

Fig. 3. Instantaneous circumferential non-uniform temperature T_4 distribution measured with eight thermocouples ($T4t_1 - T4t_8$) located behind the turbine; measurements taken at increasing/ decreasing rotational speeds (Błachnio and Pawlak, 2011)

A damage to at least one blade among dozens around the blade rim may result in a gas-turbine failure, or even destruction. Therefore, the question of uniform temperature distribution along the blade, and in particular, along the circumference of the gas-turbine blade rim proves extremely significant as referred to gas turbine power and reliability (Swadźba et al., 2008).

2. SPECIFIC PROPERTIES OF A TURBINE ENGINE AS A NON-LINEAR OBJECT

All versions of the simulation model for the jet engine that have already been published by (Pawlak et al., 2003; Pawlak, 2010) comprise considerable number of non-linear parameters. In particular, these include static characteristics of the compressor and the turbine. The theory of control says that in case when at least one component in the computation structure is non-linear, the entire structure is non-linear as well (Pismenny and Levy, 2002). Thus, a turbine jet engine, considered as an object of control, is a dynamic nonlinear object. Such an important feature of a turbine engine, resulting from that fact that the engine is a non-linear dynamic object, is the impact of the temperature field non-homogeneity within the working agent at the outlet of the combustion chamber onto the acceleration time and performance at steady conditions.

Procedures of handover /takeover tests of engines at manufacturing plants as well as routine tests after overhauls include measurements of the temperature field (Dzida, 2000). In most cases, due to practical reasons, the temperature field non-homogeneity is measured within a cross-section of the jet nozzle duct with use of dedicated equipment. The reasons for non-homogeneity may be various and in practice the phenomenon is very difficult for total eradication (Dzida, 2000). The most common method that can be applied consists in appropriate calibration and selection of a matching set of working injectors. Fig. 4 shows an example graph that depicts non-homogeneity of temperature field across the jet nozzle of a prototype K-16 engine (slightly altered version of the K-15 engine). The image was acquired by means of the measuring testbench shown in Fig. 5. The testbench is made up of two sets of thermocouples, with 7 units in each set, deployed between the inner and outer walls of the jet duct within its cross-section. The measurements are taken by simultaneous readouts from all 14 thermocouples at a time for various angle positions of the entire arrangement selected by its revolution around the longitudinal axis.

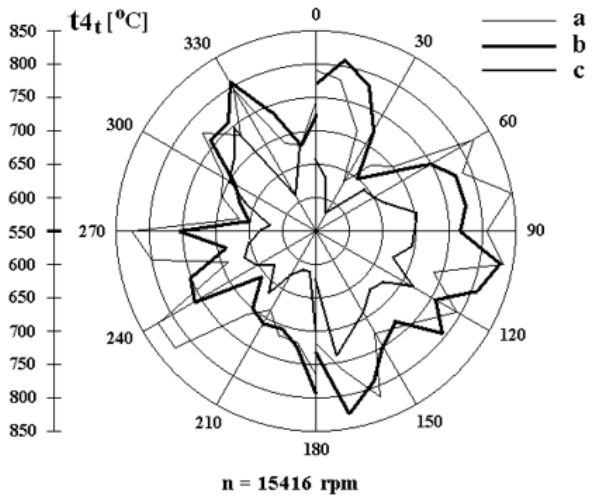

Fig. 4. Example results for measurements of the temperature field non-homogeneity within the working agent inside the jet nozzle of the K-16 engine. a – nearby the outer wall, b – in the middle of the gas duct radius, c – nearby the inner wall

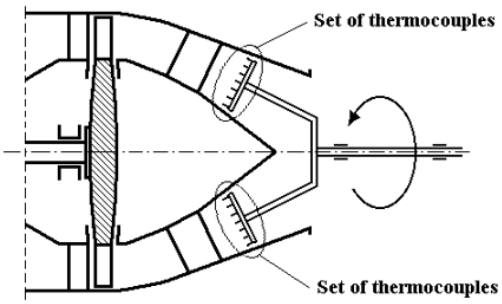

Fig. 5. Diagram of an appliance for measurement of the temperature field non-homogeneity within the working agent in the engine jet nozzle

The measurement results depicted in Fig. 4 indicate that non-homogeneity of the temperature field for the cross-section of the working agent flux is surprisingly large and subject to some fluctuations in spite of the constant rpm of the rotor. The size of such fluctuations can be expressed as discrepancies of temperatures measured for the same measurement points but after elapsing of time necessary for displacements of the measurement arrangement by the angle of 180º (see temperature differentials for 'azimuths" of 0º and 180º).

The simulation model for the SO-3 engine (Pawlak et al., 2003; Pawlak, 2010) presented involves description of the working agent parameters within selected cross-sections of the gas duct with use of the 'zero-dimensional' approach. Thus, such a description is incapable of considering such nuances as 3D nature of the working agent flow, in particular through the so called 'hot part' of the engine.

3. PLAN FOR A NUMERICAL EXPERIMENT WITH USE OF A SIMULATION MODEL

The idea of this paper consists in suggestion to modify the structure of the engine model with the aim to achieve a kind of a simple mathematical dummy that enables simulation of the temperature field non-homogeneity within the working agent at the combustion chamber outlet, where the simulation is carried out with use of basically zero-dimensional description of the working agent flow.

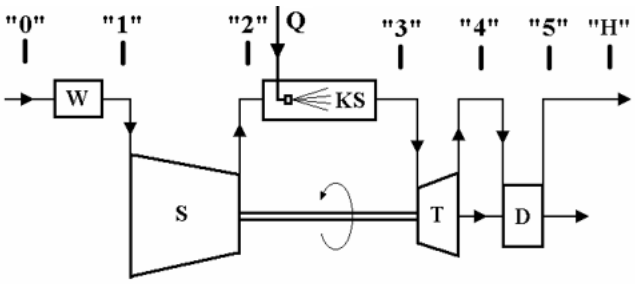

Fig. 6. The basic principal diagram of a turbojet engine: W – engine intake, S – compressor, KS combustion chamber, T – turbine, D – exhaust nozzle jet, Q – fuel expenditure

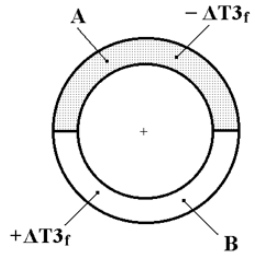

Fig. 7. Conventional breakdown of the cross-section area for the outlet duct of the combustion chamber (or the intake duct of the turbine)

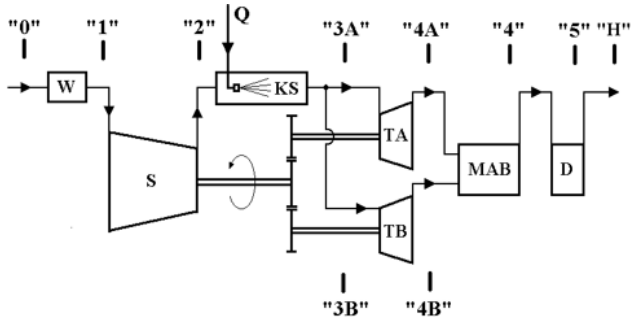

Fig. 8. The schematic diagram for the engine model – a mathematical dummy for simulation of the temperature field non-homogeneity within the working agent at the turbine intake: W – engine intake, S – compressor, KS combustion chamber, TA – turbine (part 'A'), TB – turbine (part 'B'), MAB mixing area, D – nozzle jet, Q – fuel expenditure

Fig. 6 depicts the general structure of the engine. This diagram was used as the outset point to develop the simulation model already described in (Pawlak et al., 1996; Pawlak and Balicki, 2003). Figs. 7 and 8 depict upgraded version of that model where both the turbine and the combustion chamber are split into mutually equal parts. Each of the TA and TB turbines has the same efficiency characteristic curve, whilst the flow characteristic curves are equivalent to a half of the working agent flux (Driankov et al., 1966; Stewart, 2001).

With regard to the split combustion chamber the assumption was made that a different temperature of the working agent should be measured at the outlet of each turbine half, which is the result of random and difficult to explain fluctuations of the temperature field. The conventional diagram split in that way into two mutually equal cross-section areas of the outlet duct of the combustion chamber is shown in Fig. 7.

4. RESULTS FROM THE NUMERICAL EXPERIMENT CARRIED OUT WITH USE OF THE SIMULATION MODEL

The upgraded model for the SO-3 engine as described above was then combined with the model for the automatic control circuit, not shown in the drawing (Pismenny and Levy, 2002). The control circuit enables execution of simulated control for transition processes and generation of selected steady states. Two types of numerical experiments were carried out. The first type assumed investigation into how the non-homogeneity of the temperature field affects transition processes within the engine. The second series of investigations was dedicated to check impact of the temperature field non-homogeneity onto static characteristics of the engine (Wróbel, 2004).

The transition processes were triggered by quick subsequent accelerations and decelerations, starting for the idle run of the engine up to nearly the maximum thrust with due care to avoid tripping the limiter for the maximum engine rpm. The experiments were carried out with the presumed values of the $\Delta T3_f$ parameter that represents the measure of non-homogeneity of the temperature field distribution at the outlet of the combustion chamber (or at the turbine intake). Examples of obtained results are depicted in Fig. 9 to Fig. 11.

The selected static characteristic curves of the engine are shown in Fig. 9 to Fig. 11. These curves were plotted for the engine operation under normal atmospheric conditions on the ground (Ma = 0, H = 0) and for flights at the speed of Ma = 0.4 under normal atmospheric conditions at the altitude of 6 km. For that purpose the own-developed method proposed by the author was applied, referred to as scanning of the engine status space and described in details in Pawlak (2010). That method, verified in Pawlak and Balicki (2003) and Błachnio and Pawlak (2011) for determination of static characteristic curves for the K-15 engine, prevails over the conventional one, typically used for the same purpose because it enables collection of great many points with measurement results, which is shown in Fig. 9 to Fig. 11.

4.1. Simulation of selected transition processes

Results from simulation of transition processes for the case in which the engine runs under normal ground conditions are shown in Fig. 9 to Fig. 11. Excitation of the transition processes was carried out by input waveforms of fuel expenditures for three 3 values of the $\Delta T3_f$ parameter as shown in Fig. 9.

The presented results feature with some distinctive properties:

– Values of all engine parameters presented in graphs plotted for steady states clearly depend on the value of the $\Delta T3_f$ parameter in spite of the fact that the fuel expenditure observed for steady states and shown in Fig. 9 is exactly the same for all values of the $\Delta T3_f$f parameter,

– Duration of the acceleration and deceleration periods are substantially different for all monitored engine parameters (n, Thrust, C_j) and depend on the value of the $\Delta T3_f$ parameter.

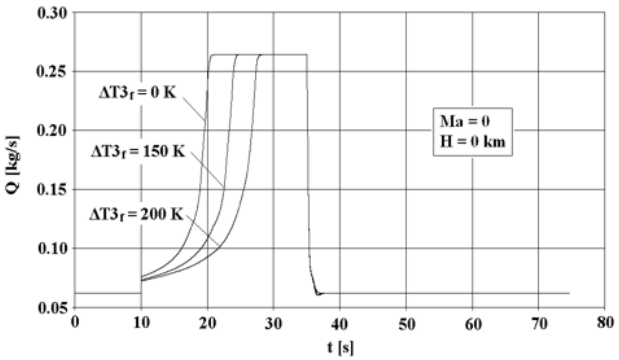

Fig. 9. Timings for fuel expenditures during acceleration and deceleration of the jet engine within the range from idle run to the area slightly below full thrust without tripping the limiter of the maximum rotor rpm, under normal ambient conditions on the ground and for various settings for the $\Delta T3_f$ parameter

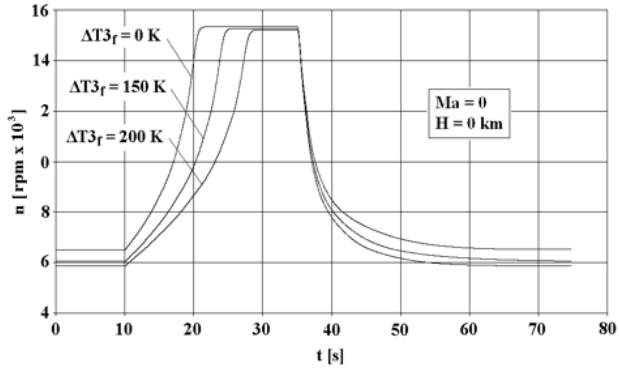

Fig. 10. Timings for the rotor rpm during acceleration and deceleration of the jet engine within the range from idle run to the area slightly below full thrust without tripping the limiter of the maximum rotor rpm, under normal ambient conditions on the ground and for various settings for the $\Delta T3_f$ parameter

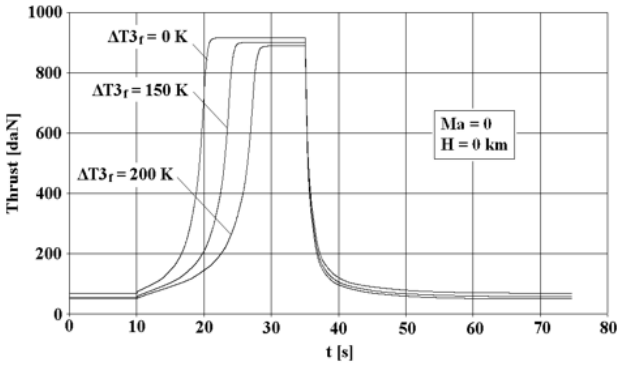

Fig. 11. Timings for the engine thrust during acceleration and deceleration of the jet engine within the range from idle run to the area slightly below full thrust without tripping the limiter of the maximum rotor rpm, under normal ambient conditions on the ground and for various settings for the $\Delta T3_f$ parameter

The foregoing results indicate the need to thoroughly examine impact of the $\Delta T3_f$ parameter onto static characteristic curves of the engine.

4.2. Selected static characteristics

As mentioned before, static characteristic curves for the engine model were determined with use of the own-developed method, called by scanning of the state space. Among other applications the method was also used to find out static characteristic curves of the K-15 engine. The key advantage of the method is the possibility to obtain great many points with measurement results for steady states, where the scanning time is much shorter than it takes place when the conventional method is applied. However, the method has also a drawback, since it can be applied for determination of static characteristic curves merely for single-rotor engines with small volume of the jet nozzle duct, i.e. for such engines where dynamic behaviour thereof can be described by means of the 1st order non-linear differential equation.

The typical property of all other static characteristic curves that are shown in Fig. 12 to Fig. 14 is the fact they substantially differ from each other for various values of the $\Delta T3_f$ parameter.

It is worth paying attention that static characteristic curves plotted for the engine for the flight at the altitude of H = 6 km feature elevated rotor rpm within the range of idle run, which can be seen from comparison between Fig. 12 and Fig. 13. It is the distinctive property of all avionic turbojet engines and it was correctly reproduced in the simulation model for the SO-3 engine applied to these studies.

5. CONCLUSIONS

The investigations enabled to find out substantial impact of temperature field non-homogeneity onto deterioration of both dynamic and static properties of the SO-3 engine. The non-homogeneity leads to a lag of the acceleration time (see Fig. 9 to Fig. 11), which is the crucial parameter for suitability of the engine for use. Also other performance parameters of the engine in its steady state, such as specific fuel consumption per thrust unit and total fuel consumption in time, are considerably higher. It is the phenomenon that can be spotted both for operation of the engine on the ground (Ma = 0, H = 0) and at flight (Ma = 0.4, H = 6 km).

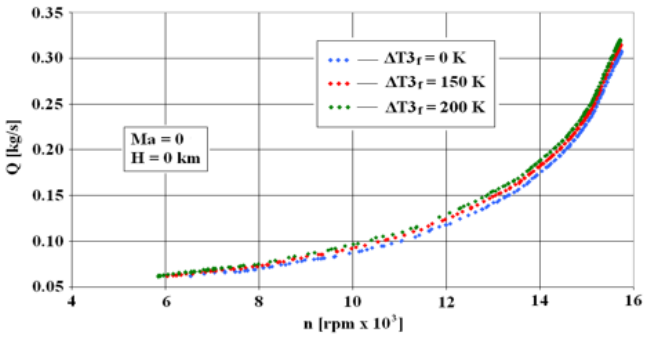

Fig. 12. Static characteristic curves plotted for the jet engine in the coordinate system $Q = f(n)$ for various fixed values of the $\Delta T3_f$ under normal ambient conditions on the ground

Results from investigations on a real object confirm the impact of the temperature field non-homogeneity within the working agent at the turbine intake onto entire duration of the engine acceleration process underground conditions. The impact of the mentioned temperature field onto specific and total fuel consumption in steady

states, although revealed by experiments carried out within the scope of these studies, is still awaiting its experimental confirmation.

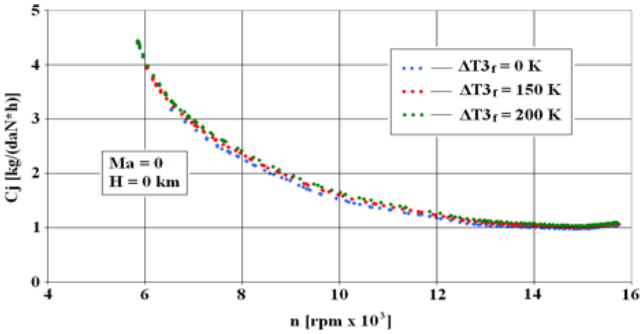

Fig. 13. Static characteristic curves plotted for the jet engine in the coordinate system $C_j = f(Q)$ for various fixed values of the $\Delta T3_f$ under normal ambient conditions on the ground

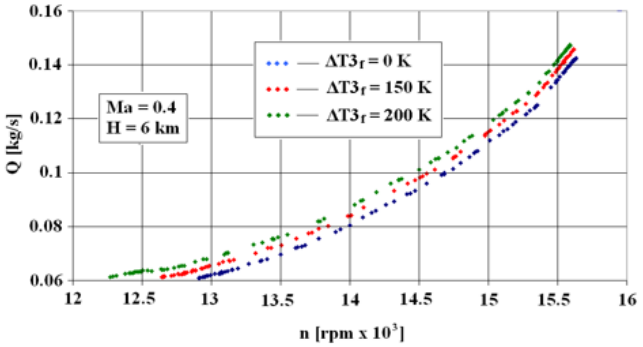

Fig. 14. Static characteristic curves plotted for the jet engine in the coordinate system $Q = f(n)$ for various fixed values of the $\Delta T3_f$ for the flight at the speed of Ma = 0.4 at the altitude of H = 6 km under normal ambient conditions

The phenomena described in the Introduction are visible when the conventional parameter that stands for non-homogeneity of the temperature field distribution is large enough, e.g. $\Delta T3_f$ > 100K. Thus, one can expect that for a real engine it will be possible to apply the method disclosed in this paper to define requirements to the permissible maximum of dispersion for the temperature of the working agent.

REFERENCES

1. **Błachnio J., Dięgielewski W., Kułaszka A., Zasada D.** (2014), Operation-attributable factors and how they affect condition of heat-resistant coatings of gas-turbine blades, *Studies and Proceedings of the Polish Association of Knowledge Management*, No. 68, 17-31.
2. **Błachnio J., Pawlak W.** (2011), Damageability of gas turbine blades - evaluation of exhaust gas temperature in front of the turbine using a non-linear observer, Advances in Gas Turbine Technology, *In Tech*, 435-464.
3. **Bogdan M., Błachnio, J**. (2010), A non-destructive method to assess condition of gas turbine blades, based on the analysis of blade-surface image, *Russian Journal of Nondestructive Testing*, Vol. 46, No. 11, 860-866.
4. **Driankov D., Hellendoorn H., Reinfrank M.** (1966), *Introduction to fuzzy-logic control*, WNT, Warsaw.
5. **Dzida M.** (2000), *Identification of reasons for non-stationary and non-homogenous behaviour of gas temperatures and pressures downstream the combustion chamber of gas turbines*, Publishing House of the University of Technology in Gdańsk.
6. **Marsh S.** (2013), Preventig fretting fatigue in blade dovetail roots by modifying geometry of contact surfaces, *Power Transmission Engineering*, 28, 45-49.
7. **Pawlak W., Wiklik K., Morawski J. M.** (1966), *Synthesis and investigation of control systems for turbojet engines with use of computer simulation methods*, Scientific Library of ITWL, Warsaw.
8. **Pawlak W. I.** (2000), Influence of an inequality of gas thermal field at the engine turbine inlet on the speed of transient processes – the result of experiments with simulation model, *Journal of KONES Internal Combustion Engines*, Vol. 7, No. 1-2, 37-42.
9. **Pawlak W. I .** (2010), *Turbojet engine – instruments for simulation, control and monitoring*, Scientific Library of the Institute of Aviation, Warsaw.
10. **Pawlak W. I., Balicki W.** (2003), Influence of an inequality of gas thermal field at the engine turbine inlet on the speed of transient processes – the result of experiments with real engine, *Journal of KONES*, Vol. 10, No. 3-4, 25-28.
11. **Pismenny J., Levy Y.** (2002), Local Temperature Regulator In Gas Turbine Engines, *International Journal of Turbo& Jet – Engines*, Vol. 10, No. 1-2, 79-92.
12. **Spychała J., Pawlak W., Kułaszka A., Błachnio J.** (2013), Assessment of technical condition demonstrated by gas turbine blades by processing of images for their surfaces, *Journal of KONBIN*, 1 (21), 41-50.
13. **Stewart I.** (2001), *Does God play dice. The new mathematics of chaos*, PWN Scientific Publications, Warsaw.
14. **Swadźba L., Maciejny A., Formanek B., Mendala B.** (2008), Characterization of microstructure and properties of TBC systems with gradient of chemical composition and porosity, *Archives of Metallurgy and Materials*, 53, 945-954.
15. **Wróbel Z., Koprowski R.** (2004), *Practice in image processing within the MATLAB software*, EXIT Academic Publishing House, Warsaw.
16. **Żółtowski B., Cempel C.** (2004), *Machinery fault diagnosis engineering*, Polish Society of Engineering Diagnosis, Warsaw.

DOI 10.2478/ama-2014-0039

PID CONTROLLERS DESIGN APPLIED TO POSITIONING OF BALL ON THE STEWART PLATFORM

Andrzej KOSZEWNIK*, Kamil TROC*, Maciej SŁOWIK*

*Faculty of Mechanical Engineering, Bialystok University of Technology, ul. Wiejska 45C, 15-351 Białystok, Poland

a.koszewnik@pb.edu.pl, kamiltroc@o2.pl, m.slowik@pb.edu.pl

Abstract: The paper presents the design and practical implementation of PID controllers for a Stewart platform. The platform uses a resistance touch panel as a sensor and servo motors as actuators. The complete control system stabilizing the ball on the platform is realized with the Arduino microcontroller and the Matlab/Simulink software. Two processes required to acquire measurement signals from the touch panel in two perpendicular directions $\boldsymbol{X}$ and $\boldsymbol{Y}$, are discussed. The first process includes the calibration of the touch panel, and the second process - the filtering of measurement signals with the low pass Butterworth filter. The obtained signals are used to design the algorithm of the ball stabilization by decoupling the global system into two local subsystems. The algorithm is implemented in a soft real time system. The parameters of both PID controllers (PID$\boldsymbol{x}$ and PID$\boldsymbol{y}$) are tuned by the trial-error method and implemented in the microcontroller. Finally, the complete control system is tested at the laboratory stand.

Key words: PID Controller, Low Pass Butterworth Filter, Stewart-Gough Platform, Arduino Microcontroller, USB Port, Touch Panel Sensor

1. INTRODUCTION

Parallel link manipulators known as the "Stewart-Gough" platforms (see Fig.1) were investigated thoroughly in the last years. Since their potential advantages as: high rigidity, high accuracy, and high load-carrying capacity they seem to be better in comparison to the conventional serial link manipulators. That is why many researches often choose such structures as control plants. The first parallel mechanism was introduced by Gough and Whitehall in 1956 year (Gough and Whitehall, 2012) as a tyre-testing machine. Next, the design of the platform was improved by Stewart in 1965. Then, the modernized structure was used as an aircraft or vehicle simulation device. Parallel manipulators were used also as platforms for communication satellite dishes and telescopes positioning.

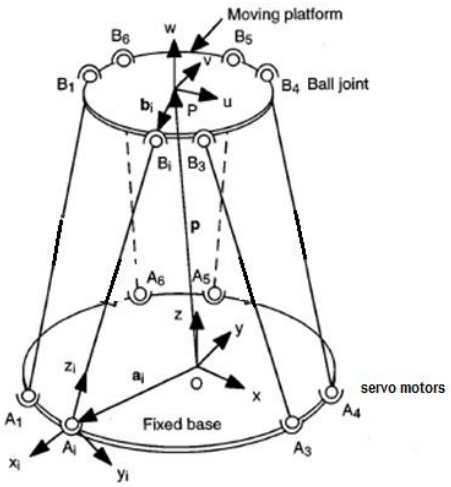

Fig. 1. Electrically actuated Stewart-Gough platform

The most popular type of actuators used in parallel link manipulators are pneumatic or hydraulic actuators. Both types of actuators have many advantages and their application in the system depends on the payload to weight ratio and on the dimensions of the system. Since pneumatic devices are less sensitive to temperature changes and contamination, a lot of researchers have tried controlling air cylinders using various methods.

One of the most popular control methods is the PID technique. Wang and Van Varseveld and Bone (Wang et al., 1999; Varseveld and Bone, 1997) used PID controllers with nonlinear compensation for servo-pneumatic actuators to control the position of the Stewart platform. Weng and Xu (2013) also used the PID controller with the LQG filter to control the position and to damp the vibration of the platform. Other researchers used non-traditional control methods. Urenizezius et al. applied the LQR technique. Paul et al implemented the sliding mode control (Urniezius and Geguzis, 2014; Paul et al., 1994; Shunmugham and Hayakawa, 1997). Wang et al. (2009) used the optimal control method based on the generalized natural frequencies of the system to stabilize the platform.

The Stewart platform discussed in the current article is a small size structure (the dimension of the fixed platform is 30 cm, and of the moving platform – 11 cm) with the low payload to weight ratio. The control system for a ball on the platform is realized by six electrical servo motors, the resistance touch panel and the PID controller. The choice of the PID control algorithm has been dictated mainly by practice problems of controlling the platform rather than by theoretical considerations of designing the control law. Other control methods would be difficult to implement because the mathematical model of the platform does not exist yet. Moreover, the PID control technique is a first control law investigated at this laboratory stand and it is realized together with a student. The design and experimental verification of other control methods will be the subject of future investigations.

The paper presents consecutive steps of the design process and practical implementation of the chosen control algorithm for the platform and the Butterworth filters for the measurement signals.

2. THE STEWART PLATFORM AS A PLANT OF THE CONTROL SYSTEM

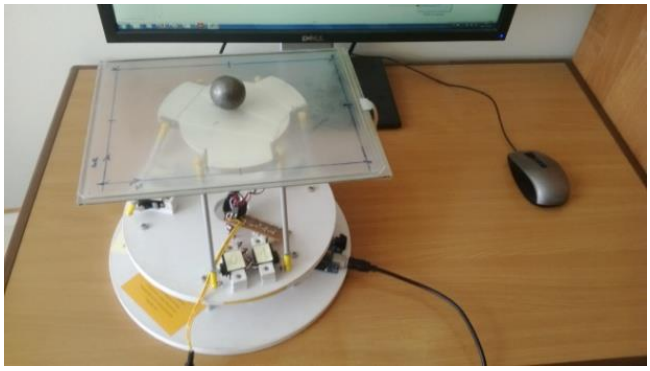

Fig. 2. The laboratory stand with the touch panel and the microcontroller

The 6-DOF Stewart platform shown in Fig. 2 consists of: a base frame, a moving platform, six legs, and components of the control system. As actuators the NewPower XL-9HM servomotors have been chosen and located on the frame base. As a sensor the RES121-4W touchpad has been chosen (http://www.buddyrc.com/new-power-xl-9hm.html). The process of stabilization of the ball on the upper platform is realized by the 8-bit Arduino Mega 2560 microcontroller operating at 16 MHz frequency.

3. THE CONTROL ALGORITHM

The control algorithm of stabilization of the ball on the upper platform is realized by the established communication link between the Arduino microcontroller and the Matlab/Simulink software via the USB port. The standard transmission rate for this port is up to 480Mb/s (115 kb/s in the current case), so this rate is sufficient to control the system in the soft real time system regime (http://stackoverflow.com/questions/17308956/differences-between-hard-real-time-soft-real-time-and-firm-real-time). The diagrams of the control system and algorithm are shown in Figs. 3 and 4.

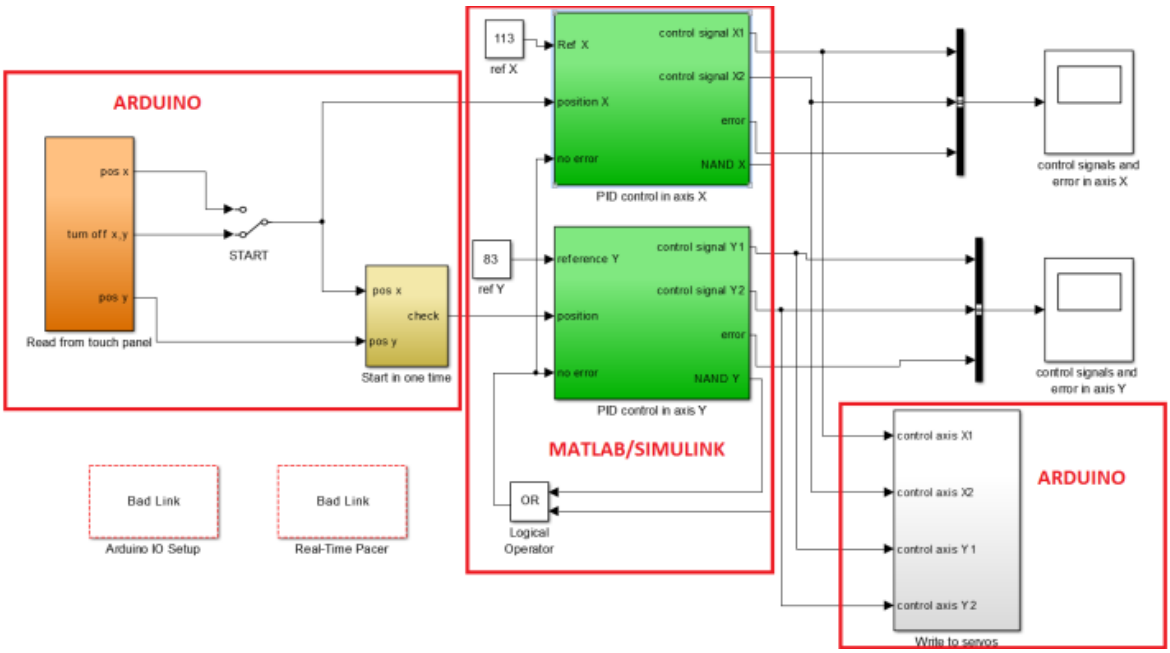

Fig. 3. The control scheme of the ball position

According to Fig. 4, the error signals in two perpendicular directions X and Y are obtained based on two measured signals (posx and posy) and two setpoint values (ref_x and ref_y). Both desired values: $ref_x = 113$ and $ref_y = 3$ correspond to a real middle point of the touch panel in two directions X and Y, respectively. If the ball's position on the platform is greater than 2 mm in each direction then the control signals u_x and y are calculated in Matlab/Simulink and configuration of servo motors is changed (the signals are sent to Arduino). Otherwise the configuration of the servo motors remains the same.

The complete control system is based on the Matlab/Simulink software and the Arduino microcontroller hardware. As a result the block diagram consists four main subsystems are prepared and shown in Fig.4:

- read from touchpanel – the signals from touchpanel is read by Arduino and filtered,
- simultaneous start – synchronous switch on both control feedback loop,
- write to servos – the values control signals from Matlab are recalculated and pass to servos,
- PID control – the control signals u_x and u_y are calculated with using Matlab software.

DOI 10.2478/ama-2014-0039

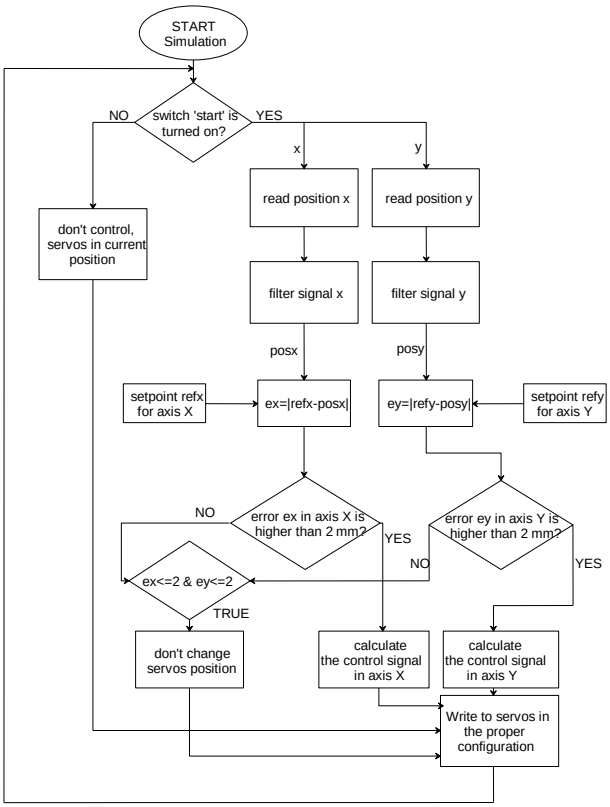

Fig. 4. Scheme algorithm of stabilization the ball on the platform ($ref_x = 113$ mm, $ref_y = 83$ mm)

4. CALIBRATION PROCESS OF THE TOUCH PANEL

The calibration process of the touch panel for different location of the ball on the platform is carried out in the paper. In this order the ball is located into two extreme position and one position into centre point on the sensor versus two perpendicular directions X and Y, respectively. In results values of resistance of electrodes on the touch panel are measured and recorded in Fig. 5 and Fig. 6. Finally, obtained results are collected and transformed into displacement in Tab. 1.

Tab. 1. Results of calibration process of the touch panel

Direction	Resistance Ω	Displacement mm
X	207-875	0-232
Y	219-814	0-166

The comparison of both figures (Fig. 5 and Fig. 6) shown correctly response action of the touch panel in both directions, but obtained values of resistance in Y direction have firmly distribution. Thus, in order to design correctly control law these signals should pass by low pass 2-order Butterworth filter in frequency range up to $\omega_{cutoff} = 35$ rad/s, which transfer function as follows (http://www.ece.uah.edu/corses/ee426/Butterworth.pdf):

$$H(s) = \frac{0.1225}{s^2+0.495s+0.1225} \quad (1)$$

Taking into account Fig. 7 and Fig. 8 we can see that the signals from the touch panel in perpendicular directions are filtered, however application of this filter in the control system cause appear time delay on level 40 ms. In results we obtained possibility of design the control system only in soft real-time regime system.

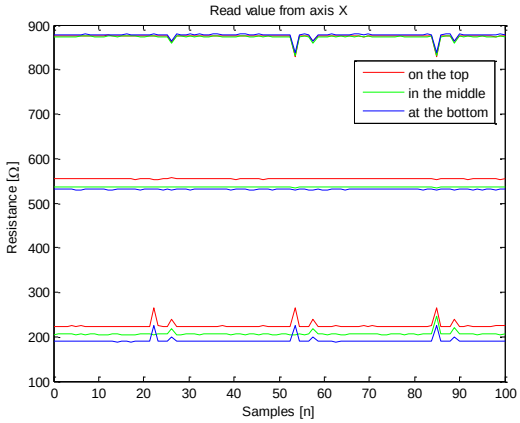

Fig. 5. The calibration of the touch panel in X axis

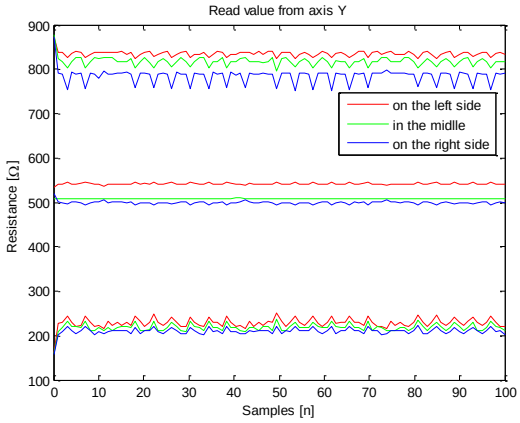

Fig. 6. The calibration of the touch panel in Y axis

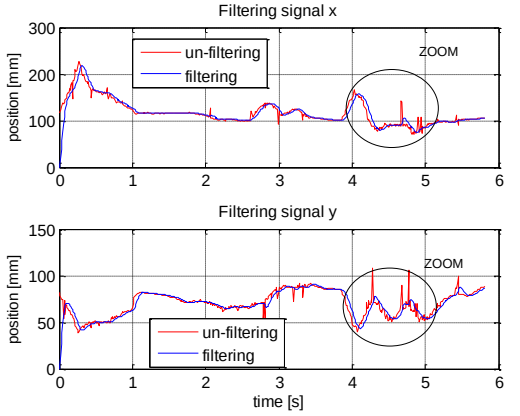

Fig. 7. The comparison of non-filtering and filtering signals

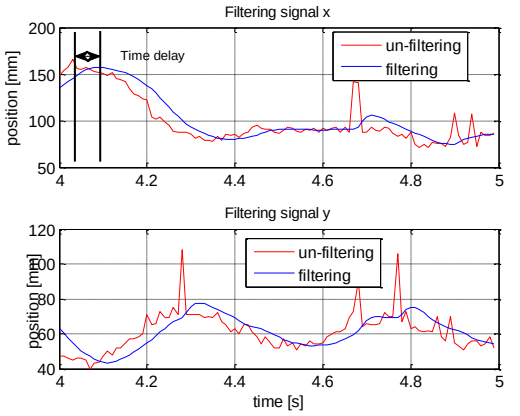

Fig. 8. The comparison of non-filtering and filtering signals in zoom scale

5. CONTROL STRATEGY

The stage of design of stabilization the ball on the platform require to consider location of all six servo motors on the base platform. As first, the opposite site servo motors are coupled versus their location on the fixed base. Next, taking into account one couple of servo motors, the control signals $U+$ and $U-$ are generated by controllers for each of them. The control signals expressed by Eq. 2 consists value of 90 that represents the initial value of the control signal. Based on this assumption the control signals can be written as follows:

$$U1^{+}(t) = 90 + u_{PIDx}(t)$$
$$U1^{-}(t) = 90 - u_{PIDx}(t) \quad (2)$$

where: $u_{PIDx}(t) = k_p e(t) + k_i \int e(t)dt + k_d \frac{de(t)}{dt}$.

Practical realization of control subsystem to stabilize position of the ball in the X axis is shown in Fig. 9. The subsystem according to Fig. 3 consists three inputs: $ref_x = 113$ (desired value), measurement value of position of the ball and signal without error. The last signal is responsible for simultaneously switching the control system between two directions for two cases. Once the ball is in the center point of the touch panel with extreme values less from +/- 2mm, but in the second case button START is switch off. If the ball is in the center point of the touch panel then values of the error signals are checked. If -2< ex <2 for X direction then the output signal from logic gate NANDD_x equal 0 and output value with logic gate OR also is 0 (in case that NANDD_y also equal 0). In results the error signal is 0 and all servo motors have still actual values. In second case the error signal is omitted if mentioned button has been switched off. In such case variable posx equals -20 and in the result one of inputs of multiply block is equal 0. Finally, the control signals $X1$ and $X2$ for X axis are generated by PIDx. Obtained signals in range of 30-150 corresponds to minimal and maximal pitch angle of rudder bar of the servo motors.

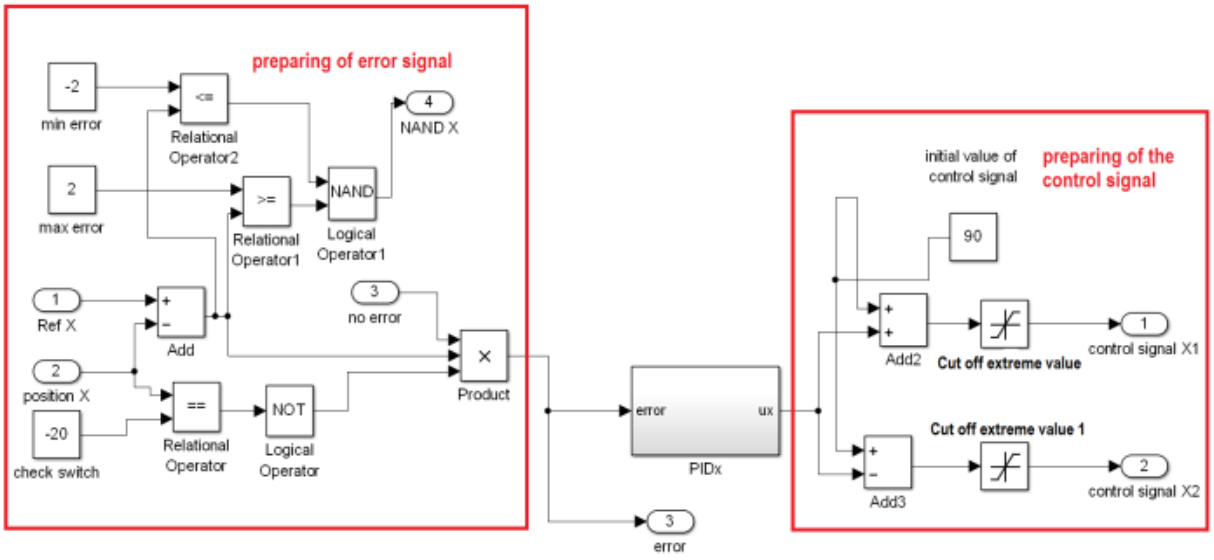

Fig. 9. The control scheme of the control of ball position's in *X* direction

The parameters of PID controllers are chosen directly on the lab stand in few stages. In first order the system is prepared to tests by setting up the rudder bar of actuators in parallel orientation versus the fixed base of the platform. In result the initial condition of the control system and initial value of control signals are set up to 0 and 90, respectively. In the next step the ball is located in position (-55; -30) from middle position of the touch panel. After that the parameters of the both controllers PIDx and PIDy are tuned by the trial error method. As a result the transfer function of these controllers are expressed as follows:

$$PID_X(s) = \frac{0.1s^2+0.35s+0.25}{s} \quad (3)$$

$$PID_Y(s) = \frac{0.12s^2+0.45s+0.25}{s} \quad (4)$$

Next, obtained signals from controllers are passed to microcontroller Arduino. The results of carried out investigations – the signals from both control subsystem PIDx and PIDy (error signal and control signal) were recorded and are shown in Fig. 10 and Fig. 11, respectively.

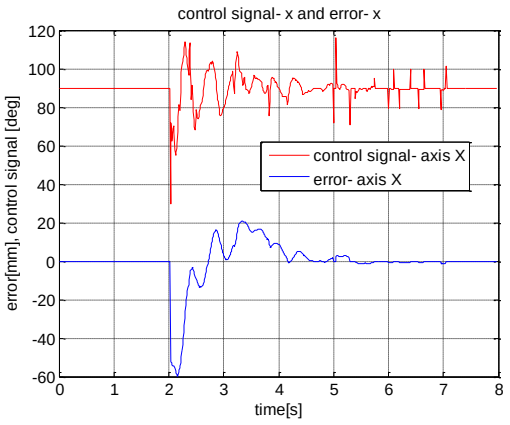

Fig. 10. The control signal and error signal derived by the PIDx controller

We can see, that the position of the ball is constant in desired point of the platform up to 2 second. After that, the both control loops are switched on as a result of change of the ball location greater than 2 mm in two directions. One more time stabilization of the ball of the platform is achieved after 3 or 5 seconds.

DOI 10.2478/ama-2014-0039

The difference between both transient periods of stabilization of the ball occurs because the controller PIDy generates peaks of high values after 4 seconds in the control signal. Finally, obtained results are satisfying in point of view of control system such structure and further investigations allow us to compare PID controller with other types of control methods.

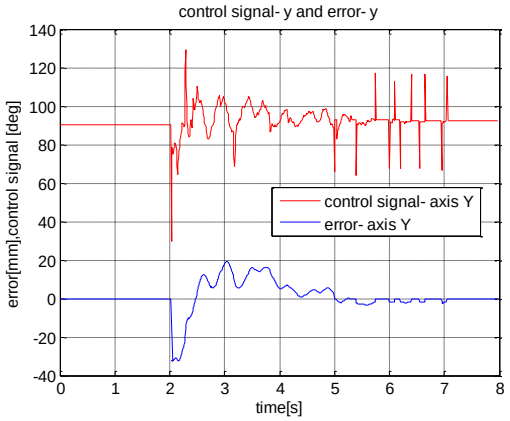

Fig. 11. The control signal and error signal derived by the PIDy controller

6. CONCLUSIONS

The research work aimed stabilization of the ball on the Stewart platform with using Arduino microcontroller and Matlab/Simulink software. The process of designation of the parameters of the PID controllers is carried out in many stages. In the first step we successfully shown two process of preparing of the measurment signals: calibration of the touch sensor and filtering signals with using low pass Butterworth filter. Next, the parameters of both PID controllers (PIDx and PIDy) are determined directly on the laboratory stand. Moreover, we passed these parameters of the controllers to microcontroler Arduino and we tested the whole control system in regime of soft-real time system.

REFERENCES

1. **Gough V. E., Whitehall S. G.** (2012), Universal tyre test machine, *Proceedings of the 9th International Technical Congress F.I.S.I.T.A*, 117–137,1962.
2. **Paul A. K., Mishra J. K., Radke M. G.** (1994, Reduced order sliding mode control for pneumatic actuator, *IEEE Transactions on Control Systems Technology*, Vol. 2, No. 3, 271–276.
3. **Shunmugham P., Hayakawa Y.** (1997), Practical design of adaptive model-based sliding mode control of pneumatic actuators, *Proceedings of Advanced Intelligent Mechatronics*, IEEE, Tokyo, Japan, 140.
4. **Urniezius R., Geguzis E.** (2014), Hybrid Fuzzy Logic and Adpative LQR Controller for Swing-up, Positioting and Stabilization of Inverted Pendulum*, Elektronika ir Elektrotechnika*, Vol.20, No.3, 11-15.
5. **Varseveld R. B. V., Bone G. M.** (1997), Accurate position control of a pneumatic actuator using on/off solenoid valves, *IEEE/ASME Transactions on Mechatronics*, Vol. 2, No. 3, 195–204.
6. **Wang J., Pu J., Moore P.** (1999)**,** A practical control strategyfor servo-pneumatic actuator systems, *Control Engineering Practice*, Vol. 7, No. 12, 1483–1488.
7. **Wang W., Yang H., Zou J., Ruan X., Fu X.** (2009) Optimal design of Stewart platforms based on expanding the control bandwidth while considering the hydraulic system design, *Journal of Zhejiang University*, Vol.10(1), 22-30.
8. **Weng Ch., Xu Z.** (2013), Track-position and vibration control simulation for strut of the Stewart platform, *Applied Physics and Engineering*, Vol.14(4), 281-291.
9. http://stackoverflow.com/questions/17308956/differences-between-hard-real-time-soft-real-time-and-firm-real-time (10.09.2014)
10. http://www.buddyrc.com/new-power-xl-9hm.html (12.03.2014)
11. http://www.ece.uah.edu/corses/ee426/Butterworth.pdf (30.09.2014)

This work is co-financed from Dean's Project W/WM/19/2013 and Statutory Work of Department of Automatic Control and Robotics S/WM/1/2012

CROSS-CORRELATION-BASED METHOD VS. CLASSICAL FFT FOR SPECTRAL ANALYSIS OF IMPULSE RESPONSE

Adam KOTOWSKI*

*Faculty of Mechanical Engineering, Department of Automatic Control and Robotics, Bialystok University of Technology, ul. Wiejska 45C, 15-351 Bialystok, Poland

a.kotowski@pb.edu.pl

Abstract: The paper presents comparison of results of impulse response spectral analysis that has been obtained using a method based on cross-correlation with results obtained using classical FFT. The presented non-Fourier method is achieved by correlating the analyzed signal and reference single-harmonic signals and using Hilbert transform to obtain an envelope of cross-correlation. The envelope of cross-correlation makes it possible to calculate appropriate indicator and make its plot in frequency domain as a spectrum. The spectrum obtained this way has its advantage over the FFT that the spectral resolution does not depend on duration of signal. At the same time, the spectral resolution can be much greater than spectral resolution resultant from FFT. Obtained results show that presented non-Fourier method gives frequency readout more accurate in comparison to FFT when the impulse response is a short-time signal e.g. few dozen of miliseconds lasting.

Key words: Spectral Analysis, FFT, Cross-Correlation, Hilbert transform, Envelope, Spectral Resolution

1. INTRODUCTION

Impulse response as a result of impact testing has been used in wide area of engineering owing to its convenience and simplicity on experimentation (Ahn et al., 2005). It is well known that using fast Fourier transform (FFT) for spectrum analysis will give an immediate frequency profile of recorded signals. When analyzing signals using FFT, frequency resolution is fixed as an inverse of the duration of the analyzed signal (Bendat and Piersol, 1980; Gasior, 2004) and, as a result, it fails to meet the requirements of measurement. One of the ways to increase frequency resolution and improve frequency reading is interpolation. It improves the resolution by a few orders, depending on the interpolation method (Gasior, 2006; Gasior, 2010). In order to avoid limitation in frequency resolution using FFT, it has been investigated the problem of frequency resolution and showed that it was possible to obtain frequency resolution of one-tenth of the spacing between the frequency points produced by the Fourier transform (Cawley and Adams, 1979). For increasing spectral frequency resolution and improving frequency estimation, the zero-padding technique also is widely used (Quinn, 2009; Dunne, 2002). In general, the interpolation algorithms can be a computing-cost-effective replacement of the zero-padding technique in applications (Gasior, 2006).

There are a great number of engineering applications of correlation function (Bendat and Piersol, 1980). Looking for its new applications, the cross-correlation function has been utilized to correlate real-measured signal and a single-harmonic signal generated by software (Kotowski, 2010). Also, the Hilbert transform was used to obtain the envelope of the cross-correlation function (Thrane, 1984; Thrane et al., 1999).

This paper describes a method of reading a particular frequency of the harmonic developed on the basis of the cross-correlation function and its envelope. The main advantage of this method over the FFT is its ability to obtain different frequency resolution from that obtained by using FFT, often required as increased resolution, e.g. ten times increased.

2. METHODOLOGY

The cross-correlation function $R_{xy}(\tau)$ between two processes, $x(t)$ and $y(t)$, is calculating by the expression (Bendat and Piersol, 1980):

$$R_{xy}(\tau) = \lim_{T\to\infty} \frac{1}{T} \int_0^T x(t)y(t+\tau)\,dt \tag{1}$$

where: T – signal record length, τ – argument of cross-correlation function (time delay).

The Hilbert Transform (HT) enables calculation of the envelope $A(t)$ of a real-valued function $x(t)$ as follows (Thrane et al., 1999; Feldman, 2011):

$$A(t) = \sqrt{x^2(t) + \tilde{x}^2(t)} \tag{2}$$

where $\tilde{x}(t)$ is HT of a real-valued function $x(t)$. Then, an envelope of the cross-correlation function Renv is as follows:

$$R_{env}(\tau) = \sqrt{{R_{xy}}^2(\tau) + {\tilde{R}_{xy}}^2(\tau)} \tag{3}$$

where: $\tilde{R}_{xy}$ is HT of the cross-correlation R_{xy}. The envelope of the cross-correlation of two harmonic processes with one of them being damped, decays exponentially. In addition, the equality of the frequencies of the harmonics creates the highest position of the envelope plot in comparison to the non-equality of the frequencies (Kotowski, 2014). Apart from analyzed signal $y(t)$, the method used in the paper requires a series of harmonic signals gi(t) generated as follows:

$$g_i = \sin(2\pi \cdot w \cdot i \cdot t) \tag{4}$$

where: i – an integer value (index), w – frequency resolution.

After correlating the input and the generated signals, the plot position of the envelope of the cross-correlation indicates an identification of the harmonic detected. This phenomenon is easy to observe and the determination of common frequency is simple. As a result, the envelope plot can be effectively used to identify the harmonics incorporated in recorded signals with no need for the Fourier transform. The frequency value of the harmonic in the input signal $y(t)$ can be determined using the envelope plot. Studying the envelopes, we obtain both w and i values of signal $g_i(t)$ used for calculations. Thus, formula $(w \cdot i)$ indicates the frequency of the identified harmonic. Apart from cross-correlation envelope plots, indicator S_e is used to express envelope position numerically as follows:

$$S_e(n) = \Delta t \sum_{n=1}^{N} R_{env}(n) \tag{5}$$

where R_{env} is the cross-correlation envelope, Δt is the sampling period and N stands for the number of samples. As a result, it is possible to prepare the S_e plot, as a result of spectral analysis, for a frequency span in which the impulse response has been recorded. The frequency resolution of S_e plot is strictly connected to w value.

3. DATA FOR ANALYSIS

To illustrate the comparison between cross-correlation-based method and FFT for spectral analysis of impulse response, a numerical example of a four-degree-of-freedom system impulse response is considered.

The unit impulse response function of a multi-degree-of-freedom system can be expressed as (Ahn et al., 2005):

$$h(t) = \sum_{r=1}^{n} A_r \exp(-\sigma_r t)\sin(\omega_{dr} t) \tag{6}$$

where: A_r – the rth modal constant, σ_r – the rth modal damping, ω_{dr} the rth damped angular frequency of the system. Thus, four-degree-of-freedom system impulse response can be expressed as:

$$\begin{aligned} h(t) = {} & A_1 \exp(-\sigma_1 t)\sin(2\pi f_1 t) \\ & + A_2 \exp(-\sigma_2 t)\sin(2\pi f_2 t) \\ & + \ldots + A_3 \exp(-\sigma_3 t)\sin(2\pi f_3 t) \\ & + A_4 \exp(-\sigma_4 t)\sin(2\pi f_4 t) \end{aligned} \tag{7}$$

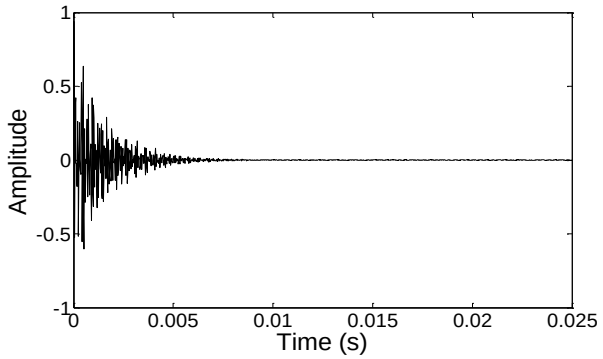

Fig. 1. Impulse response for analysis

For obtaining time history of four-degree-of-freedom system impulse response, values of parameters of Eq. (7) have been assumed. They are: $A_1 = 0.13$, $A_2 = 0.40$, $A_3 = 0.23$, $A_4 = 0.30$, $\sigma_1 = 560$, $\sigma_2 = 610$, $\sigma_3 = 640$, $\sigma_4 = 600$, $f_1 = 3196.4$ Hz, $f_2 = 11027.3$ Hz, $f_3 = 13244.5$ Hz, $f_4 = 15168.7$ Hz. The considered impulse response have been calculated by sampling frequency equal to 48000 Hz and sampling time T equal to 0.025 s. The impulse response under consideration is shown in Fig.1. In fact, the impulse response goes to zero after the time of 0.010 s. These two periods of time history are to be considered in the next Section.

4. RESULTS

In this section, it is presented results of impulse response spectral analysis by using cross-correlation-based (CCB) method and FFT. These kinds of analysis are compared on the basis of values of frequencies readout for four spectra peaks.

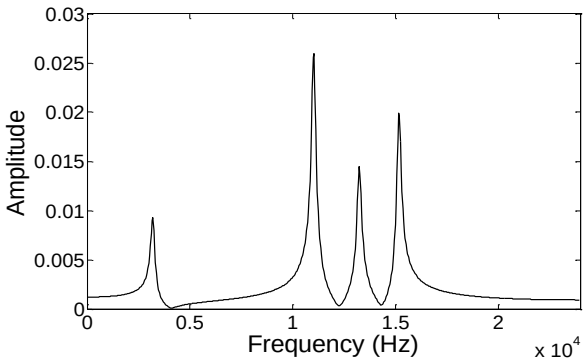

Fig. 2. Impulse response spectrum obtained using FFT for $T = 0.025$s

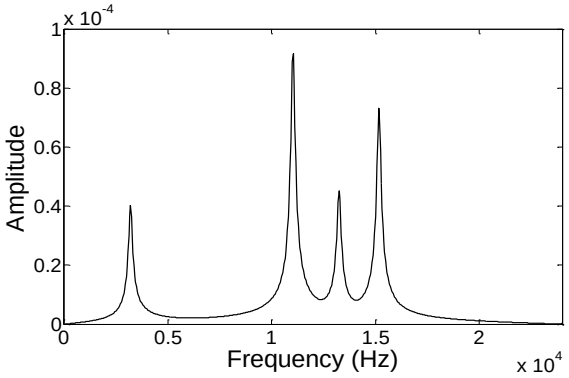

Fig. 3. S_e indicator plot for $T = 0.025$s and $\Delta f = 40$Hz

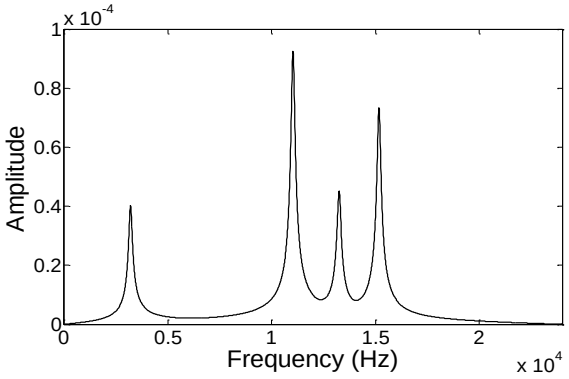

Fig. 4. S_e indicator plot for $T = 0.025$s and $\Delta f = 10$Hz

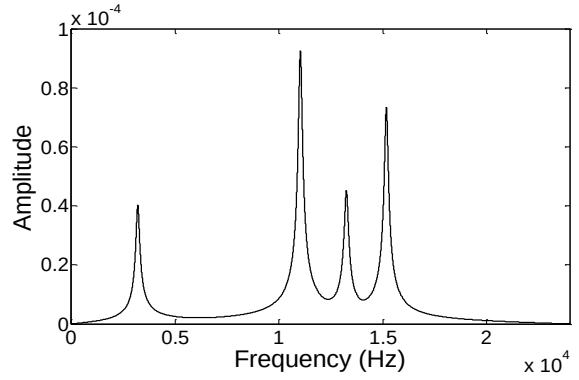

Fig. 5. S_e indicator plot for $T = 0.025\text{s}$ and $\Delta f = 1\text{Hz}$

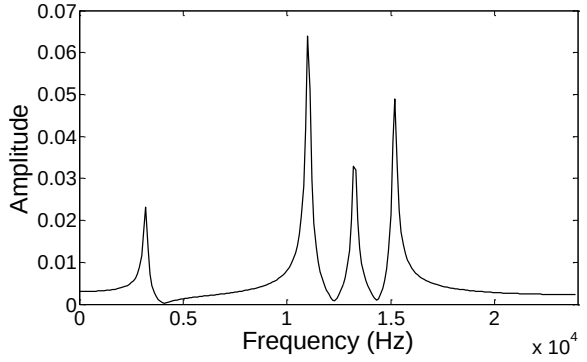

Fig. 6. Impulse response spectrum obtained using FFT for $T = 0.010\text{s}$

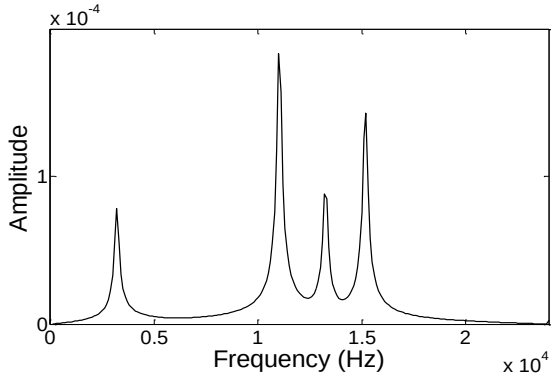

Fig. 7. S_e indicator plot for $T = 0.010\text{s}$ and $\Delta f = 100\text{Hz}$

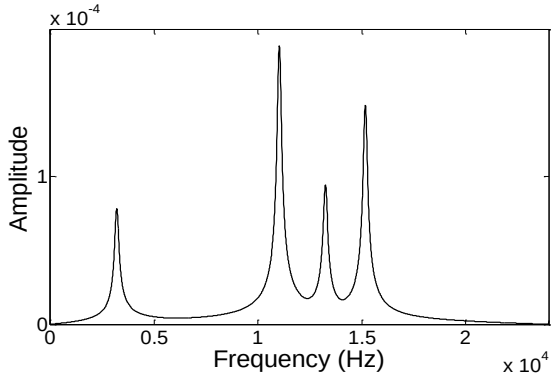

Fig. 8. S_e indicator plot for $T = 0.010\text{s}$ and $\Delta f = 10\text{Hz}$

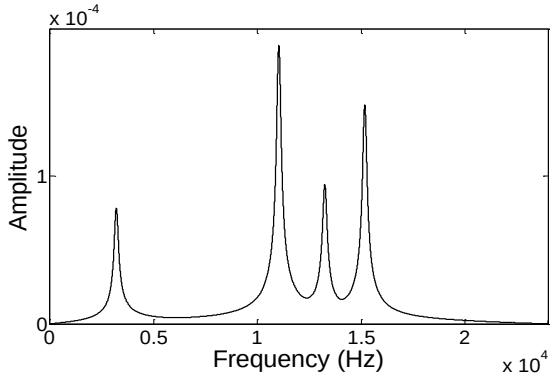

Fig. 9. S_e indicator plot for $T = 0.010\text{s}$ and $\Delta f = 1\text{Hz}$

The spectral analysis using FFT has resulted frequencies readout by frequency resolution Δf as a result of the sampling time of impulse response T. It has been 40Hz and 100Hz for 0.025 second and 0.010 second, respectively. The spectral analysis using CCB method has resulted frequencies readout by different frequency resolution independent of the sampling time of impulse response.

The spectra obtained using FFT and the Se indicator (Eq.5) for $T = 0.025$ second and $T = 0.010$ second are shown in Figs. 2-5 and Figs. 6-9, respectively.

The values of frequencies read from plots for both methods are shown in Tabs. 1 and 2 for sampling tine equal to 0.025s and 0.010s, respectively. There are four frequency values for succeeding four plot peaks. The one of CCB method frequency resolution has been fixed the same as for FFT (40Hz, 100Hz). For further research of CCB method, resolution of 10Hz and 1Hz has also been considered for that method.

Tab. 1. Results for sampling time $T = 0.025\text{s}$

Theoretical frequency (Hz)	FFT Δf=40Hz	CCB method Δf=40Hz	CCB method Δf=10Hz	CCB method Δf=1Hz
3196.4	3200	3200	3200	3198
11027.3	11040	11040	11030	11028
13244.5	13240	13240	13240	13244
15168.7	15160	15160	15170	15169

Tab. 2. Results for sampling time $T = 0.010\text{s}$

Theoretical frequency (Hz)	FFT Δf=100Hz	CCB method Δf=100Hz	CCB method Δf=10Hz	CCB method Δf=1Hz
3196.4	3200	3200	3200	3199
11027.3	11000	11000	11030	11028
13244.5	13200	13200	13240	13244
15168.7	15200	15200	15170	15169

The main difference between methods is connected with the errors between determined frequencies and theoretical frequencies. The CCB method allows to obtain higher frequency resolution than classical FFT. It resulted less errors between determined frequencies and theoretical frequencies. Hence, frequency determination has been improved in comparison to classical FFT. Tabs. 1 and 2 also show that results obtained by CCB method do not depend on sampling time, they are the same or difference seems very

negligible. For the frequency resolution of 1Hz, the CCB method resulted the lowest error for both signal lengths. In this case, absolute errors between theoretical frequency and measured frequency reached $2.6(1.6)\text{Hz}$, 0.7Hz, 0.5Hz and 0.3Hz. Using FFT, this errors reached varies from 3.6 to 44.5 Hz. Figs. 10 and 11 show relation in frequency determination errors for two lengths of analyzed impulse response, 0.025s and 0.010s, respectively.

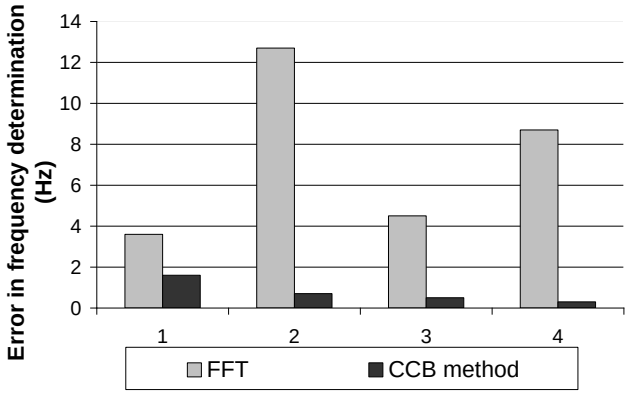

Fig. 10. Relation in frequency determination errors for FFT and CCB method for sampling time $T = 0.025s$

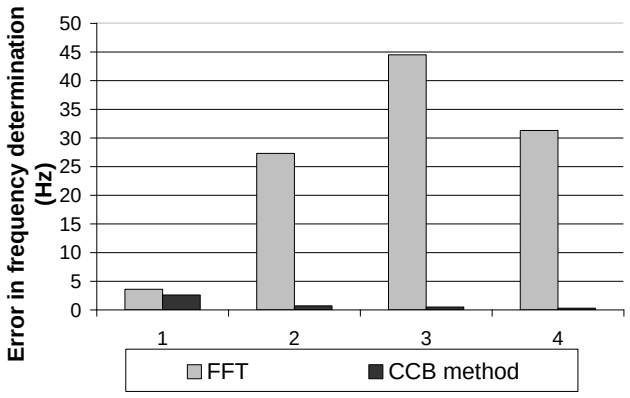

Fig. 11. Relation in frequency determination errors for FFT and CCB method for sampling time $T = 0.010s$

Except peak near theoretical frequency of 3196.4Hz, the frequency errors using CCB method $(0.3 \div 0.7\text{Hz})$ are several dozen times lower than frequencies errors using FFT $(4.5 \div 44.5\text{Hz})$.

5. CONCLUSIONS

The paper presents comparison of results of frequency reading based on impulse response spectral analysis that has been obtained using cross-correlation-based method with results obtained using classical FFT. The presented non-Fourier method is achieved by correlating the analyzed signal and reference single-harmonic signals and using Hilbert transform to obtain an envelope of cross-correlation. The spectral analysis obtained using proposed method has its advantage over the FFT that the spectral resolution does not depend on signal length and it gives a possibility to obtain a controllable spectral resolution. Moreover, the spectral resolution can be much greater than spectral resolution resultant from FFT. By extension, frequency readings are more accurate by doing proposed frequency resolution improvement. Thus, cross-correlation-based method can be an additional method for improving the accuracy of natural frequencies measurement using impulse tests.

REFERENCES

1. **Ahn S. J., Jeong W. B., Yoo W. S.** (2005), Improvement of impulse response spectrum and its application, *Journal of Sound and Vibration*, 288, 1223–1239.
2. **Bendat J. S., Piersol A. G.** (1980), *Engineering applications of correlation and spectral analysis*, Wiley-Interscience, New York.
3. **Cawley P., Adams R. D.** (1979), Improved frequency resolution from transient tests with short record lengths, *Journal of Sound and Vibration*, Vol. 64, 123-132.
4. **Dunne J. F.** (2002), A fast time-domain integration method for computing non-stationary response histories of linear oscillators with discrete-time random forcing, *Journal of Sound and Vibration*, Vol. 254, 635-676.
5. **Feldman M.** (2011), Hilbert transform in vibration analysis, *Mechanical Systems and Signal Processing*, 25, 735-802.
6. **Gasior M.** (2006), *Improving frequency resolution of discrete spectra*, Ph.D. thesis, AGH University of Science and Technology, Krakow, Poland.
7. **Gasior M.** (2010), *Improving frequency resolution of discrete spectra - Algorithms of three-node interpolation*, ISBN 978-3-8383-5943-4, LAP LAMBERT Academic Publishing.
8. **Gasior M., Gonzalez J. L.** (2004), *Improving FFT frequency measurement resolution by parabolic and gaussian interpolation*, AB-Note-2004-021 BDI, CERN, Geneva, Switzerland.
9. **Kotowski A.** (2010), Reading the frequency of harmonics by cross-correlation function and its envelope, *Proc. 6th Int. Conf. Mechatronic Systems and Materials*, 108-109.
10. **Kotowski A.** (2014), A new method for spectral analysis of non-stationary signals from impact tests, *Journal of Vibroengineering*, 16, 2171-2177.
11. **Quinn B. G.** (2009), Recent advances in rapid frequency estimation, *Digital Signal Processing*, 19, 942-948.
12. **Thrane N.** (1984), *The Hilbert Transform*, *Technical Review*, No. 3, Brüel&Kjær, BV 0015.
13. **Thrane N., Wismer J., Konstantin-Hansen H., Gade S.** (1999), *Practical use of the "Hilbert transform"*, Application Note, Brüel&Kjær, BO 0437.

This work was supported by Bialystok University of Technology under work No. S/WM/1/2012.